國立交通大學

機械工程學系

碩士論文

石墨及 PDMS 呼吸式質子交換膜燃料電池之水管理與熱分佈分析

Water Management and Thermal Distribution Analyses of Graphite and PDMS Air-breathing PEMFC

研 究 生：鍾云婷

指導教授：陳俊勳　教授

中華民國一〇〇年六月

石墨及 PDMS 呼吸式質子交換膜燃料電池之水管理與熱分佈分析

Water Management and Thermal Distribution Analyses of Graphite and PDMS Air-breathing PEMFC

研究生：鍾云婷　　Student：Yun-Ting Chung

指導教授：陳俊勳　　Advisor：Chiun-Hsun Chen

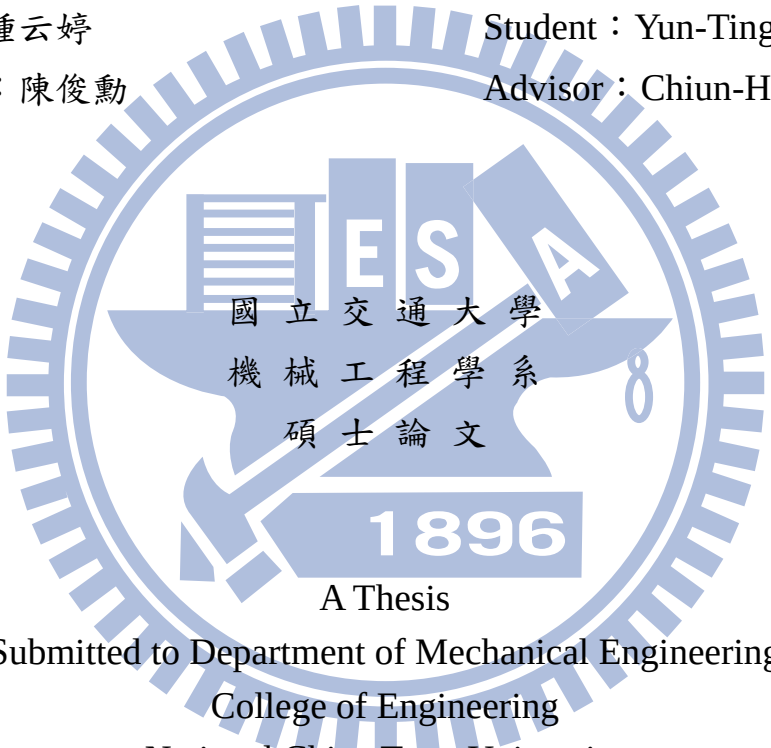

國立交通大學

機械工程學系

碩士論文

A Thesis

Submitted to Department of Mechanical Engineering

College of Engineering

National Chiao Tung University

In Partial Fulfiillment of the Requirements

For the Degree of

Master of Science

In Mechanical Engineering

June 2011

Hsinchu, Taiwan, Republic of China

中華民國一〇〇年六月

Water Management and Thermal Distribution Analyses of Graphite and PDMS Air-breathing PEMFC

石墨及 PDMS 呼吸式質子交換膜燃料電池之水管理與熱分佈分析

學　生：鍾　云　婷　　指導教授：陳俊勳

國立交通大學機械工程學系

摘要

本文主要為研究以 PDMS 與石墨質子交換膜燃料電池之實驗測試，探討反應面積為 5 公分×5 公分的單電池。第一部分是 PDMS(聚二甲基矽氧烷)單電池之研究，實驗參數包括流量及其對應之氫氣利用率以及組裝時鎖合扭力的影響；第二部分是石墨單電池的研究，實驗參數包括流量、鎖合扭力以及電池溫度的影響，此兩部分實驗皆用熱顯像儀拍攝陰極溫度分佈；另外，PDMS 與石墨燃料電池都經由長時間 24 小時放電測試以觀察其耐久度。最後，本論文將 PDMS 與石墨燃料電池做性能的比較與分析。

由實驗結果可知，PDMS 與石墨燃料電池的性能都隨著流量的增大而增大，但 PDMS 燃料電池到達 60sccm 和石墨燃料電池到達 40sccm 以上，性能就不會再增大；PDMS 燃料電池的氫氣利用量是 60sccm，因此熱顯像儀拍攝出的溫度分布在此流量時較均勻；電池組裝之鎖合扭力必須在不使流道結構變型的情況下增加才能有效提升其性能；石墨燃料電池的性能會隨著電池溫度的增加而增加，到達 60℃以上，性能會隨著溫度的增加而減少；PDMS 燃料電池堆經過二十四小時長時間測試後，都有良好的耐久度，但是石墨的卻不穩定，但若將石墨電池溫度加熱至 60℃，即有穩定的輸出；經比較後，在同樣的條件下和同樣的阻抗下，PDMS 燃料電池皆比石墨燃料電池性能表現佳；由於 PDMS 燃料電池有比較少的積水現象，因此比石墨燃料電池更適合用在呼吸式燃料電池上。

關鍵字：PDMS，石墨，質子交換膜燃料電池，氫氣利用量，熱顯像儀，鎖合扭力，電池溫度

Water Management and Thermal Distribution Analyses of Graphite and PDMS Air-breathing PEMFC

Student: Yun-Ting Chung Advisor: Prof. Chiun-Hsun Chen

Department of Mechanical Engineering

National Chiao Tung University

ABSTRACT

This study fabricated PDMS (Polydimethyl Siloxane) and graphite PEMFC (Proton Exchange Membrane Fuel Cell). The active area of the membrane is 5cm×5cm. Firstly, a series of performance experiments on a single PDMS air-breathing PEMFC were carried out and demonstrated. The experimental parameters included flow rate with the corresponding hydrogen utilization and clamping force. Secondly, the similar performance experiments on single graphite air-breathing PEMFC were also carried out and illustrated. The experimental parameters consisted of flow rate, clamping force and cell temperature. For both experimental studies, the corresponding thermal imagines of resultant temperature distributions on the cathode surface were given as well. In addition, in order to justify the durability of continuous usage and water produced situation, both fuel cells mentioned above were tested for 24 hours at a fixed operating voltage. Finally, we made a comparison between PDMS and graphite PEMFCs to see the performance difference and the advantage.

The experimental results show that both the performances of the single PDMS and graphite air-breathing PEMFC increase with an increase of flow rate, but have no further obvious improvements when the

flow rates are greater than 60sccm and 40sccm, receptivity. The hydrogen utilization of the single PDMS PEMFC is 60sccm, and the corresponding thermal image show its temperature distribution being more uniform; An appropriate clamping torque should be considered carefully to enhance the performance without narrowing the fuel flow channels; The performance has significantly improved as increasing graphite fuel cell temperature, however, it starts to decrease as the cell temperature above 60℃; The single PDMS fuel cell can maintain a stable power output for a long time use up to 24 hours. One the contrary, the single graphite air-breathing PEMFC cannot, but it can maintain a stable power output when the cell temperature is raised to 60℃ manually; The PDMS PEMFC has a better performance than that of the graphite one under the same conditions and the same resistance; PDMS is a better material than graphite for air-breathing fuel cell because it has less water flooding effects and possesses a better performance.

Keywords: PDMS, Graphite, PEMFC, Hydrogen Utilization, Thermal Imaging Analyzer, Clamping Force, Cell Temperature

Acknowledgements

最感謝我的指導教授　陳俊勳，除了論文的指導外，也教導我很多做人處事的道理，不斷的磨練我的心智，使我更加的堅強，這是我兩年中所獲得最大的淬鍊。感謝燃料電池國科會的計畫經費及 Lab506 支持我做此研究。感謝阿貴學長在研究上不厭其煩的教導，因為學長從容的態度，才使我擔憂的心情得到舒緩。感謝義嘉學長細心的指導，使我的研究之路更加順遂。感謝昶安、宗翰、家維、瑭原、金輝學長平日的幫忙，感謝同屆的聖容、嘉軒、世庸、黃鈞一起同甘共苦，讓我的學習之路不孤單，感謝凌宇、詠翔、鉦鈞、天洋學弟的平日的幫忙，讓口試能順利進行。最後要感謝我的父母、妹妹、信志、牛頓室友們，你們永遠是我心靈的避風港，沒有你們的陪伴，也不會有今日的我，在這兩年期間，你們扮演非常重要的角色。

Contents

LIST OF TABLE

LIST OF FIGURES

Chapter 1

Introduction

1.1 Motivation and Background:

Fossil fuel is a main source for vehicles in our daily life. A great amount of fossil fuel has been used in the petroleum industrial age, and it almost depletes in recent years. Because of the shortage of fossil fuel, the price of petroleum has been soared as shown in Fig. 1.1. Besides, fossil fuel has some drawbacks: to begin with, the emissions from chemical reactions, like CO_2, CO, CH_4 and N_2O etc., causing acid rain and global warming, pollute our environment; see Fig. 1.2. And the Greenhouse effect is getting more severe, and it becomes a global problem now. Next, when the petroleum discharges or accidently leaks to the ocean, they will hurt or kill the marine life to lead a disequilibrium to the biosphere. Last but not least, the productions of fossil fuel, such as plastics and Styrofoam, etc., cannot dissolute themselves, and they cause severe damage to the land. Most importantly, fossil fuel cannot be a permanent energy source for mankind. Looking for the alternative energy becomes an important issue.

There have been developed several ways to replace fossil fuel in recent years. Nuclear is one of the viable ways, but it is hard to find a material that can endure the high temperature for a long time. Wind and water also can be the sources of power, but they have limitations of land. Geothermal energy resources and bio-fuels are not good enough to generate electric power still. Some researchers will consider gas-electric hybrid for vehicles, but it is not a permanent choice eventually. As a consequence, fuel cells are the best way to supply electricity. Because the hydrogen can be fully supplied without

depletion, fuel cells become the most important research topics in 21st century.

The fuel cells can become such promising devices nowadays because they have a lot of advantages. They combine many advantages of both combustion engines and batteries, like high energy densities and highly reliable. They also have their own advantages: no-pollution, no moving parts, silent and quickly recharged by refueling. There are five major types of fuel cells operating at different temperature regimens (see Table 1.1): the phosphoric acid fuel cell (PAFC), the proton exchange membrane fuel cell (PEMFC), the alkaline fuel cell (AFC), the molten carbonate fuel cell (MCFC) and the solid-oxide fuel cell (SOFC). Among them, the PEMFC is the most attractive one due to its low temperature operation and high power density that can be started and stopped quickly at the room temperature. In addition, it is a good electricity supply device, ranged from W to KW. For example, mobile phones, lap-top, personal computer, portable generation, household appliances, vehicles and other electronic equipments can be used with the PEMFC widely.

Table 1.1 Major Fuel Cell Types [1]

	PEMFC	PAFC	AFC	MCFC	SOFC
Operating temperature	80℃	200℃	60-220℃	650℃	600-1000℃

PEMFC can be divided into two categories according to the fuels supplied: methanol and the hydrogen. The methanol is liquid and the hydrogen is gas. The methanol type of PEMFC is called the direct methanol fuel cell (DMFC). It was under extensive investigation in 2005, but it has some drawbacks. It is harmful to the human health, and it also produces CO to poison Pt catalyst and CO_2 to cause the Greenhouse effect. Besides, it has lower performance than

that of PEMFC, because of the slower fuel anode reaction process. On the contrary, the PEMFC with hydrogen has a higher open circuit voltage (OCV) and produces water only that cannot be a problem to our life, so the application of hydrogen fuel in PEMFC is more preferred.

The PEMFC employs a proton exchange membrane as an electrolyte, which is a solid polymer. It is located between anode and cathode, which are porous graphite. Such anode-membrane-cathode sandwich structure is called a membrane electrode assembly (MEA), whose entire thickness is less than 1 mm.

The electrochemical reactions in the PEMFC are as following:

$$\text{Anode: } H_2 \rightarrow 2H^+ + 2e^-$$

$$\text{Cathode: } \frac{1}{2}O_2 + 2H^+ + 2e^- \rightarrow H_2O + \text{heat}$$

$$\text{Overall: } H_2 + \frac{1}{2}O_2 \rightarrow H_2O + \text{heat}$$

The hydrogen reacts at the anode that is catalyzed by the catalyst, Pt. After reaction, the products are hydrogen ion H^+, which reacts with oxygen at the cathode to generate water and heat, and electron e^-. And the corresponding internal temperature range is less than 90˚C.

In this research team of Chen, Chung [2] used the MEMS (Micro Electro Mechanical Systems) technology to fabricate the single micro PEMFC on silicon-based wafer in order to accomplish a better performance of PEMFC. Unfortunately, the structure of silicon-based flow field plate was too friable to crack while assembling, and its inelastic property easily causes the gas-leaking problem. Hsu [3] used a better material, Polydimethyl Siloxane (PDMS; $(H_3C)_3SiO\,[Si(CH_3)_2O]_n\,Si(CH_3)_3$), to replace the silicon-based one for the micro PEMFC. This material has good biocompatibility, nontoxicity, opaque, hydrophobicity, plasticity and has low heat conduction coefficient, etc. Besides,

it can combine the gasket and flow field together. It can keep fuel cell maintained at a higher temperature to prevent water from condensing that solves water management problem because PDMS is not a good heat conductor. Then, the PEMFC has better performance without the formation of water droplet. Therefore, this thesis continues the effort to apply PDMS in a $5\times5cm^2$ reaction area of the air-breathing single PEM fuel cell to mitigate water flooding problem. In addition to the performance tests, thermal imaging analyzer is used to find the temperature distribution in the cell.

1.2 Literature Review:

There are a lot of research subjects to investigate the factors to improve the fuel cell performance, such as air movement, system considerations, system integration, load handling, fuel delivery, water removal, uniform temperature distribution, homogeneous fluid distribution, good current transport, high conductivity and materials.

Meyers and Maynard [4] used a miniaturized fuel cell integrated on a silicon substrate. There were two designs, one was a bilayer design, which was like sandwich structure that the anode and cathode was separated; another design was a monolithic design that the anode and cathode was on the same substrate. Comparing with the two designs, they found that the power density of a bilayer design is much better as shown in Fig.1.3.

Noponen et al. [5] introduced a measurement system for mapping of current distribution in a free-breathing PEMFC. The results showed that the operating temperature has a significant influence on the performance of the fuel cell. Furthermore, the free convection is weak at low cell temperature, and the membrane is dry at high cell temperatures. They also showed that under some

conditions the fuel cell has homogenous current distribution and does not need any auxiliary pumps or fans to increase the airflow.

The paper by Shah, Shin and Besser [6] was the first report using PDMS as the base material in micro fuel cell. They manufactured micro flow channels on PDMS by soft lithography, because PDMS was cheaper material comparing to silicon. They also compared Pd catalyst with Pt one and found that Pt catalyst is better than Pd one due to the poorer reaction kinetics of Pd catalyst. The performance of fuel cell is proportional to the humidification of hydrogen stream, the conversion of hydrogen, and the catalyst porosity in electrodes. The loading of catalyst has no influence on the conversion of hydrogen; the conversion of hydrogen is determined by the partial pressure of gases at the outlet measured by the mass spectrometer and the temperature on catalysts. When the temperature on catalysts increases, the conversion of hydrogen is decreased, leading to a poor performance.

Shimpalee et al. [7] established a model of 200 cm^2 serpentine flow-fields with different patterns to make the gas distribution uniform. In this paper, they employed the 3-channel, 6-channel, 13-channel, 26-channel serpentine flow-fields and 26-channel complex flow-field on 200 cm^2 PEMFC as shown in Fig. 1.4. The conclusion was that the performance changes with the number of parallel channels, which is related to the path length. The shorter path length (the higher number of parallel channels) has better performance, less water production and more uniform distribution of current density. However, the performance of 13-channel serpentine flow-field is better than that of the 26-channel one, because it has higher water content in membrane, which leads to a higher proton conductivity. The performances of 26-channel serpentine and 26-channel complex flow-fields are similar, indicating that the performance

is independent of configuration.

Schmitz et al. [8] indicated that the performance of an air-breathing PEMFC is related to the opening size of cathode and the gas diffusion layers (GDLs). They considered three opening ratios of 33, 50 and 80%, and the GDLs with different wetting properties to perform the analyses. Larger opening ratio (80%) produces the higher current density and temperature at corresponding cell potentials. The GDL with the hydrophobic has a better performance than the one with the hydrophilic. The latter absorbs water in the GDL, so the membrane is dry out. On the contrary, the hydrophobic GDL cannot absorb water in the GDL, so it keeps the membrane humidified and blocks the oxygen supply. The best performance for air-breathing PEMFCs is an untreated Toray® GDL, which has a lower contact resistance and higher porosity; it keeps the membrane humidified, but does not block the supply of oxygen.

Jung et al. [9] improved the water management problem and the performances of the air-breathing and air-blowing PEMFCs at low temperature by adding hydrophilic SiO_2 particles to the anode catalyst layer. The conclusion was that the performance of air-blowing PEMFC is higher than that of the air-breathing one due to the good transportation of air at the cathode. The performance becomes highest with 100% humidification at the anode; on the other hand, the performance becomes the lowest with flooding at the cathode. The advantages of SiO_2 are that the back diffusion of water to the anode can be enhanced and the water at the cathode can be removed by absorbing water to the anode.

Chen et al. [10] used rapid prototyping (RP) technology to build a new 10-cell air-breathing miniature planar array fuel cell stack, which has a volume

of 6cm×6cm×0.9cm, and the active area was 1.3cm×1.3cm in each individual MEA. The flow field plate was made of acrylonitrile-butadiene-styrene (ABS) by plastic injection molding technology. The RP technology is much faster and cheaper than the conventional CNC and MEMS. The peak powers of the parallel connected and serial connected stack are 99mWcm^{-2} at 0.425V and 92mWcm^{-2} at 4.25V under free convection (at 70℃), and 123mWcm^{-2} at 0.425V and 105mWcm^{-2} at 5.25V under forced convection. The parallel connected stack has higher power density than the serial one, and the performance under forced convection is higher than that of free convection.

Ito et al. [11] developed an evaluation method based the ratio of liquid water to pore volume in GDL. They measured the differential pressure through the interdigitated fuel cell to estimate the liquid water ratio in GDL. The differential pressure was measured by ac impedance method that measuring the ionic resistance in polymer electrolyte membrane, and the water saturation was related to the operation condition of fuel cell. The variables included the material of GDL, load current, gas utilization ratio and humidification temperature. The conclusion was that the performance of cloth-type GDL is higher than that of paper-type one, and the water saturation is proportional to the load current, gas utilization ratio and humidification temperature.

Wen and Huang [12] presented a new method to discharge the waste heat to ambiance by using the pyrolytic graphite sheet (PGS) in a single fuel cell. The PGS is a thermal conduction material, playing an important role as a heat spreader, and the advantages are less volume, light weight and cost reduction by reducing the ancillary components. The heat transportation and temperature distribution are better with PGS than the ones without PGS. When increasing

the oxygen flow rates, more water is removed from the membrane and it becomes dehydrated. The use of PGS increases the water condensation due to the temperature decrease by conduction, so the membrane becomes hydrated. The conclusion was that the PGS increases the water droplets under the high flow rates and dry conditions.

Pandiyan et al. [13] developed an analytical method to understand the thermal and electrical resistances of PEMFC, which were determined by the mass balance and polarization curve, respectively. Thermal and electrical resistances of the electrode are 67.7 and 52mΩ in a four cells stack, respectively. When the increase of thermal resistance is three times, the current increases 50% and the temperature change is 10℃. The electrode fabrication process can change the internal resistance of the fuel cell stack, which is a major key in thermal management.

Siu and Chiao [14] used PDMS as the material of gasket and electrode in microbial fuel cell. They used MEMS technology, such as etching and evaporation processes, to form the microchannel pattern on the silicon wafer, and to mold PDMS on the wafer. Comparing with the recent silicon micromachined microbial fuel cell, their result showed the better performances in the average power density and average current density.

Song et al. [15] used PDMS to fabricate planar PEM fuel cells. They measured current density at different flow rates. The result showed that the current density is a decreasing function of flow rate because the residence times for protons reaching the cathode are shorter at higher flow rates. Since the distance between anode and cathode must be as short as possible, they used Nafion membrane, whose thickness was only 200~400nm. The current density

increases 166% compared to the other planar membrane device.

According to [12], Wen et al. [16] used PGS in a 10-cell stack with 100 cm^2 active area. The temperature variation was measured by four thermocouples on the cathode gas channel plate. The result showed that the temperature distribution becomes uniform in fuel cell stack with the PGS, indicating that PGS is a good thermal management material. And the maximum power of fuel cell stack with the PGS increases 15%.

Bussayajarn et al. [17] applied three different cathode geometries with the same opening ratio: parallel slit, circular open and oblique slit as shown in Fig. 1.5. The performance and stability were investigated with the different cathode geometries. The circular open design is found to be the best in performance and current density, and the performances of parallel slit and oblique slit design are similar, because the shorter rib distance and hydraulic diameter can result in better oxygen transportation and uniform oxygen distribution. The oblique slit design shows high stability, on the contrary, the parallel slit and circular open design are unstable. Both the performance and stability are better in forced convection condition than in self-breathing condition.

Dai et al. [18] surveyed the papers related to water transport and balance in the MEA of PEMFCs. The parameters included operating conditions, component designs and material properties. The major rule of the water balance depends on the materials of water management properties and the components matching operating conditions and load requirements. The data of materials and components in MEA were insufficient, so it was difficult to optimize the design of MEA. It needs to develop a new material for water management capability and to design a component structure and water balance models. Water balance influences not only the performance but also the

durability in both experiment and modeling.

Karst et al. [19] used different cathodic cover opening ratio to manage water content for micro air-breathing PEMFCs. It was a method which decreased the flooding at the cathode and increased the water back-diffusion at the anode by varying the cover opening ratio. The new method didn't require any control tool and didn't increase the volume of cell, either. The total closure of the cover maintains the water accumulated at the cathode. The 5% of cover opening ratio maximizes the back-diffused water and produces 33% of total water at 150mA cm^{-2}.

Pomfret et al. [20] used a Si-charge-coupled device (CCD), camera-based and near-infrared imaging system, to observe the anode processes in the solid oxide fuel cell. A Si-CCD camera-based NIR imagining system was the first equipment using at the Ni/YSZ cermet anodes. The benefit of the NIR imagining system was cheaper, lighter and more sensitive than mid-IR imaging system. Most importantly, it was easier and quicker to observe the operation and processes in SOFCs under various conditions. And the result showed that the temperature drop is due to the presence of oxides and water in SOFCs.

Kim et al. [21] used the thin flexible printed circuit board (FPCB) as a current collector in order to reduce an air-breathing monopolar stack's volume. They also designed different patterns of air-breathing holes on the cathode to find the effect of varying the geometry and opening ratios on stack performance as shown in Fig. 1.6. They found that in cathode, the circular-hole pattern with opening ratio of 38% has the best performance; on the other hand, the rectangular cathode opening pattern with 65% opening ratio causes cathode flooding and unstable output problems.

Yu et al. [22] attempted to reduce the cell resistance and improved the

performance of miniature silicon wafer fuel cells. Three different thicknesses of current collector were selected. They found that the thicker the current collector, the better the cell performance. It is because an increment of the current collector thickness increases the area of conductor, which decreases the cell resistance and improves the cell performance.

Zhang et al. [23] used two effective methods, FEM analysis and simplified prediction method, for estimating the contact resistance between the bipolar plate and GDL. The predicted results by both methods show the good agreement with the experimental ones. The contact resistance is influenced by the average clamping pressure and the assembly clamping pressure distributions.

Chang et al. [24] studied the effects of the clamping pressure on the performance of PEMFC. The contact electrical resistance is a function of the clamping pressure, so it is necessary to assemble a fuel cell with a proper force. The results showed that increasing the clamping pressure reduces the interfacial resistance and enhances the electrochemical performance of a PEMFC at the low clamping pressure levels. In contrast, increasing the clamping pressure reduces the Ohmic resistance, but meanwhile narrows down the mass diffusion path from gas channels to the catalyst layers at the high clamping pressure levels. The above two effects make the power density not to rise due to the lower mass-transfer limitation for higher current density.

Zhou et al. [25] investigated the effect of clamping force on the performance of PEMFC that directly affects the interfacial contact resistance, non-uniform porosity distribution of GDL, GDL deformation and reactant transport in GDL. They used finite element method (FEM) to analyze the elastic deformation of GDL and porosity distribution, and finite volume method (two-phase flow model) to analyze the mass transport of reactants and products.

The results showed that the contact resistance plays an important role at a low clamping force in determining the power density because the contact resistance decreases obviously with increasing clamping force. But at a high clamping force, the contact resistance decreases slightly with an increasing clamping force, and now the GDL deformation plays a main role. As the GDL porosity decreases, the transport resistances of gas and liquid water increase. Accordingly, the power density decreases with an increase of clamping force when the influence of GDL porosity is more significant than that of Ohmic contact resistance.

Wen et al. [26] applied the pressure-sensitive films (FUJI-FILM I&I) to observe the internal contact pressure distributions under three different clamping torques (8, 12 and 16 N-m) and three different bolt configurations (2, 4 and 6-bolt configurations). When the torque was applied, the pressure-sensitive film was broken and a color-forming material was released and absorbed by the film. The pressure film was then transferred into a color image file that was compared with the reference color bar to obtain the pressure values. The results showed that the larger mean contact pressure and more bolt numbers, the higher maximum power. The uniformity of the contact pressure distribution is improved and the contact ohmic resistance is reduced when increasing the mean contact pressure and bolt numbers. However, the maximum power does not increase linearly with the bolt numbers and torques. In fact, it increases until a certain torque point (e.g. >10 bar) is reached, and further increasing the clamping pressure not only reduces the contact ohmic resistance but also narrows down the mass transfer path from gas channels to the catalyst layers.

Lee and Chu [27] applied a finite volume-based CFD approach to investigate the behavior in a fuel cell. The effects of cell temperature and

humidification temperature influence the location of the gas-liquid interface (defined as the location where the liquid water begins to condense), the cell performance and the distribution of liquid water saturation. The results indicated that the humidification temperature slightly higher than the cell one is the best working condition. It is because that in such condition, liquid water forms when the inlet gases enter the channel, some of the liquid water keeps the membrane moist to enhance its ionic conductivity.

Matian et al. [28] used a thermal imaging camera to study the temperature distribution and variation on the outer surfaces of PEM fuel cell. One important parameter, namely the surface emissivity factor, that needed to be identified in advance. A calibrated thermocouple was put on surface and the temperature was recorded, then, emissivity factor in the camera settings was altered until the temperature measured by the camera agreed with the one by the thermocouple. They obtained the emissivity factor of 0.88, and this value did not change throughout the experiments. The results showed that the temperature distribution in the stack is not only affected by convection in the gas flow channels but also by natural convection and conduction; about 50~60% of the heat is dissipated by natural convection.

Zhang et al. [29] operated a PEMFC without external humidification (0% relative humidity) to eliminate the gas humidification system and decrease the complexity of the fuel cell system. The performance at 100% RH is higher than that at 0% RH, because the membrane needs to be humidified to carry hydrogen ions. The results showed that the cell performance at 0% RH decreases with the increasing operation temperature and reactant gas flow rate and a decreasing operation pressure.

Ous and Arcoumanis [30] used 25 cm^2 reaction area of the air-breathing

single PEM fuel cell to investigate the formation of water droplets and their aggregation in the cathode under various operating parameters, such as air and hydrogen stoichiometry, cell temperature and external load. The stoichiometry of air and hydrogen causes droplets aggregation and makes fewer droplets extraction. In contrast, the temperature and external load have the effects on removing water, and the temperature is especially an obvious operating parameter. The formation of water droplets is reduced as the temperature increases, but the over-temperature can cause the membrane dehydrated.

1.3 Scope of Present Study

In this study, the materials of PDMS and graphite are used for the flow field plates to improve the water management in the 5×5 cm^2 reaction area of the air-breathing single PEM fuel cells. The use of a 25 cm^2 air-breathing cell can observe the temperature distribution more easily, and the air-breathing one can reduce the auxiliary oxygen supply system.

The research flow chart is given in Fig. 1.7. The experimental parameters included the material, flow rate, clamping force and cell temperature. The temperature distribution images on cell surfaces were obtained by using a thermal imaging analyzer. The data of hydrogen utilization were deduced by the measurements from mass flow meters. The contact and ionic resistance was measured by an Ohm Tester. The I-V (I-P) curves and durability data were recorded by the test station. Those measured data are used to evaluate the performances of the manufactured fuel cells. After a series of performance tests were carried out, the performance comparisons by using PDMS and graphite flow field plates are given as well. In addition, the comparison with other work, such as Zhang et al. [29], Chang et al. [24] and Ous and Arcoumanis

[30], are made as well.

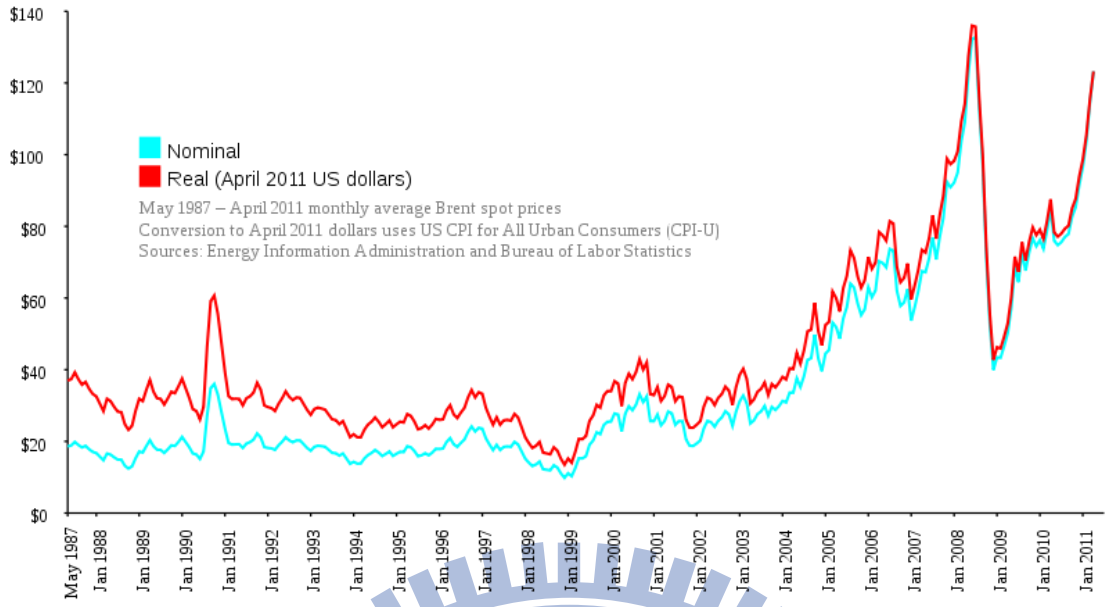

Fig. 1.1 The Petroleum's Price in Recent Year
http://en.wikipedia.org/wiki/Price_of_petroleum

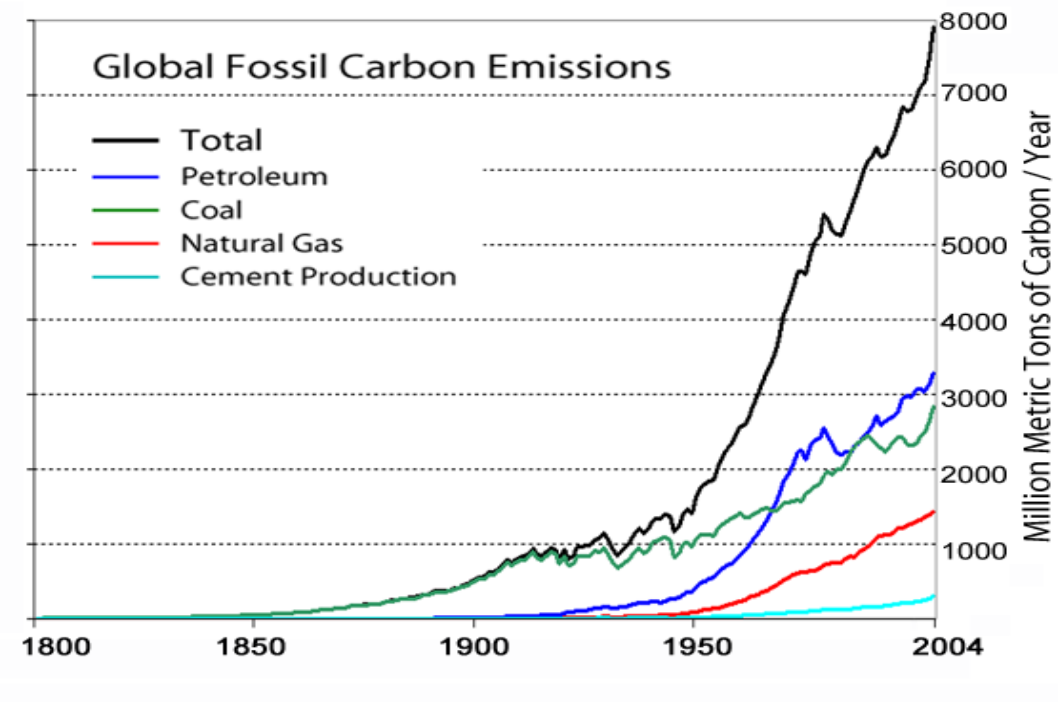

Fig. 1.2 Global Fossil Carbon Emissions in Recent Years
http://en.wikipedia.org/wiki/Greenhouse_gas

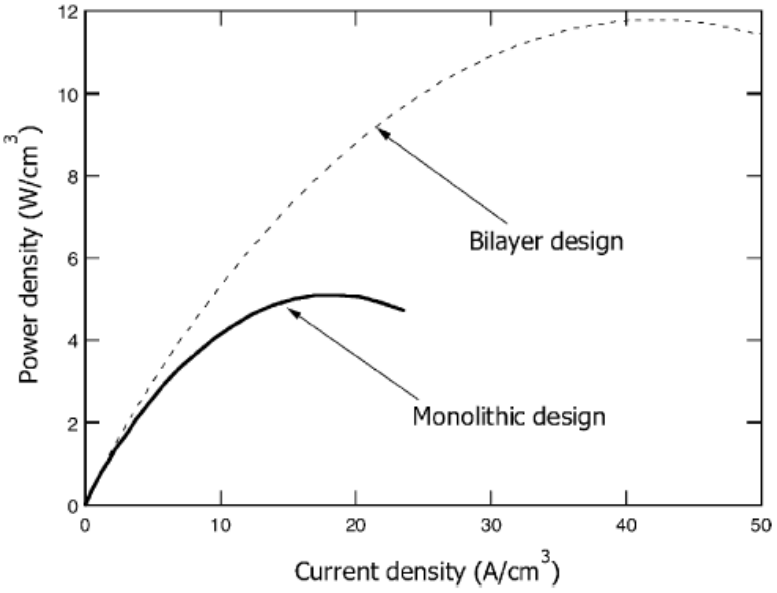

Fig. 1.3 Comparison of Power Densities for Bilayer and Monolithic Design [4]

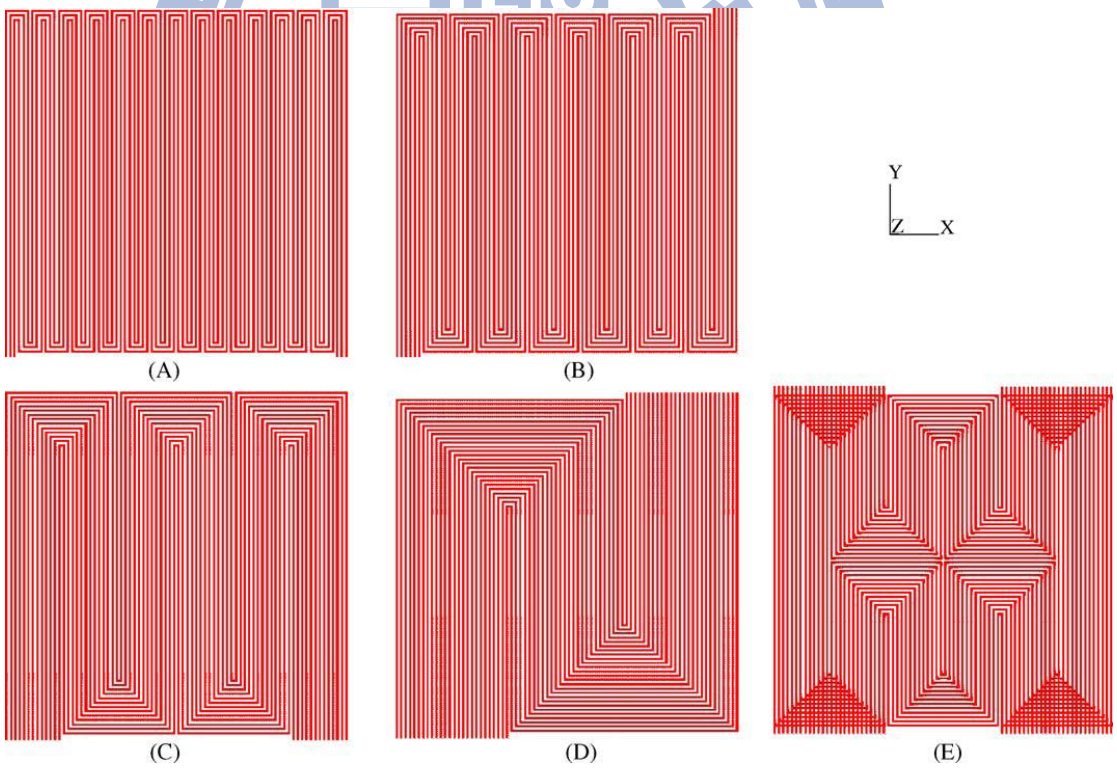

Fig. 1.4 Flow Field Patterns of Anode and Cathode on 200 cm^2 PEMFC: (A) 3-Channel Serpentine Flow-Field; (B) 6-Channel Flow-Field; (C) 13-Channel Flow Field; (D)26-Channel Flow Field; (E) 26-Channel Complex Flow-Field [7]

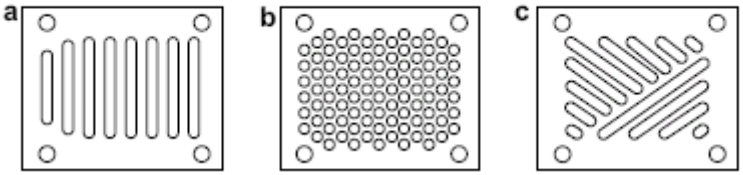

Fig. 1.5 Three Different Open Cathode Designs: (a) Parallel Slit (b) Circular Opening and (c) Oblique Slit [17]

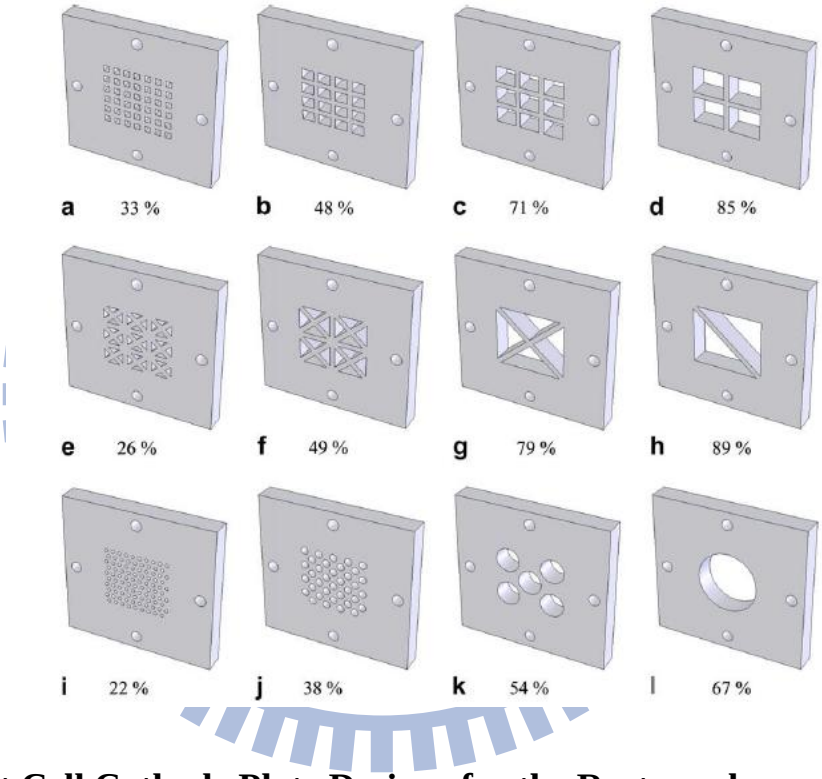

Fig. 1.6 Unit Cell Cathode Plate Designs for the Rectangular, Triangular and Circular Opening Geometries at Various Opening Ratios [21]

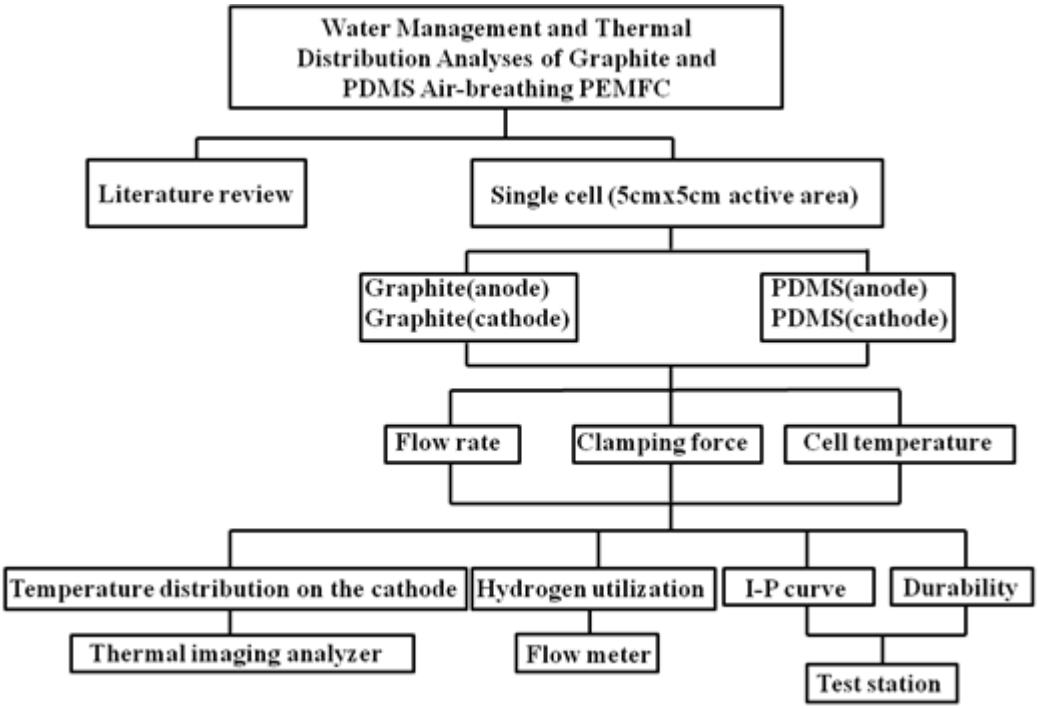

Fig. 1.7 Research Flow Chart

Chapter 2

Fundamentals of Fuel Cell

2.1 History of Fuel Cell:

The origin of fuel cell can be traced back to the 19 century. In 1839, a scientist also a lawyer named William R. Grove who had the first concept of a fuel cell. The idea of fuel cell came from the experiment of water electrolysis. He used electricity to electrolyze water into hydrogen and oxygen, and then took the reverse reaction that it generated a small current that established the foundation of the fuel cell. The electrolysis and the reverse of electrolysis are as follow:

$$\text{Electrolysis:}\quad H_2O + \text{electricity} \rightarrow H_2 + \frac{1}{2}O_2$$

$$\text{Reverse reaction:}\quad H_2 + \frac{1}{2}O_2 \rightarrow H_2O + \text{electricity}$$

In 1889, L. Mond and C. Langev employed a metal Pt as the catalyst to fabricate the first fuel cell which could generate 3.5mA/cm^2 at 0.73V. Therefore, the formal name of “fuel cell” had come up at that time.

In 1932, Francis Bacon used Ni as the catalyst to replace Pt and alkaline electrolyte which was different from Mond and Lavgev’s. He invented the “bacon battery” which was based on Mond and Lavgev’s. In fact, the bacon battery is the first alkaline fuel cell. In 1959, both Bacon and Allis-Chalmers companies used the machines driven by fuel cells, the development of fuel cell became commercialization since then and it helped fuel cell became more realistic in the future.

During 1960~1970, NASA found out a proper main power source, hydrogen fuel cell, for spaceship. Because the power was suitable for the

spaceship and the produced water could supply astronauts to drink in the outer space. In 1976, a new polymer membrane called Nafion came out, and it was registered by DuPont. In 1993, Ballard power system company invented the first automobile in the world that powered by fuel cells. But the development of fuel cell is not complete yet.

Nowadays, the flooding situation is still a main problem for air-breathing type of fuel cell, because it becomes difficult to breathe when the water blocks air supply to gas diffusion layer and then it decreases the voltage. Thus it takes a long time for fuel cells to be realistic in commercialization. Fortunately, we can use thermal imaging analyzer to observe the temperature distribution to indicate water flooding situation and then use PDMS to solve the flooding problem.

2.2 Principle of the Fuel Cell

2.2.1 Thermodynamics

Fuel cell converts chemical energy into electrical energy directly, so it is more efficient than heat engines. The maximum theoretical efficiency of a heat engine is described by the Carnot cycle as follow:

$$\varepsilon_{Carnot} = \frac{T_H - T_L}{T_H},$$

where T_H is maximum temperature and T_L is the rejection temperature of the heat engine. For example, a heat engine operates at 675K and rejects heat at 325K, the resultant Carnot efficiency is 52%.

The ideal efficiency (ε) of a fuel cell is the amount of useful energy that can be extracted from the reaction relative to the total heat energy released by the reaction in combustion:

$$\varepsilon = \frac{\Delta G^0}{\Delta H^0}$$

For example, ΔH^0 is -285.83KJ/mole for the hydrogen/oxygen reaction and ΔG^0 is -237.14KJ/mole at standard conditions, so the ideal efficiency is 83%.

But the real efficiency of fuel cell is lower than the ideal one due to the voltage and the fuel utilization losses. The real efficiency of fuel cell may be expressed as:

$$\varepsilon_{real} = \varepsilon_{ideal} \times \varepsilon_{voltage} \times \varepsilon_{fuel}$$

where ε_{ideal} is the ideal efficiency of the fuel cell, $\varepsilon_{voltage}$ the voltage efficiency and ε_{fuel} the fuel utilization efficiency.

The energy can be expressed as an electrical potential or standard-state reversible voltage (E^0) when ΔG^0 represents the amount of useful energy that can be extracted from the fuel cell at standard condition, and the relation equation is:

$$E^0 = \frac{\Delta G^0}{2F}$$

The reversible voltage of hydrogen-oxygen is 1.23V at standard condition, which is the open circuit voltage (OCV).

The open circuit voltage of the fuel cell depends on the operating conditions, because ΔG is a function of pressure and temperature. When the case is not under standard condition, these dependencies can be described by the Nernst equation:

$$E_{Nernst} = E^0 - \frac{RT}{2F} \ln \frac{P_{H_2O}}{P_{H_2} P_{O_2}^{\frac{1}{2}}}$$

It provides us to observe how the voltage changes with the partial pressures of reactant and product. However, the real voltage of fuel cell is lower than the ideal one due to the irreversible kinetic losses and the fuel utilization losses.

2.2.2 Kinetics

The ideal voltage of fuel cell is determined by the Nernst equation, but the real voltage output is less than the ideal one. In the real fuel cell, the more current outflow is drawn, the more voltage output loses and it declines the total power. There is a graph of fuel cell that incorporates current and voltage characteristics called a current-voltage (I-V) curve (Fig.2.1), which can illustrate the performance of real fuel cell. From this curve, it can know the real voltage output of the fuel cell at a given current output.

According to the I-V curve, it is difficult to keep a high voltage at the higher current due to irreversible losses, and there are three types of losses for fuel cell, which can be identified in I-V curve (see Fig 2.2):

1. Activation losses
2. Ohmic losses
3. Concentration losses

The activation losses are due to electrochemical reaction in the initial section, the ohmic losses are due to ionic and electronic conduction in the middle section, and the concentration losses are due to mass transport in the last section of the curve.

There is an equation that can predicate the real voltage output of fuel cell based on the ideal voltage output minus three kinds of losses:

$$E_{real} = E_{Nernst} - \eta_{act} - \eta_{ohmic} - \eta_{conc}$$

where E_{real} is the real voltage output, E_{Nernst} the ideal voltage output, η_{act} the activation losses, η_{ohmic} the ohmic losses and η_{conc} the concentration losses. These three types of losses will be discussed as follows.

2.2.2.1 Activation Losses

The voltage output decreases rapidly at the lower current density, because the electrochemical half reactions at the anode and cathode electrodes are slow. The oxygen reduction reaction at the cathode is especially slow that is the main reason that voltage output decreases rapidly at lower current density.

Although the free energy of products is lower than that of reactants, reaction rates are still limited. Because there exists an energy barrier called activation energy between the reactants and products, it impedes reactants to convert into products. In order to lower the energy barrier, a part of generated voltage must sacrifice to increase the rate of reaction and the current output. The Butler-Volmer equation can describe the relationship between the current density output and activation overvoltage.

$$i = i_0 \left(\frac{C_O}{C_O^*} e^{-\frac{\alpha F \eta_{act}}{RT}} - \frac{C_R}{C_R^*} e^{-\frac{(1-\alpha) F \eta_{act}}{RT}} \right)$$

When the activation overvoltage is over 50mV, the Butler-Volmer can be simplified into a simpler form:

$$i = i_0 \quad e^{-\frac{\alpha F \eta_{act}}{RT}}$$

When it transforms to logarithmic form, it is called the Tafel equation.

$$\eta_{act} = \frac{RT}{\alpha F} \ln \frac{i}{i_0}$$

Activation losses can be reduced by increasing the current density, which is the functions of the catalyst material and the surface area of electrodes. Platinum is the best catalyst material and the highly porous electrodes can expand the reaction surface area. Disperse the nano particles of platinum into the porous electrodes, so the gas phase pores, the electrode and the electrolyte contact intimately. It maximizes the triple phase boundary which increases the

current density.

2.2.2.2 Ohmic Losses

The voltage output decreases in the middle section of the I-V curve because of the internal resistance of materials and the movement of protons and electrons. These section of losses follow Ohms law, V = I R, so it is called "Ohmic losses". The reason that causes ohmic losses is the electrically conductive electrodes and the ion conductive electrolyte. The latter is larger than the former, so the electrolyte influence is the main reason of ohmic losses. Even though there are ohmic losses, the peak power occurs in the middle of I-V curve.

2.2.2.3 Concentration Losses

The voltage output decreases rapidly at the high current density and then drops to zero. When the voltage is zero, the current density output is the maximum current, known as the short-circuit current. Because the voltage output is zero, the total power delivered is also zero. The reason causing concentration losses are the mass transport limitation. The consumed rate of the reactant gases on the reaction surfaces is faster than the one of its supply at the high current density. Due to insufficient of the reactant gases, the partial pressure of the reactant gases reduces to zero. According to the Nernst equation, the partial pressure of the reactant gases drops rapidly, leading the voltage output to zero. The voltage loss caused by the mass transportation limit of reactant can be expressed as:

$$\eta_{conc} = \frac{RT}{nF} \ln \frac{i_L}{i_L - i}$$

where η_{conc} is the concentration losses and i_L is the limiting current density. According to the equation, the concentration losses are due to high current

density. However, the good design of the flow field plate and the highly porous electrodes can mitigate concentration losses and have a better performance.

2.3 Type of Fuel Cell

There are five major types of fuel cells, they are:

1. Phosphoric Acid Fuel Cell (PAFC)
2. Alkaline Fuel Cell (AFC)
3. Solid Oxide Fuel Cell (SOFC)
4. Molten Carbonate Fuel Cell (MCFC)
5. Proton Exchange Membrane Fuel Cell (PEMFC)

These five categories of fuel cell have the same operation principles, but they operate in different temperature and have different electrolyte and electrode materials. In addition, their fuel tolerance and performance characteristics are also different. The detailed differences are summarized in Table 2.1.

Table 2.1 The Five Major Types of Fuel Cells

Type of fuel cell	**PAFC**	**MCFC**	**SOFC**	**PEMFC**	**AFC**
Electrolyte	H_3PO_4	$(Li,K)_2CO_3$	$(Zr,Y)O_2$	MEA	Polymer
Anode	Pt/C	Ni+10wt%Cr	Ni+$(Zr,Y)O_2$	Pt/C, Pt-Ru/C	Pt/C
Cathode	C	NiO	$(La,Sr)MnO_3$,$LaCoO_3$	Pt/C	Pt/C
Ion	H^+	CO_3^{2-}	O^{2-}	H^+	OH^-
Reaction of anode	$H_2 \rightarrow 2H_2O + 2e^-$	$H_2+CO_3^{2-} \rightarrow H_2O+CO_2+2e^-$	$H_2+O^{2-} \rightarrow H_2O+2e^-$ $CO+O^{2-} \rightarrow CO_2+2e^-$	$H_2 \rightarrow 2H_2O+2e^-$	$H_2 + 2OH^- \rightarrow 2H_2O+ 2e^-$
Reaction of cathode	$1/2O_2+2H^++2e^- \rightarrow H_2O$	$1/2O_2+CO_2+2e^- \rightarrow CO_3^{2-}$	$1/2O_2+2e^- \rightarrow O^{2-}$	$1/2O_2+2H^++2e^- \rightarrow H_2O$	$1/2O_2+2H_2O+2e^- \rightarrow 2OH^-$
Operating temperature	160~190°C	600~700 °C	900~1,000 °C	30~80 °C	90~100 °C
Fuel compatibility	H_2	H_2, CH_4	H_2, CH_4, CO	H_2, methanol	H_2
Advantage	CO durability, combined heat and power	high power, combined heat and power, reform the fuel in cell	high power, combined heat and power, air as oxidant, reform the fuel in cell	high density power, air as oxidant, operating in room temperature, fast activation,	Operating in room temperature, fast activation
Disadvantage	operating in high temperature, high cost, low efficiency	device can be corroded	operating in high temperature, damaging in high temperature	high cost, infecting by CO	high cost, fuel is only H_2
Application	distributed generation	large-scale power plant, distributed generation	large-scale power plant, distributed generation, automobile industry	domestic appliances, portable source, automobile	spaceship

Source: Fuel Cell Systems Explained (2003) James Larminie, Andrew

2.3.1 PAFC

The phosphoric acid fuel cell employs liquid H_3PO_4 as an electrolyte, which is in the middle of two porous graphite electrodes coated with a platinum catalyst. Hydrogen is used at the anode and air or oxygen is at the cathode. The PAFCs operate above 42℃, around 180 to 210℃, because the freezing point of pure phosphoric acid is 42℃. The benefit of the phosphoric acid is high thermal, chemical, volatility and electrochemical stability and it also has greater tolerance of CO, which is up to 1%. The PAFC become the first widely used fuel cell in commercial market.

2.3.2 AFC

The alkaline fuel cell employs potassium hydroxide as an electrolyte. It operates at about 200℃, and uses hydrogen at the anode and air or oxygen at the cathode. H^+ is transported from the anode to the cathode in acidic fuel cells, in opposite, OH^- is transported from the cathode to the anode in an alkaline fuel cell. Thus, water is produced at the anode. It is important to remove the excess water; otherwise the performance of AFC will decline. NASA used the AFC in spaceship for a main power source and it also is employed in hydrogen-powered vehicles.

2.3.3 SOFC

The solid oxide fuel cell employs solid ceramic as an electrolyte, and yttria-stabilized zirconia (YSZ) is the common used material. The YSZ has a lot of advantages, such as high porosity, high thermal expansion compatibility, good ion conductivity and mechanical stability. The materials of anode and cathode are different. The anode is made of nickel zirconia, which has high

catalytic activity and good conductivity and the cathode is made of lanthanum manganate, which has high catalytic activity and good oxidation resistance. It operates around 600 to 1000℃, so the electrodes must be able to stand the high temperature environment. The efficiency of the SOFC is only about 50~60%, but it can reach 90% when combining heat and power advices. Therefore, the SOFC is always used in industrial and electricity generating stations.

2.3.4 MCFC

The molten carbonate fuel cell employs a molten mixture of alkali carbonates as an electrolyte, such as lithium and potassium or lithium and sodium carbonates. It uses CO_2 at the cathode and produces CO_2 at the anode, recycling the CO_2 from the anode to the cathode, and the carried ion between the cathode and the anode is CO_3^{2-}. The anode is made of nickel/chromium alloy and the cathode is lithiated nickel oxide that both have high catalytic activity and good conductivity. It operates at about 650℃, which is the high temperature, similar to SOFC. The efficiency of MCFC is about 50%, but it can reach 90% when combining heat and power advices.

2.3.5 PEMFC

The proton exchange membrane fuel cell employs a thin polymer membrane as an electrolyte like plastic wrap, and the most common material is Nafion™. The membrane is between the anode and cathode, which have two sections, platinum-based catalyst and porous carbon electrode. The structure is electrode-catalyst-membrane-catalyst- electrode, which is called a membrane electrode assembly (MEA). Hydrogen is used at the anode, and air or oxygen is used at the cathode. The other type of fuel supply at the anode is methanol

and it is called direct methanol fuel cell (DMFC). It operates at about 90℃, because the polymer membrane must be aqueous with liquid water for ion conduction. The principles of PEMFC and PAFC are the same, but PEMFC is more attractive and a common used power source for automobile than PAFC. It is because PEMFC can start and stop quickly at low temperature and has high efficiency, most importantly, its quantity of power density is suitable for portable applications.

2.4 Fuel Cell Stack

The voltage of a single fuel cell is fixed. The way to enlarge the voltage is to connect the fuel cells together in series that is called "fuel cell stack". The total voltage of the stack is adding the voltages of individual single fuel cell together, so the number of fuel cells of a stack depends on the amount of voltage needed. But the real voltage of fuel cell stack is less than the summed voltages of single fuel cells due to the utilization rate of fuel and the various losses.

2.5 Principle of PEMFC

PEMFC is different from a conventional battery; it converts chemical energy into power energy directly. As long as we supply fuel to the PEMFC, it continuously generates current, in other words, it is just like a transformation machine. There are hydrogen oxidation reaction and oxygen reduction reaction in PEMFC. The oxidation is taken place at the anode, where hydrogen is split into electrons and protons (H^+). Then, the electrons pass through the wire connected with the two electrodes, and the protons (H^+) pass through the electrolyte to reach cathode. The oxygen reduction is occurred at cathode, where the electrons, protons and oxygen are combined together to produce water. The half of electrochemistry reactions are as follow:

$$\text{anode: } H_2 \rightarrow 2H^+ + 2e^-$$

$$\text{cathode: } \frac{1}{2}O_2 + 2H^+ + 2e^- \rightarrow H_2O + \text{heat}$$

$$\text{overall: } H_2 + \frac{1}{2}O_2 \rightarrow H_2O + \text{heat}$$

The process of electron flow is the critical point to generate current, and the amount of current depends on the reaction area of electrodes. Enlarging the reaction area of electrodes leads to larger current. The electrode is usually made into a thin and highly porous structure to increase the surface area that maximizes surface-to-volume ratio.

2.6 Structure of PEMFC

The structure of PEMFC is shown in Fig.2.3, which is like a sandwich structure, and each individual item is described as follow:

2.6.1 Bipolar Plate, Current Collector and End Plate

The voltage of single fuel cell is too small to drive electrical appliances, so connecting several fuel cells in series is a common way to increase voltage. The bipolar plate is a structure to connect the fuel cells in series, and the plate is between the anode of a fuel cell and the cathode of adjacent fuel cell. It is a high conductive plate to collect the current and contains flow channels to uniform gas distribution. It is an important structure to support MEA stably and reduce the difference of gas pressures between the anode and cathode. In the study, we use the PDMS as the material of bipolar plate, but it is not a conductive. And the current collector is next to bipolar plate in order to collect current to outside load. The outer structure is end plate, which fixes all the segments of fuel cell together and keeps the pressure distribution uniformly.

2.6.2 Gas Diffusion Layer (GDL)

The gas diffusion layer is a porous structure to let the gas pass through, and is made of carbon paper or cloth. It has good conductivity for electron and ability to remove water. The scale of the gas diffusion layer is constant, so the contact resistance is small. In addition, it is hydrophobic, so the holes cannot be blocked by water.

2.6.3 Gasket

The purpose of the gasket, made of Teflon-PTFE, is for sealing. It can stand high temperature and corrosion. Most importantly, it can prevent gas leaking from gas diffusion layer.

2.6.4 Proton Exchange Membrane (PEM)

The proton exchange membrane, a very important section of PEM fuel cell, is named as Nafion. The function of PEM is being a path for protons. The proton conductivity is related to the PEM thickness and the amount of water content. The proton conductivity increases when the PEM thickness becomes thinner and the amount of water content is higher. For this reason, it is necessary to keep the PEM thinner and hydrous. Another important function of the PEM is to separate the reactants of anode and cathode, otherwise, the reaction of the hydrogen and oxygen will discharge heat to increase temperature that is dangerous.

2.6.5 Active Layer

The active layer is between the PEM and GDL, the reaction gas flows through the bipolar plate, GDL and active layer in sequence. The active layer is an important segment to convert chemical energy into electrical energy. We

employed the metal platinum (Pt) in the anode and cathode, because it is a good material to activate the electrochemical reaction.

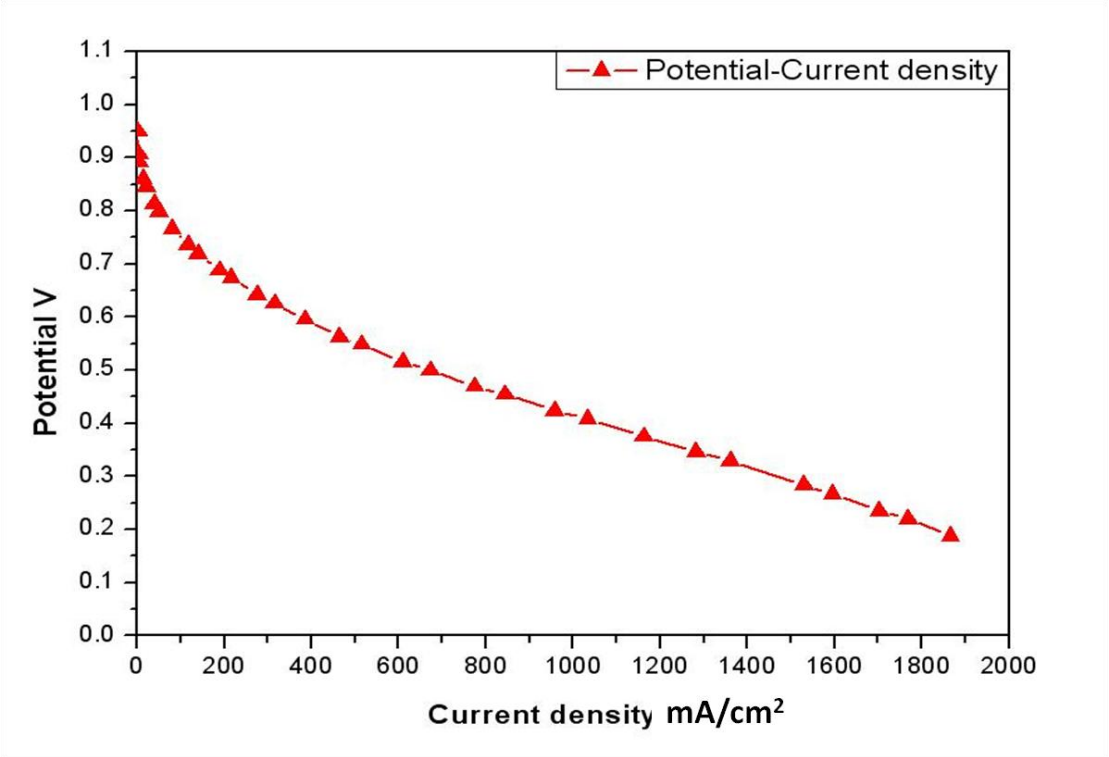

Fig. 2.1 Typical *I-V* Curve For a PEMFC

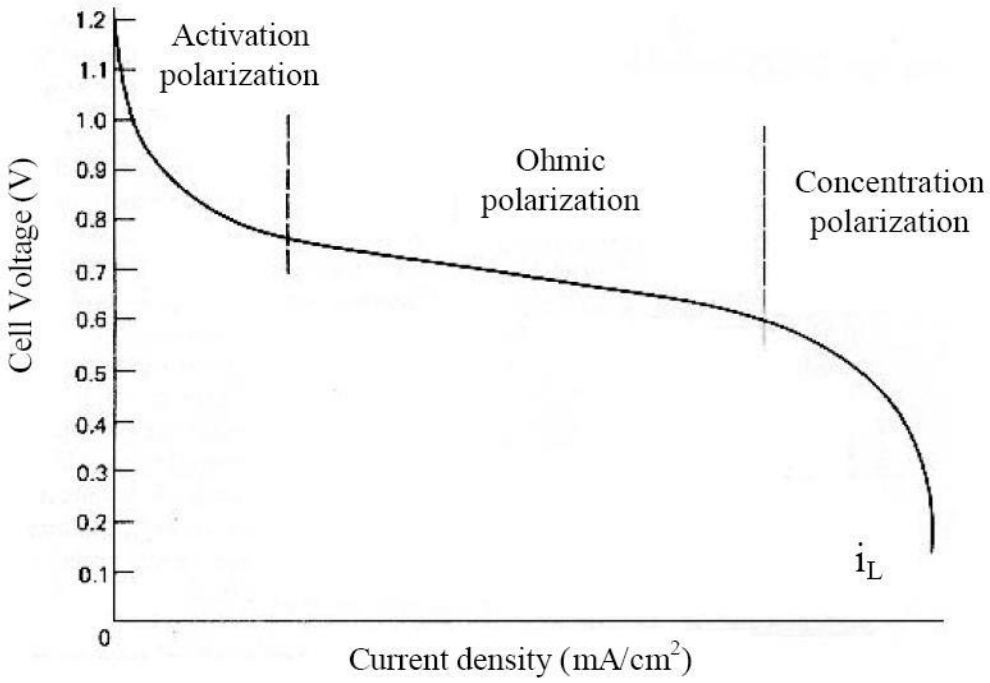

Fig. 2.2 I-V Curve of Fuel Cell

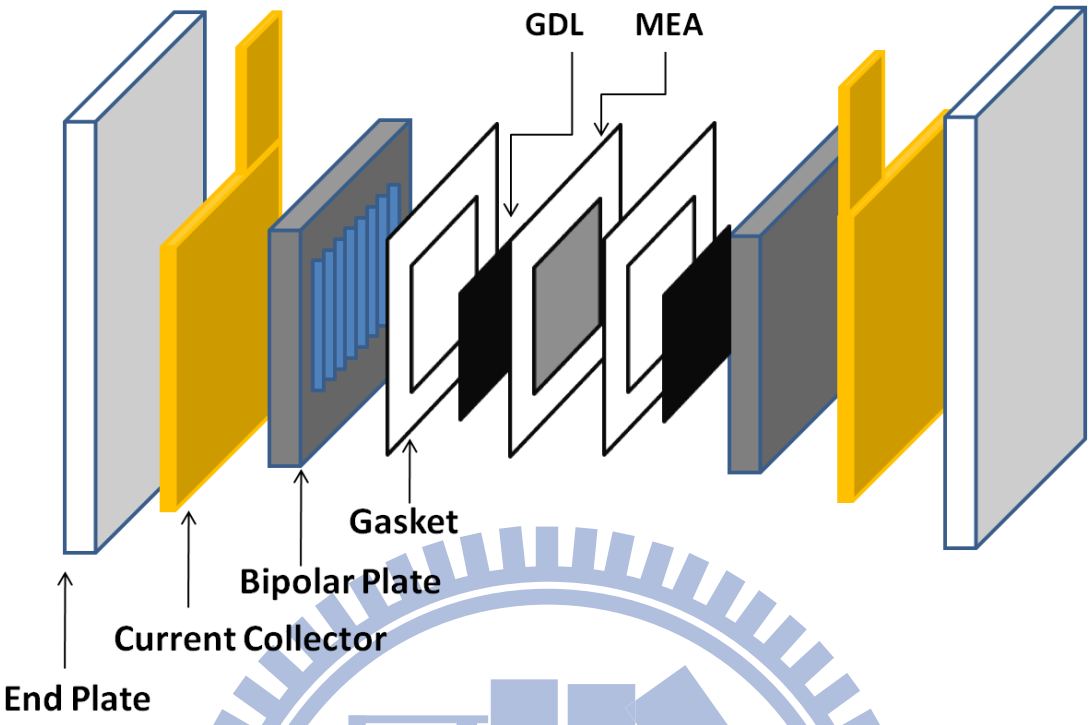

Fig. 2.3 Sandwich Structure of PEMFC

Chapter 3

Experimental Apparatus and Fabrication Processes

3.1 Processes of Fabricating the PDMS Flow Field Plates

The overall fabrication includes two processes: (1) process of fabricating acrylic flow field mold; (2) process of molding PDMS on the acrylic flow field mold. The molding process takes advantage of the fact that PDMS is a fluid at room temperature that is easily converted into solid form by cross-linking upon heating. To begin the molding process, a premixed substance of 10:1 weight ratio of Sylgard polymer base and curing agent is slowly poured on the acrylic mold, and then the acrylic mold is put into the vacuum chamber (see Fig. 3.1). After degassing for 1 hour to remove bubbles before curing, the PDMS is cured at 60℃ for 2 hours and peeled-off from the acrylic mold. Now the PDMS flow field plates are completed; see Fig. 3.2. The patterns of anode flow field plates are introduced into my study from ITRI.

3.2 Assembly and Components of PEMFC

3.2.1 Components of PEMFC

For the PDMS PEMFC, its components include Membrane Electrode Assembly (MEA), Gas Diffusion Layer (GDL), Current collector slices, PDMS flow field plate, and Acrylic plate. For the graphite PEMFC, its components include Membrane Electrode Assembly (MEA), Gas Diffusion Layer (GDL), Current collector plate, Graphite flow field plate, and End plate. Some of them have to be done extra works. For examples, the flow field plates need to be drilled gas inlet and outlet before assembly, and the flow field plate in air-breathing cell needs an extra hole for natural convection. These components

are shown in Figs. 3.3, 3.4 and 3.5, respectively.

3.2.2 MEA and GDL

The MEA used is manufactured by the HEPHAS ENERGY CO., LTD. Fig. 3.3 shows the picture of the MEA and GDL. Its specifications are listed in Table 3.1.

Table 3.1 The Properties of MEA

MEAs DupPont™ Nafion® NRE-212	
Anode Loading (Pt)	0.3 (mg/cm^2)
Cathode Loading (Pt)	0.5 (mg/cm^2)
Active Area	$25cm^2$ (5cm × 5cm)
Typical Thickness (micrometer)	50.8
Basis Weight (g/m^2)	100
Specific Gravity	1.97
Hydrogen Crossover ($ml/min \cdot cm^2$)	< 0.010
Water Content (% water)	5.0 ± 3.0%
Water Uptake (%water)	50.0 ± 5.0%
Linear Expansion (% increase) ***From 50%RH, 23℃ to water soaked, 23℃***	10
Linear Expansion (% increase) ***From 50%RH, 23℃ to water soaked, 100℃***	15

3.2.3 Assembly of Air-breathing PEMFC

The single air-breathing PEMFC consists of bipolar plates, end plates,

current collector slices and membrane-electrode-assembly (MEA), as shown in Figs. 3.6 and 3.7. The structure is like sandwich as shown in Fig. 3.8. Air is used as oxidant supply and driven by natural convection on cathode side. However, the acrylic plate, graphite plate and the PDMS should be designed to match the shape of current collector slices, as shown in Fig. 3.9. The 81-circles of current collector slice are chosen. The air-breathing PEMFC uses natural convection to transport oxidant (air), so the flooding problem must be treated carefully.

3.2.4 Current Collector Slices

The current collector is an important parameter affecting the PDMS PEMFC performance, so the current collector slices are under the same open ratio (the rate of the non-conductive area and the total) are designed. The material used is gold-plated copper. (Fig. 3.10)

3.3 Test Station

A PEMFC test station, as shown in Figs. 3.11 and 3.12, is constructed to evaluate the characteristics of single or stack fuel cell. The components of test station are listed in Table 3.2.

Table 3.2 Instrument of Hardware Specifications

Hardware	***Number***	***Specification / Type***
Controlling Temperature System	5	25~90^{0}C T-type thermal couple
Heater	6	Humidify the gas: 250W Heating fuel cell: 50W Preheating pipe: 180W
Controlling Mass Flow	2	Hydrogen:0-400 sccm

Rate System		Oxygen: 0-2000 sccm
Display of mass flow rate	1	PROTEC PC-540
Valve of Back Pressure	2	250 psi Max
Back Pressure gauge	2	0~150 psi
Adding Humidity Container	2	Volume:1L Pressure:5Kgf/cm^2
Drain Valve	2	AW30-03BD
Switching Power Supply	2	3V,20A 24V,4.5A
Electromagnetic Valve	3	061317X 501062S
Hydrogen Detection	1	COSMOS 0-2000 ppm
19" Instrumental Frame	1	RA3570-0

Some parameters, such as flow rate, humidity and reheat temperature, can be adjusted in this station. After experiments, the testing data, as listed in Table 3.3, can be collected by the software of test station.

Table 3.3 Function of Software

Item	***Function***
Automatic Control System	Controlling the Current, Voltage, Mass Flow Rate, Load
Testing Data	Current vs. Time, Voltage vs. Time, Power vs. Time, Tafel Data, Long-time Performance test

The limiting conditions of test station are listed in the Table 3.4.

Table 3.4 One or More PEMFC Testing Range

Type of electronic load	***PRODIGIT 3315D***
Current	0~15A

Voltage	0~60V
Power	75W Max

Fig. 3.12 shows the diagrams of components for the test station. Mainly, the system includes three parts, mass flow controllers, temperature controllers, and a DC electronic load.

3.4 Thermal Infrared Imaging Camera System

3.4.1 Thermal Imaging Analyzer

Fig. 3.13 shows a thermal infrared imaging camera (SAT-S160), which takes the temperature distribution image on the cathode surface of fuel cell. It is put in front of the cathode surface and the distance between them is 25cm (see Figs. 3.14 and 3.15). The camera is designed for research, development and scientific applications with high resolutions (160 × 120 pixels) and high quality images. It has a thermal sensitivity of 0.08℃ at 30℃, and can record temperatures in the range from -20 to +250℃. The camera has a viewing field, which allows to be imaged from roughly three feet away. The camera has an accuracy of ±2℃, or ±2% of the reading.

Guangzhou SAT has developed a powerful SAT infrared image processing software to be used in conjunction with S160. The operator can not only see the infrared image but also perform spot, line and area analyses, and easily complete the inspection report (including data and charts of the image, line analysis, area analysis, infrared parameters, etc.). In addition, the software has the functions of multi-page and alternate page analyses. The user can put certain analysis results together on the specified pages and change them into word format, so that the report can be more case-specific and visualized.

In the SAT-S160 system, it includes: SAT-S160 Camera, Two Rechargeable lithium cells, Intelligent charger, Video signal output cable, Video connector, USB connector, Infrared lens cap, Lens hood, SAT standard software, and Tripod fixer.

3.4.2 Technical Specification of SAT-S160

Table 3.5 lists the technical specification of SAT-S160. The operating temperature, operating humidity, and storage temperature separately have a wave length range of -20~50℃, ≦90%, and -40~70℃. It is applicable for an IDC, because the temperature range is located in the interval between the recommended minimum and maximum temperatures according to some guideline or standard.

Table 3.5 Technical Indexes of SAT-S160

Environmental Requirements of SAT-S160		
1	Operating temperature	-20℃ ~ 50℃
2	Operating humidity	≤90%
3	Storage temperature	-40℃ ~ 70℃
Technical Indexes of SAT-S160		
4	Type of Detector	Uncooled focal plane
5	Spectral range	7.5 ~ 14um
6	Weight	≤0.7Kg （including battery）
7	NETD	0.1℃
8	Temperature range	-20 ~ 250 ℃
9	Temperature accuracy	±2℃/±2%
10	Battery operating time	App. 2 hours
11	FOV	20° × 15° /10mm
12	Spatial resolution	2.2mrad
13	Pixel	160×120
14	Image display and temperature measurement	Full-screen pseudocolor and full-screen temperature measurement
15	Structure	Integrated design and one-hand operation
16	Frame frequency/ output pattern	50Hz, PAL/NTSC selection
17	Packing	High-strength plastics portable case

3.4.3 Calibration Procedure of SAT-S160

The emissivity factors of thermal infrared imaging camera are different from a variety of materials in the surface, so it is important to find an appropriate emissivity factor of the surface. In order to have more accurate temperature measurement by thermal infrared imaging camera, the setup temperature of the surface in PEMFC should be higher than the ambient one, for example, 50℃. After the setup temperature of 50℃ uniformly spread over the entire surface of MEA, the calibrated thermocouple is put on the surface of PEMFC. We check four points around the calibrated thermocouple to see the

uniformity of temperature on the surface (see Figs. 3.16 and 3.17), and then adjust the emissivity factor in the thermal infrared imaging camera until the measured temperature is agreed with the thermocouple temperature (see Fig. 3.18). The emissivity factor found was 0.95 in this study. MEA surface is a polymer, made of the long chain of carbon, which is irregular arrangement. The microporous structure is formed in the surface that results in thermal radiation reflection. The body repeatedly reflects thermal radiation that is similar to the blackbody radiation. As expected, in the experiment, the emissivity factor of 0.95 does not change in the rest of the study. The other object parameters of thermal imaging analyzer are listed in Table 3.6.

Table 3.6 Object Parameter of Thermal Imaging Analyzer

Emissivity	0.95
Distance	0.25 m
Ambient temperature	23.7 ~ 24.8 ℃
Relative humidity	52.1 ~ 53.7 %

3.5 Hydrogen Flow Meter

We use red-y compact series of the flow meter. It is set on the outlet of fuel cell to measure the corresponding hydrogen flow rate. Then the conversion ratio of fuel can be deduced from these readings. The detailed information of hydrogen flow meter is listed in the Table 3.7, and the meter picture is given in Fig. 3.19.

Table 3.7 Hydrogen Flow Meter Calibration Data

Metering Fluid	Hydrogen
Materials	Aluminum, stainless stell
Max. Flow	150 mln/min
Turndown Ratio	1:50
Operating Temperature	0℃ ~ 50℃
Operating Pressure	Up to 10 bar g
Atm. Pressure	982 mbar a
Accuracy	±1.0% of full scale
Sensor Material	PBT, epoxy
Sealing Material	FKM, optional EPDM or PTFE
Process Connection	Inside thread G1/4", G1/2"

The common used range of inlet flow rate is 40 ~ 60sccm. According to the formula of Reynolds number:

$$Re = \frac{\rho v D}{\mu} \qquad (3\text{-}1)$$

The Reynolds number is ranged between 3.16 ~ 4.74, so the inlet flow rate is laminar flow.

3.6 Digital AC mΩ meter

The test frequency is at 1kHz to measure the resistance. The resistance includes contact and ionic resistance. The detailed information of digital AC mΩ meter is listed in the Table 3.8.

Table 3.8 Information of Digital AC mΩ Meter

Measurement Method		AC 4-terminal measurement method					
Measuring Frequency		1kHz					
Measured impedance	***Range***	30 mΩ	300 mΩ	3Ω	30Ω	300Ω	3kΩ
	Resolution	1μΩ	10μΩ	100μΩ	1mΩ	10mΩ	100mΩ
	Measuring Current	7.4mA	1mA	100μA	10μA	5μA	1.5μA
	Accuracy	± (0.5% read-out value + 8-digits)					
Voltage Measurement Range		DC ± 5.0000V / ± 50.000V					
Analog Output		DC 3V					

3.7 Process of Fuel Cell Testing

In order to evaluate the performance of the PEMFC, the assembled cell is tested under the following process:

1. The inlet of the flow channel on anode is plugged into the reactant supply tubes in the test station.
2. The current collectors are connected to the sensor on the test station to measure the voltage and current, and also connected to the load supply.
3. Adjust the flow rate of the reactant gas to the assigned value to let cell operate to obtain an open circuit voltage.
4. Apply load to let the cell discharge a current through the chemical reaction under an assigned voltage.
5. The current, voltage and power outputs from the cell can be recorded and plotted into the performance (I-V and I-P) curves.

6. Repeat the procedure for another load.

3.8 Uncertainty Analysis

Some form of analysis must be performed on all experimental data. The analysis may be a simple verbal appraisal of the results, or it may take the form of a complex theoretical analysis of the errors involved in the experiment and matching of the data with fundamental physical principles. Therefore, their accuracy should be confirmed before the analyses of experimental results. Experimental measuring must have errors, and experimental errors divide into the fixed (systematic) error and random (non-repeatability) error, respectively. Fixed error is produced after each experiments and it can be removed by proper calibration and correction. However, Random error is different for every apparatus reading datum and hence cannot be removed. The objective of uncertainty analysis is to estimate the probable random error in experimental results.

3.8.1 Analyses of the Propagation of Uncertainty in Calculations

Uncertainty analysis estimates the uncertainty levels in the experiment. A method of estimating uncertainty in experimental results has been presented as follows:

Suppose a set of measurements is made and the uncertainty in each measurement may be expressed with the same odds. These measurements are then used to calculate some desired results of the experiments. The result R is a given function of the independent variables x1, x2, x3… xn. Thus,

$$R = R(x_1, x_2, x_3, \dots, x_n) \qquad (3\text{-}1)$$

An individual xn, which affects error of R, can be estimated by the deviation of a function. A variation, δX_n, in xn would cause R to vary

according to

$$\delta R_n = \frac{\partial R}{\partial x_n}\delta x_n \qquad (3\text{-}2)$$

Normalize above equation by dividing R to obtain

$$\delta \frac{R_n}{R} = \frac{1}{R}\frac{\partial R}{\partial x_n}\delta x_n = \frac{x_n}{R}\frac{\partial R}{\partial x_n}\frac{\delta x_n}{x_n} \qquad (3\text{-}3)$$

Equation (3-3) can be used to estimate the uncertainty interval in the result due to the variation in xn. Substitute the uncertainty interval for xn,

$$u_R = \frac{x_n}{R}\frac{\partial R}{\partial x_n}ux_n \qquad (3\text{-}4)$$

To estimate the uncertainty in R due to the combined effects of uncertainty intervals in all the xi, it can be shown that the best representation for the uncertainty interval of the result is

$$u_r = \pm\left[\left(\frac{x_1}{R}\frac{\partial R}{\partial x_1}u_1\right)^2 + \left(\frac{x_2}{R}\frac{\partial R}{\partial x_2}u_2\right)^2 + \cdots + \left(\frac{x_n}{R}\frac{\partial R}{\partial x_n}u_n\right)^2\right]^{\frac{1}{2}} \qquad (3\text{-}5)$$

3.8.2 The Uncertainty of Test Station Apparatus

The apparatus must to be corrected by other standard instruments to make sure that they can normally operate and let the inaccuracy of the experimental results reduce to the minimum.

3.8.2.1 The Uncertainty of HP 6060B Electronic Load: u_V,u_A

The HP 6060B electronic load in the test station has been corrected its potential and current meter before experiment. The research uses FLUKE 8060A Digital Multimeter and Chroma Smart N300-040 Electronic Load to correct HP load box. Table 3.9 shows the error for different potentials.

Table 3.9 Uncertainty of Electronic Load Potential Meter

Standard value (V)	*Digital meter (V)*	*Uncertainty (%)*
20.00	19.81	-0.95
9.95	9.85	-1.00
8.02	7.95	-0.87
6.04	5.95	-0.99
5.00	4.97	-0.60
3.03	3.00	-0.99
1.00	0.998	-0.50
0.00	0.00	0.00

Next, the DC current meter of HP load box is corrected. They use Chroma Smart electronic load and FLUKE digital meter to find the impedance of the shunt. They connect the shunt between HP load box and DC power source after correcting and adjust different potentials of power source, therefore, it can change the measurement current of load box meter. At the same time, the shunt measures a signal of current. After converting this signal, it can define the actual current of this circuit. Table 3.10 shows the error for different current.

Table 3.10 Uncertainty of Electronic Load Current Meter

Fluke digital meter (mV)	*Electronic load (A)*	*Conversion value* ($\bar{A}$)	*Uncertainty (%)*
0.00	0.00	0.00	0.00
1.69	1.00	1.02	1.96
5.05	3.00	3.04	1.32
8.37	5.00	5.03	0.60
16.71	10.00	10.05	0.50
25.04	15.00	15.06	0.40
33.41	20.00	20.09	0.45
50.21	30.00	30.19	0.63

3.8.2.2 The Uncertainty of Mass Flow Controller

In this study, there have three MFCs in the test station including anode, cathode and oxygen bleeding flow meter. The specified error is shown as follows:

$$\mathrm{ERROR}(\%) = \frac{\mathrm{CALAUATED} - \mathrm{TARGET}}{\mathrm{FULLSCALE}} \times 100\%$$

The ranges of MFC specified accuracy are 1000±5% with anode MFC, 2000±5% with cathode MFC and 500±1% with air bleeding MFC. They use the same company instrument, series 5850 MFC, as the standard correction apparatus to correct these MFCs. The results are listed in the Table 3.11, 3.12, and 3.13, respectively.

Table 3.11 Uncertainty of Anode MFC

Standard value (sccm)	***Brooks MFC read value (sccm)***	***Measure value (sccm)***	***Uncertainty (%)***
1000	1002	1001	-0.10
500	501	499.8	-0.23
250	250.2	249.7	-0.23
0	0	0	0

Table 3.12 Uncertainty of Cathode MFC

Standard value (sccm)	***Brooks MFC read value (sccm)***	***Measure value (sccm)***	***Uncertainty (%)***
2000	1999.8	1999.4	-0.02
1250	1255	1253	-0.15
1000	1000.3	1000.2	-0.01
500	500.2	500	-0.03
0	0	0	0

Table 3.13 Uncertainty of Air Bleeding MFC

Output Voltage	*Brooks MFC read value (sccm)*	*Measure value (sccm)*	*Uncertainty (%)*
5	500	500.34	0.07
3.75	375	374.54	-0.09
2.5	250	250.32	0.06
1.25	125	124.54	-0.09
-0.001	0.0	0	0

They are anode, cathode and air bleeding flow meter, respectively. In these tables, the standard value means the setting flow rate, the Brooks MFC read value means the test station MFC readout value, the measurement value is the actual measured value. Then, these data can define the errors in different flow rates.

3.8.2.3 The Uncertainty of Temperature Controller

There are three temperature controllers in the test station. They are anode, cathode humidifier and fuel cell, respectively. The results of analyses are listed in Table 3.14, 3.15, and 3.16, respectively. In these tables, standard value means the setting temperature and the measure value means actual value, measured by the correction apparatus.

Table 3.14 Uncertainty of Anode Temperature Controller

Standard value (℃)	*Measure value (℃)*	*Uncertainty (%)*
25	25	0
35	35	0
50	50	0
70	70	0
85	84	-1.17
95	94	-1.05

100	99	-1

Table 3.15 Uncertainty of Cathode Temperature Controller

Standard value (℃)	***Measure value (℃)***	***Uncertainty (%)***
25	25	0
35	35	0
50	50	0
70	70	0
85	85	0
95	94	-1.05
100	99	-1

Table 3.16 Uncertainty of Cell Temperature Controller

Standard value (℃)	***Measure value (℃)***	***Uncertainty (%)***
25	25	0
35	35	0
50	50	0
70	70	0
85	85	0
95	95	0
100	100	0

3.8.3 The Uncertainty of Fuel Cell Power Density

The uncertainty of fuel cell power density comes from measuring process of fuel cell apparatus, therefore, the minimum scale of measuring voltage in the apparatus is 1mV, and the minimum scale of measuring current in the apparatus is 0.1mA. Appendix A shows the measuring uncertainty calculating process. Table 3.17 shows the uncertainty power density of PEMFC and micro PEMFC.

Table 3.17 The Measuring Uncertainty of Fuel Cell

PEMFC	The measuring uncertainty	Voltage	±0.10%
		Current	±0.02%
		Power	±0.10%
Micro PEMFC	The measuring uncertainty	Voltage	±0.10%
		Current	±0.01%
		Power	±0.10%

Fig. 3.1 Vacuum Chamber

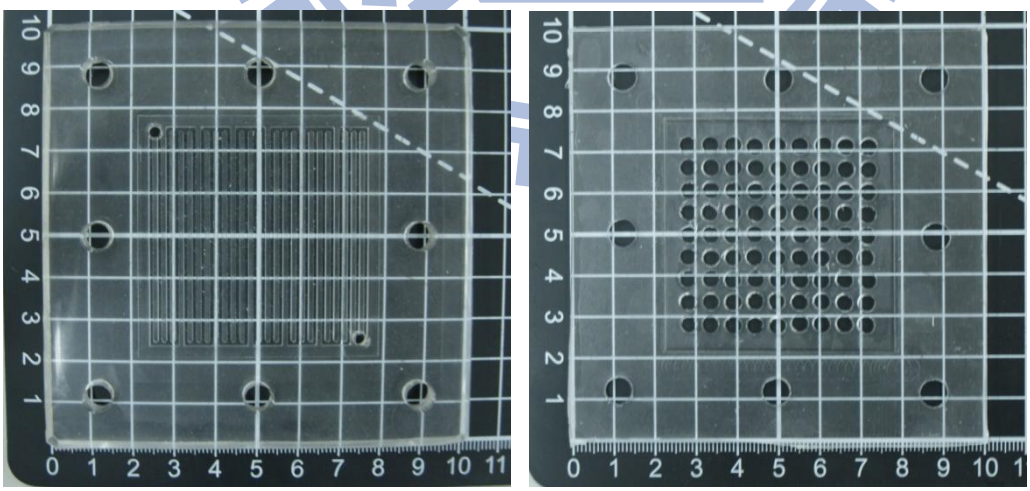

Fig. 3.2 PDMS Flow Field Plates

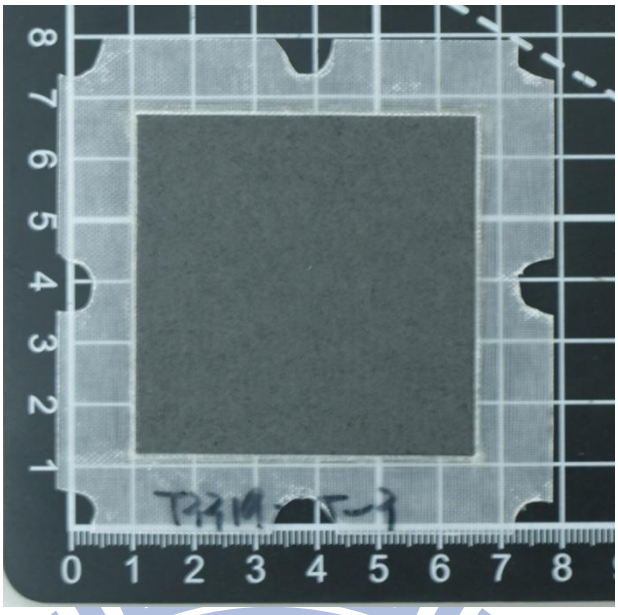

Fig. 3.3 GDL and MEA

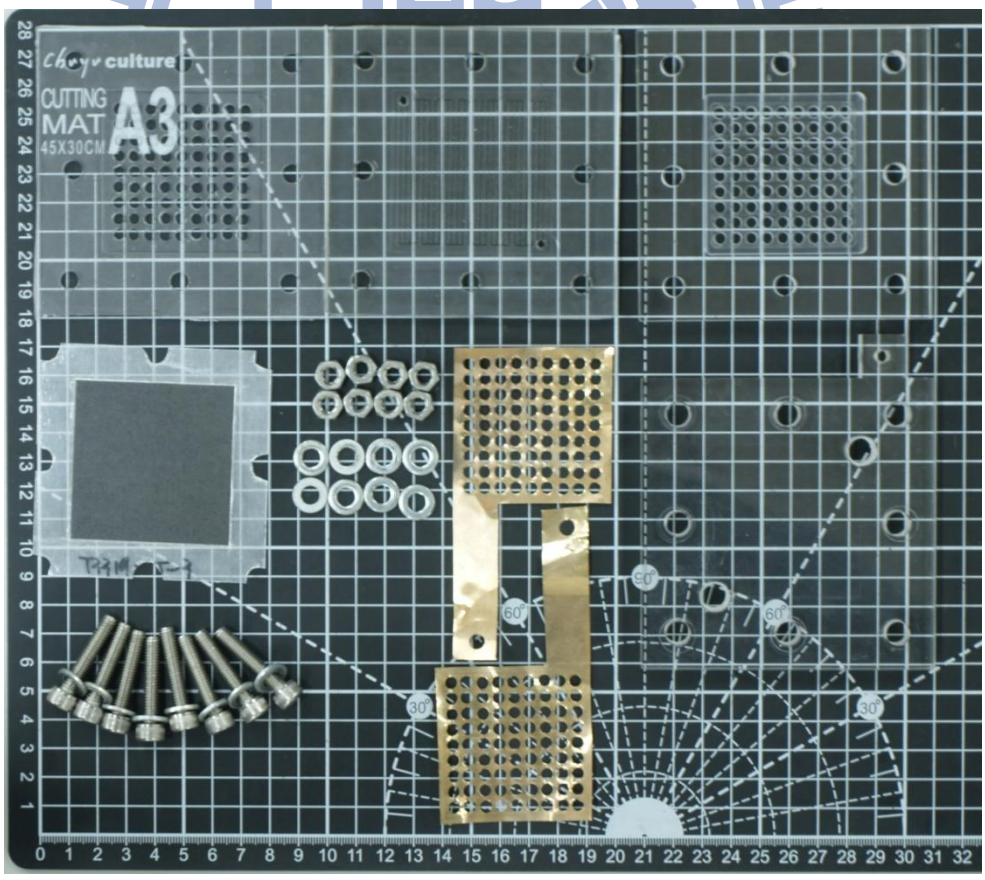

Fig. 3.4 Components of a Single PDMS Fuel Cell

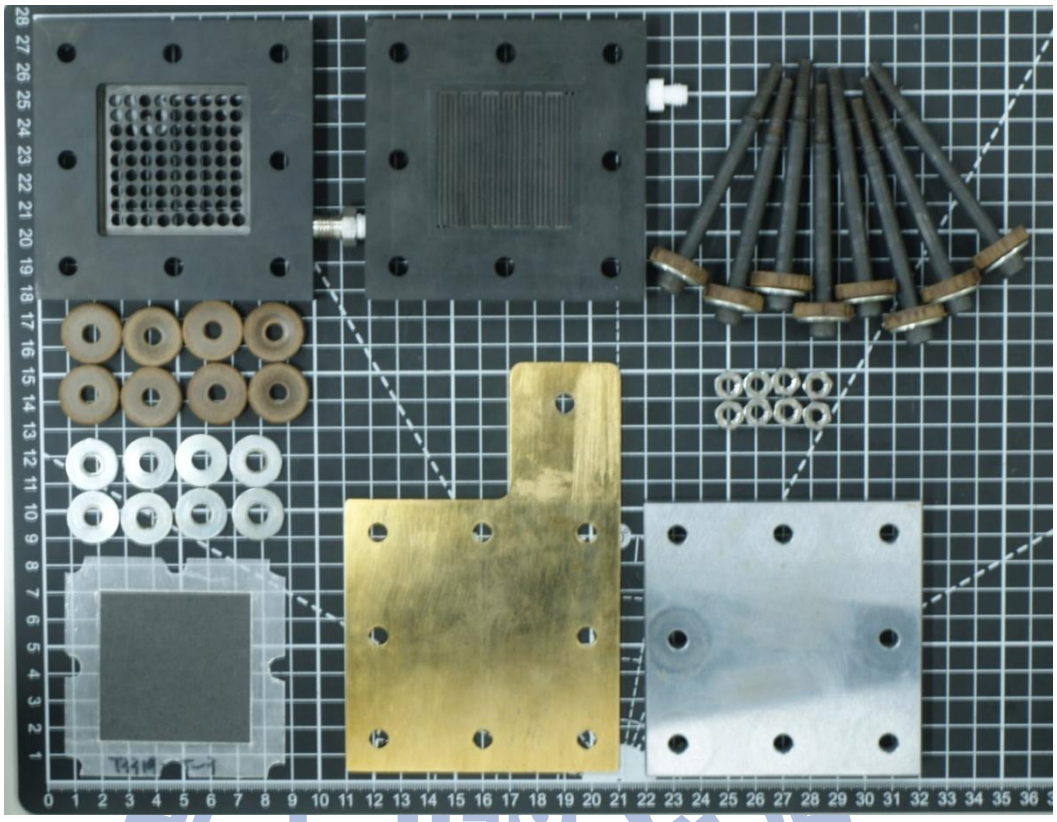

Fig. 3.5 Components of a Single Graphite Fuel Cell

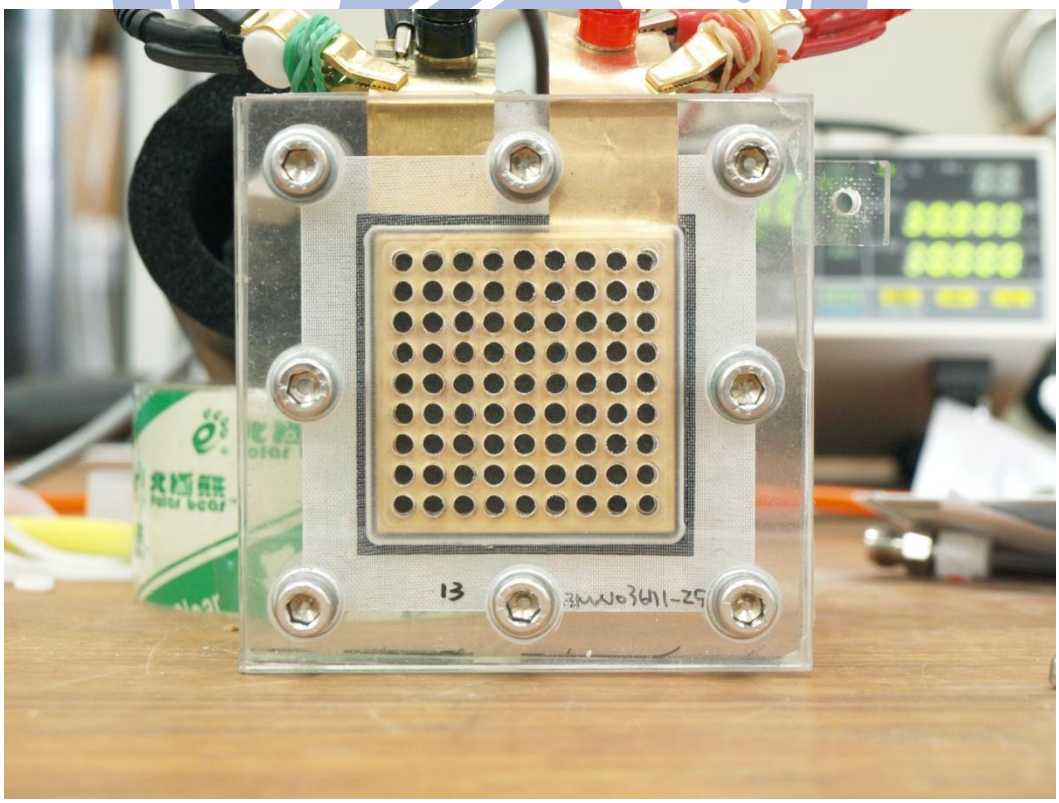

Fig. 3.6 Assembly of PDMS PEMFC

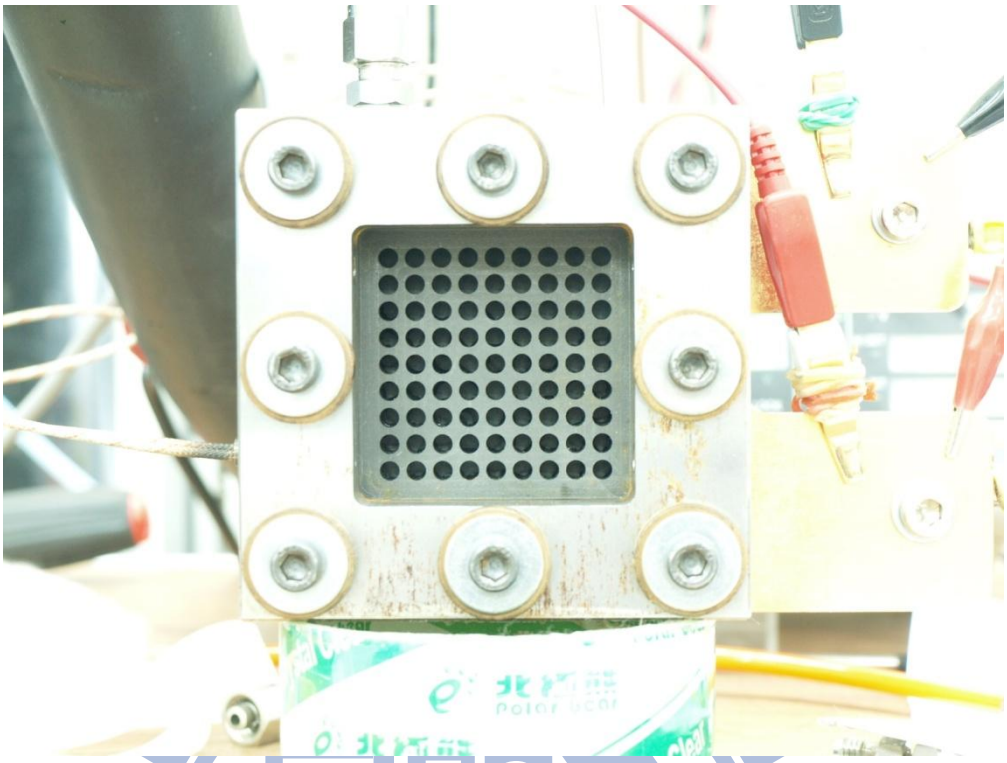

Fig. 3.7 Assembly of Graphite PEMFC

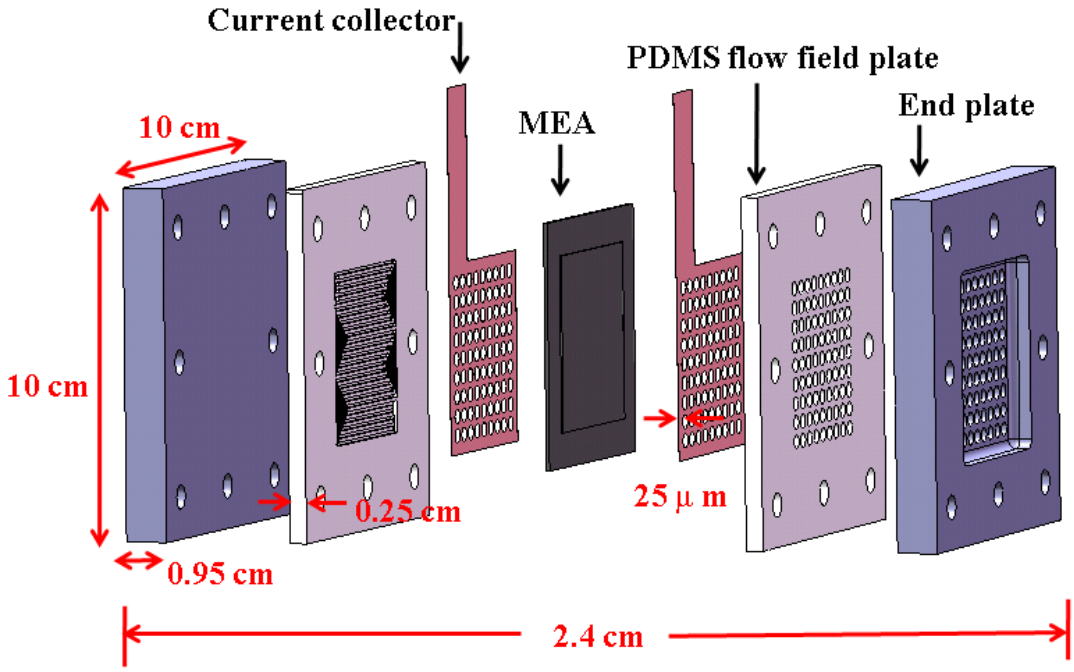

Fig. 3.8 Sandwich Structure of Single PDMS Air-breathing PDMFC

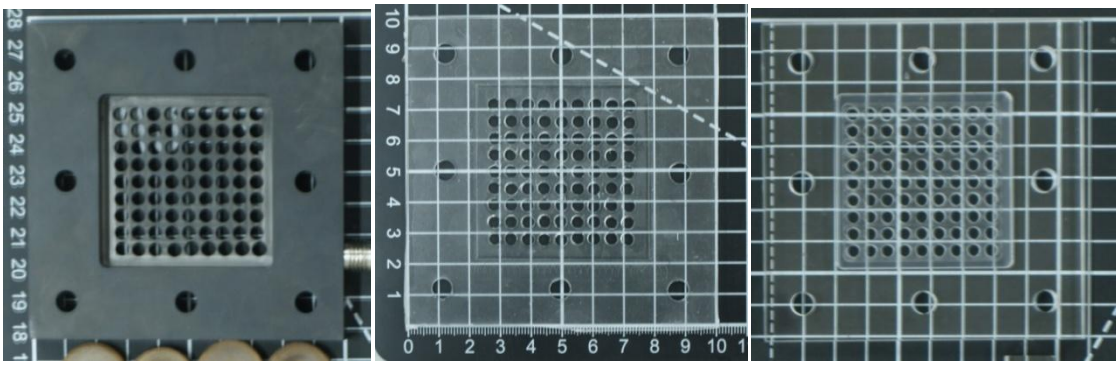

Fig. 3.9 Shape of Acrylic Plate, Graphite Plate and the PDMS

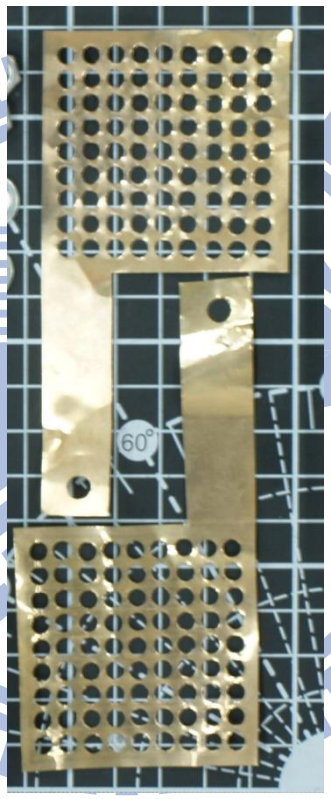

Fig. 3.10 Current Collector Slice

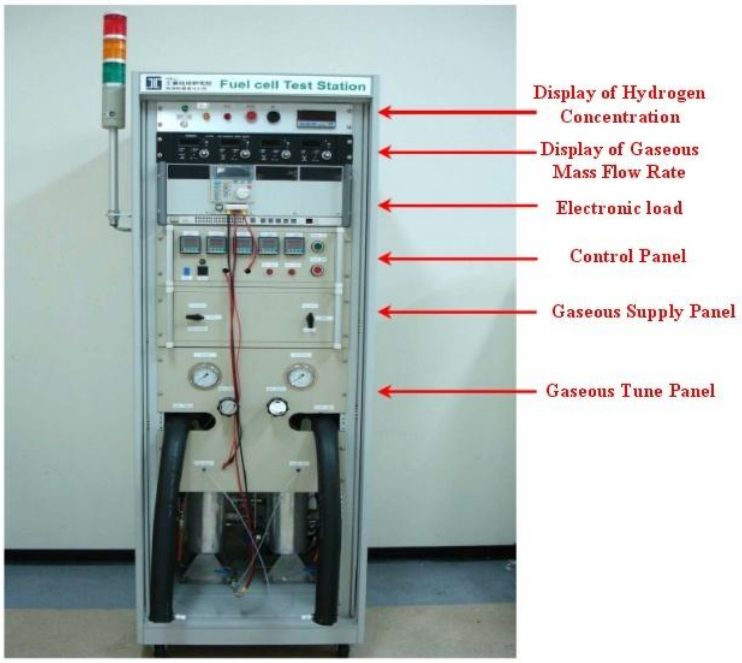

Fig. 3.11 Test Station

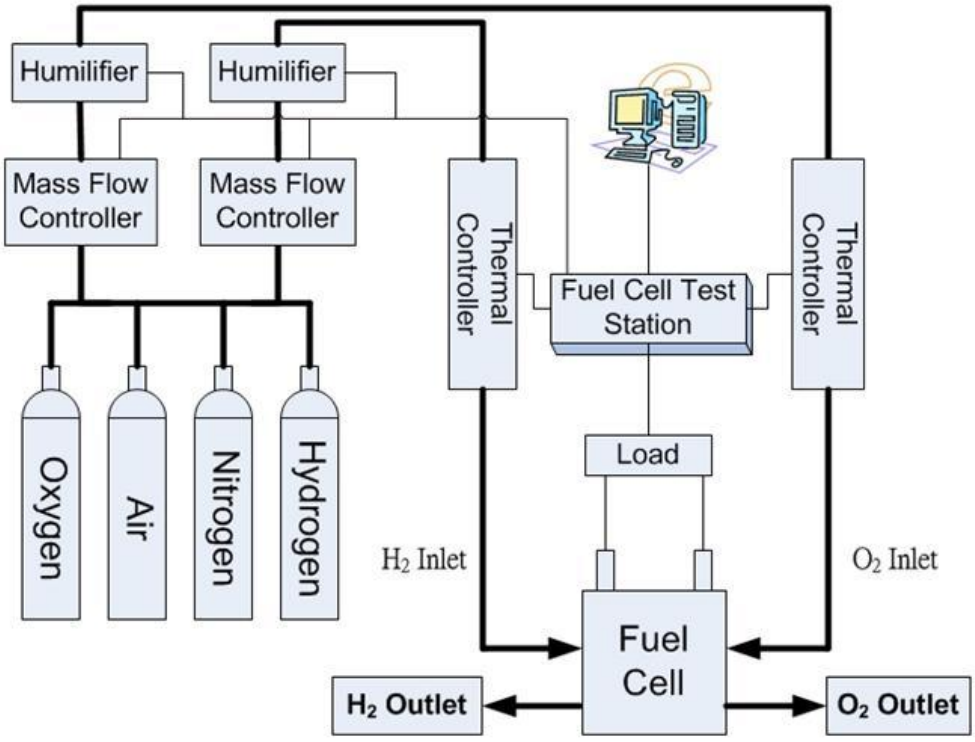

Fig. 3.12 Components of Test Station

Fig. 3.13 Thermal Infrared Imaging Camera

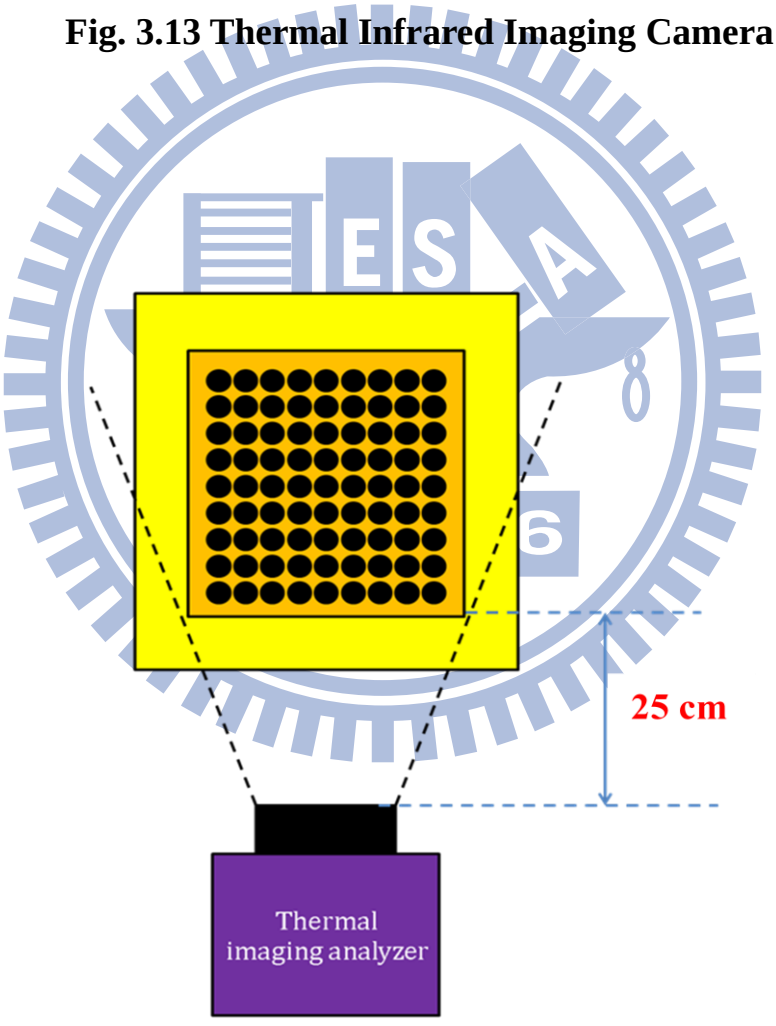

Fig. 3.14 Configuration of Thermal Infrared Imaging Camera and Air-breathing Fuel Cell

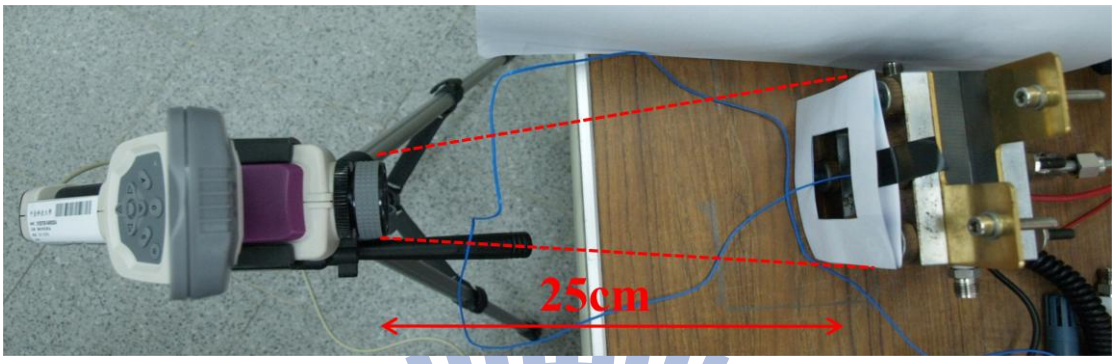

Fig. 3.15 Top View of Thermal Infrared Imaging Camera and Air-breathing Fuel Cell

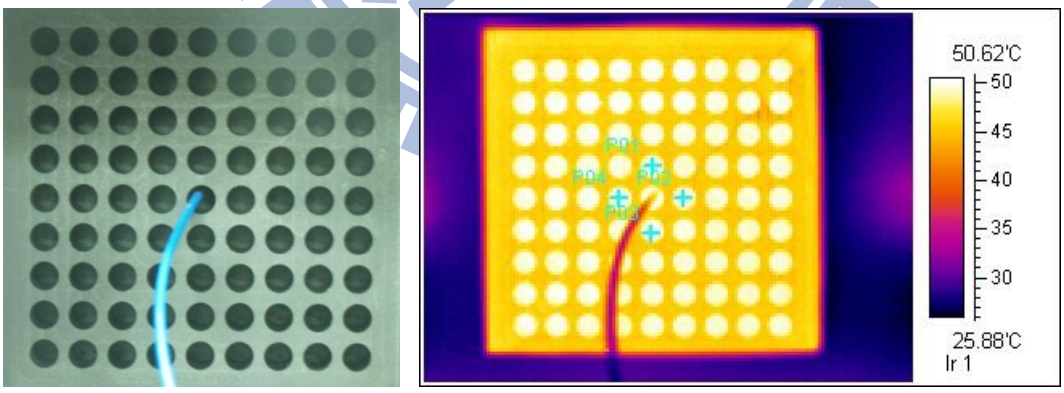

Fig. 3.16 Schematic of Thermocouple and the Surface of PEMFC and Their Thermal Imaging Picture

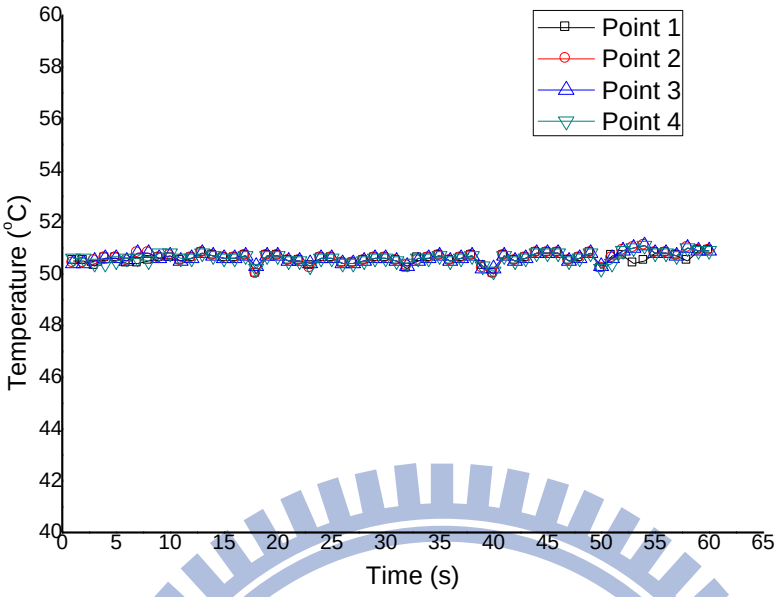

Fig. 3.17

Temperature Difference on the Surface of PEMFC between the Four Points around Thermocouple

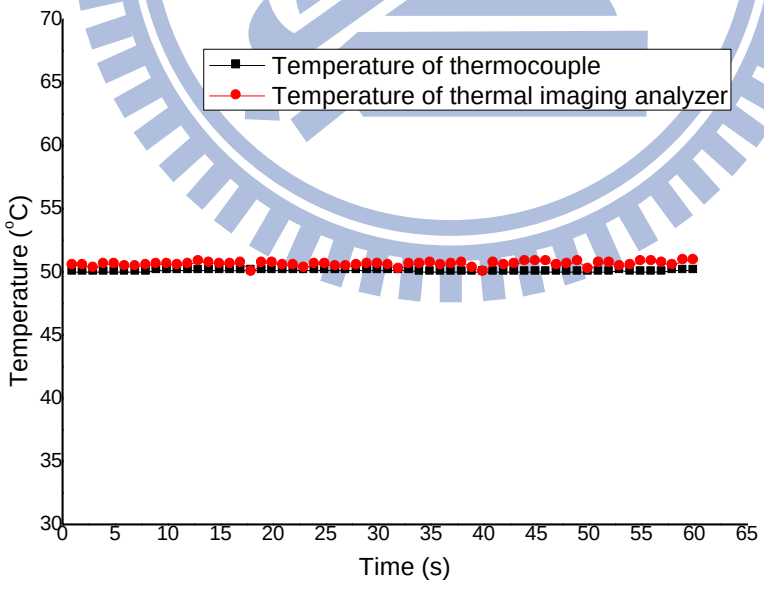

Fig. 3.18 Temperature of Thermocouple and Thermal Imaging Analyzer

Fig. 3.19 Hydrogen Flow Meter

Chapter 4

Results and Discussion

This study is divided into three parts. The research flow chart was shown in Fig. 1.7. Firstly, a series of performance experiments for parameters study on a single PDMS air-breathing PEMFC were carried out and demonstrated in section 4.1. The experimental parameters included flow rate with the corresponding hydrogen utilization and clamping force. Secondly, the similar performance experiments on single graphite air-breathing PEMFC were also carried out and illustrated in section 4.2. The experimental parameters consisted of flow rate, clamping force and cell temperature. For both experimental studies, the corresponding thermal imagines of resultant temperature distributions on the cathode surface were given as well. In addition, in order to justify the durability of continuous usage and water flooding situation, both fuel cells mentioned above were tested for 24 hours at a fixed operating voltage. Finally, section 4.3 made a comparison between PDMS and graphite PEMFC to analyze the performance difference and the advantage.

4.1 The Single PDMS Air-breathing PEMFC

4.1.1 Reference Case

A series of experiments were carried out for PDMS PEMFC. The patterns of anode flow field plates are introduced into my study from ITRI. The serpentine flow field plates have high pressure drop, so the water droplets can be drain easily. A reference case, whose performance is shown in Fig. 4.1, was chosen in advance to serve as the comparison base. The testing conditions

of reference case are listed in Table 4.1. The hydrogen flow rate of 60sccm at the anode was chosen because it had the best performance. According to the formula of Reynolds number:

$$Re = \frac{\rho v D}{\mu} \qquad (4\text{-}1)$$

The Reynolds number is about 4.74, so the inlet flow rate is laminar flow.

The oxygen at the cathode was by supplied air-breathing from the air, and the temperature and humidity were kept in room environment conditions due to the consideration for future application. The advantage of air-breathing is no need for extra driving device to supply air at the cathode, because it can enter cell to the membrane by diffusion through holes. Gas back pressure was kept at 0kPa on anode, implying that it was atmospheric pressure in the outlet of the fuel channel. The open ratios of current collector slices and the cathode flow field plate are defined as the ones of the sum of the open circle area to the total area; see Figs. 3.2, 3.9 and 3.10. In this study, open ratios for both were selected as 40%. Bussayajarn et al. [17] found the circular open design having the best performance, and Kim et al. [21] showed that the circular-hole pattern with opening ratio of 38% has the best performance. The number of circle holes in current collector slices was 81 because the better reactions and more electrons could be achieved. The same number of holes was adopted in cathode flow field plates as well.

Clamping force is the bolt torque applied on the cell, which decides the contact pressure between GDL and current collector, and the deformation of the flow field plate structure. The maximum allowable clamping torque applied was 50Kgf • cm for PDMS PEMFC and 100Kgf • cm for graphite one. Beyond these limits, the PDMS flow field plate and MEA were deformed severely and

the graphite flow field plate was crashed. In this study, 30Kgf・cm was used as reference case, because it could perform best.

Table 4.1 Testing Conditions of Reference case

Reactant gases	
Anode	H_2 (99.9%)
Cathode	Air
Flow Rates	
Anode	H_2: 60 sccm (Forced convection)
Cathode	Air-breathing (Natural convection)
Gas Backpressure (Gauge)	
Anode	0 kPa
Environmental Condition	
Gas temperature	Room Temperature (20 ±2℃)
Humidity	Room Condition (40% ±2%)
Temperature	
Reheat temperature	No reheat
Flow Field Plate	
Anode material	PDMS
Cathode material	PDMS
Cathode Shape	81-circle
Cathode Open Ratio	40%
Current Collector (thickness = 0.05mm)	
Material	Cu/Au
Shape	81-circle
Open Ratio	40%
Clamping Force	
30 Kgf・cm	

The I-V, I-P and I-R curves of reference case are shown in Fig. 4.1. Each point was taken from the average of three measurements, and the maximum error was less than 2.4%.

As mentioned in Sec. 2.2.2, there have three major types of fuel cell losses: activation, Ohmic and concentration losses. Because of those losses, the current density (I) increases with decreasing voltage (V) in I-V curve. We can see from the Figure 4.1 that the open circuit voltage (OCV) of I-V curve is 0.9797V, which is less than the ideal one, 1.23V, due to the activation losses. In the range of 0.75 to 0.9797V, the voltage drops sharply with increasing current because the temperature and humidity of fuel cell do not reach equilibrium yet. As the equilibrium achieves, the voltage drop is slowed down with increasing current. Between 0.45 and 0.75V, the voltage drop is mainly influenced by the Ohmic losses which are not only affected by clamping force, but also by the humidity of membrane and the hydrogen utilization. At the end of I-V curve, however, the voltage drops sharply again with increasing current due to the shortage of the fuel supply.

In this study, the maximum power density is 136.144mW/cm^2 and the corresponding current density is 248.288mA/cm^2 at the voltage of 0.5483V. I-P curve increases from zero to the maximum, then, it drops rapidly due to a shortage of fuel supply as mentioned previously. The best operation voltage range is found from 0.5 to 0.7V, because the cell's performance is stable in such a range.

The I-R curve is measured by a digital AC mΩ meter, which can detect the impedance during the ion transportation in the electrolyte and the resistance caused by the contact of electrode at a fixed high frequency of 1kHz. Both the contact of electrode and the ion conduction in the electrolyte contribute to the resistance. At low current density, the water produced during electrical chemical reaction is not enough to make the membrane reaching the saturated state, so the resistance becomes higher and more unstable. At high current

density, however, the membrane has enough water content to reach the saturated state, so the resistance gradually becomes lower and more stable. The limiting resistance value of I-R curve is 14.6 mOhm • cm^2 with a corresponding voltage of 0.1873V.

The resistance measured by the digital AC mΩ meter is different from the ratio of voltage to current (V/I, where V is the discharge voltage and I is the current), representing the total resistance of whole loop in the cell. Both are shown in Fig. 4.2 for comparison. It can be seen that the value obtained by V/I calculation is much greater than the one measured by AC mΩ meter. However, the difference gradually becomes smaller as the current increases, and they are almost coincident at the limiting current density, indicating that the impedance during the ion transporting in the electrolyte and the resistance caused by the contact of the electrode play the important roles.

The following parametric studies are focusing on the effects of flow rate and clamping force on the performance of single PDMS air-breathing PEMFC.

4.1.2 Effect of Flow Rate

The resultant I-P and I-V curves, hydrogen utilization and temperature distribution images are discussed under different flow rates of hydrogen.

4.1.2.1 I-P and I-V Curves

As shown in Figs. 4.3 and 4.4, it can be seen that the performance is improving with an increase of flow rate because the lower flow rate of 40 ~ 50sccm leads to a concentration loss; and the higher flow rate of 60 ~ 80sccm has enough amount to enhance the electrochemical reaction. However, the performance has no further obvious improvement when the flow rate is greater than 60sccm. Apparently, the best performance occurs at 60sccm.

4.1.2.2 Hydrogen Utilization

Theoretically, 6.965 sccm of hydrogen flow rate in fuel cell can produce 1 ampere (A) of output current. The mathematical derivation is as follow:

$$\dot{m} = (1\ \mathrm{A}) \times \left(\frac{1\ \mathrm{mol\ e^-}}{96487\ \mathrm{C}}\right) \times \left(\frac{1\ \mathrm{mol\ H_2}}{2\ \mathrm{mol\ e^-}}\right) \times \left(\frac{60\ \mathrm{s}}{1\ \mathrm{min}}\right)$$

$$= 3.109 \times 10^{-4}\ \frac{\mathrm{mol}}{\mathrm{min}}$$

$$= 3.109 \times 10^{-4}\ \frac{\mathrm{mol}}{\mathrm{min}} \times \frac{22.4}{1}\ \frac{\mathrm{L}}{\mathrm{mol}}$$

$$= 0.006965\ \frac{\mathrm{L}}{\mathrm{min}}$$

$$= 6.965\mathrm{sccm}$$

The values of current output were measured by test station and then they were translated into the hydrogen utilization, in the meantime, the experimental hydrogen utilizations were also measured by flow meter for comparison. Table 4.2 gives resultant currents under the different flow rates, ranged from 10 to 100sccm, at 0.2V. The measured and calculated values of hydrogen utilization are given as well.

Table 4.2 Hydrogen Utilization (At 0.2V)

Inlet flow rate (sccm)	***Outlet flow rate (sccm)***	***Measured utilization (sccm)***	***Current (A)***	***Calculated utilization (sccm)***	***Error (%)***	***Ratio of hydrogen utilized (%)***
9.9	0.0	9.9	1.4561	10.14	2.37%	100%
20.2	0.0	20.2	2.941	20.48	1.37%	100%
30.0	0.0	30.0	4.34	30.23	0.76%	100%
40.1	0.0	40.1	5.756	40.09	0.02%	100%
50.0	0.0	50.0	7.103	49.47	1.07%	100%
54.8	0.0	54.8	7.949	55.36	1.01%	100%
60.3	0.0	60.3	8.471	59	2.20%	100%

64.6	4.5	60.1	8.478	59.05	1.78%	93.0%
70.4	10.5	59.9	8.481	59.07	1.41%	85.1%
80.3	20.5	59.8	8.487	59.11	1.17%	74.5%
91.0	31.0	60.0	8.443	58.81	2.02%	65.9%
100.0	39.5	60.5	8.483	59.08	2.40%	60.5%

At the beginning, the flow meter was directly connected to the outlet of fuel cell, and the measured hydrogen utilizations were lower than the calculated ones as shown in Fig 4.5. It is because the outlet of fuel cell contained not only hydrogen gas but also water vapor. The water vapor mixes with hydrogen at the outlet causes a higher outlet flow rate and consequently makes the difference between inlet and outlet flow rates becoming smaller than the calculated ones. Therefore, the measured hydrogen utilizations are lower than the calculated ones. In order to solve this problem, a drying agent was connected in series ahead of the mass flow meter. The ingredient of a drying agent was CaO, used for absorbing water vapor, and the chemical reaction was as following:

$$CaO+H_2O \rightarrow Ca(OH)_2$$

After water vapor was eliminated, the measured hydrogen utilizations and the calculated ones were almost the same as shown in Fig 4.6 and Table 4.2; now, the maximum error is no more than 2.4%. The results indicate that produced current is related to the hydrogen utilization. As shown in Table 4.2, the higher hydrogen utilization, the higher current generated. The ratio of hydrogen utilized in lower flow rates of 10 ~ 60sccm are 100%, whereas it is 93.0% when the flow rate is 65sccm. It implies that the hydrogen supply is not enough when the flow rates are between 10 ~ 50sccm (referring to Figs.4.3 and 4.4). When the flow rate is above 60sccm (such as 70sccm ~ 100sccm), the ratio of hydrogen utilized is decreased because the maximum hydrogen utilization is

around 60sccm.

4.1.2.3 Thermal Images of Temperature Distributions

Matian et al. [28] used a thermal camera to study the temperature variation on each surface of the stack. In this study, thermal imaging analyzer was used to find out temperature distribution in GDL in steady state, which was taken one hour to reach. The pictures of inlet and outlet of fuel cell were illustrated in Fig. 4.7. The chemical reactions in fuel cell result in higher temperature on GDL surface, in other words, the temperature distribution demonstrate chemical reactions situation. As shown in Figs. 4.8 and 4.9, chemical reaction mainly occurs in the neighborhood of inlet, indicating that the flow rate of 10sccm is not enough to fulfill entire reaction on the cell. The corresponding maximum temperature is about 53.3℃. The flow rates from 20 to 40sccm are also not enough for fully fuel cell reaction either, so part of the fuel cell temperatures does not rise as shown in Figs. 4.10 ~ 4.15. The maximum temperature is about 72.94℃ in 20sccm, 86.37℃ in 30sccm and 92.15℃ in 40sccm. When the flow rate increases to 50sccm and 60sccm, the higher temperatures spread to the entire surface of GDL and the isotherm profiles are similar to the concentric circles as seen in Figs. 4.16 ~ 4.19. The maximum temperature is about 94.43℃ in 50sccm and 96.25℃ in 60sccm. According to the results of Sec. 4.1.2.2, the flow rate of 50sccm is still somewhat not enough for entire cell reaction, whereas 60sccm can fulfill entire cell reaction. As a consequence, the temperature distribution in 60sccm is more uniform and the temperature difference is less comparing to those in 50sccm. As expected, the temperature increases with an increase of flow rate

because the higher flow rate can let the chemical reaction more complete.

From above discussion, it can conclude that the flow rate of 60sccm is the optimal choice for the present single PDMS air-breathing PEMFC, because it can provide the best performance with complete hydrogen utilization and uniform temperature distribution.

4.1.3 Effect of Clamping Force

In this part, the clamping force effect on the performance of a single PDMS air-breathing PEMFC is discussed. The torque on each bolt on the cell (8 bolts total) was increasing from 10.0 to 50.0Kgf· cm. The results are shown in Figs. 4.20 (I-P curves), 4.21 (I-V curves) and 4.22 (I-R curves). It can be seen that the performance of the fuel cell has a significant improvement when the clamping torque of each bolt is raised from 10.0 to 30.0Kgf· cm. From 30.0 to 40.0Kgf·cm, it has no further obvious improvement, and starts to decrease from 40.0 to 50.0Kgf·cm.

From the I-R curves shown in Fig. 4.22, however, the fuel cell resistance decreases as the clamping torques rise from 10.0 to 30.0Kgf·cm, and has no further apparent reduction from 30.0 to 50.0Kgf·cm. The trend is similar to the finding of Chang et al. [24].

Basically, the cell's performance can be improved by the enhanced clamping torque because of the reduction in the electrical contact resistance between the current collectors and the GDL. However, as the applied clamping force is getting higher, the porosity of the GDL and the size of the fuel flow channel will be squeezed simultaneously, causing the poorer fuel transportation. Consequently, the resistance has no further obvious reduction and the performance will not be improved. Therefore, an appropriate clamping torque

should be considered carefully to enhance the performance without damaging the GDL and narrowing the fuel flow channels. In the present study, a torque of 30Kgf·cm is recommended.

4.1.4 Durability and Stability Test (24 hours)

4.1.4.1 Power Density-Time Curves (P-t curves)

To investigate whether the single PDMS air-breathing PEMFC performance is still able to be stable after the long-time usage, a series of durability tests were carried out for 24 hours continuously under the condition of a flow rate of 60sccm, a clamping force of 30kg and the room temperature at different fixed operating voltages, such as 0.7V, 0.6V and 0.5V, respectively. Fig. 4.23, which is presented by power density as a function of time, shows the results at three different operating voltages. During the first three hours, the three performance curves appear to have a little instability because the temperature, humidity and water management of PDMS PEMFC do not reach balance conditions yet. The system becomes stable eventually after that duration. Afterward, the performance difference at fixed operating voltage 0.5V is less than 1.05%, the one at 0.6V is less than 0.95% and the one at 0.7V is less than 7.86%. These show that the single PDMS air-breathing PDMFC can maintain a stable power output for a long time use up to 24 hours.

4.1.4.2 Water Accumulation

A fuel cell operates with hydrogen at cathode and oxygen at anode, the water is produced by the electrochemical reaction ($O_2 + 4H^+ + 4e^- \rightarrow 2H_2O$). The concentration gradient drives water to crossover through the membrane from cathode to anode, called as back diffusion. In the meantime, the protons transport across the membrane from anode and cathode with water molecules,

the process is called as electro-osmotic drag. Back diffusion and electro-osmotic drag balance the water in the MEA; therefore, it causes water flooding at the cathode when the effect of electro-osmotic drag is greater than that of back diffusion.

In order to observe the accumulating water conditions, we took pictures at the cathode side every 6 hours in 24 hours, at 0.5V, 0.6V and 0.7V. They are shown in Figs. 4.24 ~ 26, respectively. The corresponding thermal imaging pictures at steady state are given Figs. 4.27 ~ 29. The temperature at 0.5V (above 60℃) is higher than those at 0.6V and 0.7V (both below 60℃), because the lower voltage output causes higher current density, resulting in higher temperature. There is a little amount of accumulated water to appear at 0.6V and 0.7V because the temperature is below 60℃; in contrast, no liquid water appears at 0.5V because the temperature is above 60℃. It indicates that water evaporates to the environment at a higher temperature of a fuel cell (above 60℃). The results also show that the single PDMS air-breathing PDMFC has less water flooding problem, since non-thermal conductor of the PDMS material can maintain a higher temperature for operation.

4.2 The Single Graphite Air-breathing PEMFC

4.2.1 Effect of Flow Rate

The resultant I-P and I-V curves and temperature distribution images are discussed under different flow rates of hydrogen.

4.2.1.1 I-P and I-V Curves

As shown in Figs. 4.30 and 4.31, it can be seen that the performance is

improving with an increase of flow rate because the lower flow rate of 30sccm leads to a concentration loss; and the higher flow rate of 40 ~ 80sccm has enough concentration to enhance the electrochemical reaction. However, the performance has no further obvious improvement when the flow rate is greater than 40sccm. Apparently, the best performance occurs at 40sccm. According to Sec. 4.1.2.2, the theoretical hydrogen utilization is about 40sccm, obtained by calculation using current output.

4.2.1.2 Thermal Images of Temperature Distributions

As shown in Figs. 4.32 and 4.33, chemical reaction mainly occurs in the neighborhood of inlet, indicating that the flow rate of 10sccm is not enough to fulfill entire reaction on the cell. The corresponding maximum temperature is about 28.01℃. The flow rates from 20sccm to 30sccm are also not enough for fully fuel cell reaction either, so the part of fuel cell temperatures does not rise apparently as shown in Figs. 4.34 ~ 4.37. The maximum temperature is about 31.48℃ in 20sccm and 34.4℃ in 30sccm. When the flow rate is above 40sccm, the higher temperatures spread to the entire surface of GDL as seen in Figs. 4.38 ~ 4.43. The maximum temperature is about 36.66℃ in 40sccm, 36.41℃ in 50sccm and 36.33℃ in 60sccm. The results showed that the temperature distribution is uniform and the GDL temperature is below 60℃ in graphite PEMFC. And the temperature rise is not so obvious with increasing flow rate, because the graphite is a thermal conductor that can dissipate heat effectively.

4.2.2 Effect of Clamping Force

In this part, the clamping force effect on the performance of a single graphite air-breathing PEMFC is discussed. The torque on each bolt (8 bolts total) was increased from 10.0 to 100.0Kgf· cm. The results are shown in Figs. 4.44 (I-P curves), 4.45 (I-V curves) and 4.46 (I-R curves), respectively. It can be seen that the performance of the fuel cell has a significant improvement when the clamping torque of each bolt is raised from 10.0 to 100.0Kgf·cm.

From the I-R curves are shown in Fig. 4.46, however, the fuel cell resistance decreases as the clamping torques rise from 10.0 to 100.0Kgf·cm. The cell's performance can be improved by the enhanced clamping torque because of the reduction in the electrical contact resistance between the current collectors and the GDL. Furthermore, the graphite fuel flow channels are hard enough to resist the squeezing force, unlike the PDMS one. Therefore, a higher clamping torque can be chosen to enhance the performance without damaging the graphite flow plates. In the present study, a torque of 100Kgf·cm is recommended.

4.2.3 Effect of Cell Temperature

Cell temperature was expected to affect the performance of graphite air-breathing PEMFC. The temperature was increased from room temperature (22℃~24℃) to 80℃. As shown in Figs. 4.47 (I-P curves) and 4.48 (I-V curves), it can be seen that the performance of the graphite PEMFC has a significant improvement when the cell temperature is raised from room temperature (22℃~24℃) to 60℃, and starts to decrease from 60℃ to 80℃. With an increasing temperature (below 60℃), it not only accelerates water

evaporation at the cathode but also increases the reaction kinetics, resulting in high performance. However, when the temperature increases above 60℃, it reduces water content of MEA that declines both oxygen reaction and hydrogen reaction, leading to a negative impact on performance.

From the I-R curves in Fig. 4.49, the graphite fuel cell resistance has no obvious difference from room temperature (22℃~24℃) to 60℃, but increases dramatically as the cell temperature rising from 60℃ to 80℃. Because less water is contained in MEA due to evaporation and less water back diffused from cathode to anode, resulting in the low activity of protons and high resistance, as the cell temperature exceeds 60℃. At 70℃ and 80℃, the resistance decreases sharply at low current density regime (below 100 mA/cm^2), and then decreases slowly at high current density one (above 100 mA/cm^2). It is because at 70℃ and 80℃ cell temperatures, not enough water can be produced but evaporation is intensified at low current density regime, whereas it can generate enough water for water balance at high current density (above 100 mA/cm^2). There is a trade-off between water production and water evaporation in MEA.

In the present study, the appropriate cell temperature is 60℃. The trend is similar to the results of Zhang et al. [29], which the appropriate cell temperature is 60℃ also.

4.2.4 Durability and Stability Test (24 hours)

4.2.4.1 Power-Time Density Curves (P-t curves)

Just like PDMS air-breathing PEMFC, to investigate whether the single

graphite air-breathing PEMFC performance is able to be stable after the long-time usage, a series of durability tests were carried out for 24 hours continuously under the conditions of a flow rate of 60sccm, a clamping force of 30kg and the room temperature at different fixed operating voltages, such as 0.7V, 0.6V and 0.5V, respectively. Fig. 4.50, which is presented by power density as a function of time, shows the results at three different operating voltages. The performance difference at fixed operating voltage 0.5V is 38.82%, the one at 0.6V is 28.22% and the one at 0.7V is 12.14% after 24 hours. The three performance curves appear to unstable in 24 hours because the water management does not reach balance conditions and the holes of graphite fuel cell are blocked by liquid water. The reason causing water flooding is that the graphite material is a good thermal conductor, which leads heat dissipation to environment and keeps the cell at lower temperature (below 60℃).

In order to improve water flooding situation, we increased clamping force from 30 Kgf·cm to 100Kgf·cm and also increased cell temperature from room temperature to 60℃ at the potential of 0.5V to test the durability for 24 hours. As shown in Fig. 4.57, the performance difference at 30Kgf·cm and room temperature is 38.82%, the one at 100Kgf·cm and room temperature is 27.28%, and the one at 100Kgf·cm and 60℃ is less than 1.46%. The results showed that the curve at 100Kgf·cm and room temperature drops dramatically, because it has higher power output that produces more liquid water. The one at 100Kgf·cm and 60℃ has better stability comparing with the other two conditions due to the less accumulated water.

4.2.4.2 Water Accumulation

In order to observe the water accumulation, we took pictures of fuel cell on the cathode side every 6 hours in 24-hour duration, at 0.5V, 0.6V and 0.7V. These photos are shown in Figs. 4.51 ~ 4.53, respectively. The corresponding thermal imaging pictures after steady state are given in Figs. 4.54 ~ 4.56. Those show that the stable temperatures at 0.5V, 0.6V and 0.7V are all below 60℃. However, there is a lot of water accumulated at these three voltages because the temperature is so low that it cannot evaporate water below 60℃. The results show that the single graphite air-breathing PDMFC has seriously water flooding problems that it cannot maintain a stable power output for 24 hours.

For the purpose of improving water flooding problems, we increased clamping force from 30Kgf·cm to 100Kgf·cm and then increased cell temperature from room temperature to 60℃ at the potential of 0.5V to observe the consequence. As shown in Fig. 4.58 ~ 4.60, the water flooding situations do not improve obviously with an increase of clamping force; however, the accumulated water can be removed effectively with an increase of temperature.

4.3 Comparison between Graphite and PDMS Air-breathing PEMFCs

4.3.1 Flow Rate

We compared the performance (I-P curves) between the graphite-based flow field plate and the PDMS-based one under the same experimental parameters, given in Sec.4.1.1. The comparison results of Fig. 4.61 showed

that the PDMS PEMFC has better performance than that of graphite one, and the difference is about 38.02%. The graphite PEMFC has a greater thermal conductivity and lower cell temperature (below 60℃; see Figs. 4.54 ~ 4.56) in operation, so the generated water droplets can be easily condensed on the cathode (see Figs. 4.51 ~ 4.53), leading to a lower hydrogen utilization of 40sccm with a poorer performance. Matian et al. [28] showed that about 50~60% of the heat generated in graphite fuel cell is dissipated by natural convection. On the contrast, the PDMS PEMFC has lower thermal conductivity and higher temperature (above 60℃) because the materials can prevent heat loss (Figs. 4.27 ~ 4.29), so no water droplets are condensed to block the air-breathing holes (see Figs. 4.24 ~ 4.26) and leads to a more complete hydrogen utilization with a greater performance.

4.3.2 Clamping Force

Now, we compared the performance under the same resistance. In order to obtain the same resistance for both PEMFCs, we increased the clamping force of graphite PEMFC up to 100 Kgf · cm such that its resultant resistance measured by a digital AC mΩ meter was the same as that PDMS PEMFC in condition of reference case (Table 4.1), where the clamping force was 30 Kgf · cm. The test conditions of the graphite one were listed in Table 4.3. The only difference between Table 4.1 and 4.3 is the clamping force.

Table 4.3 Testing Conditions of the Graphite PEMFC

Reactant gases	
Anode	H_2 (99.9%)
Cathode	Air

Flow Rates	
Anode	H_2: 60 sccm (Forced convection)
Cathode	Air-breathing (Natural convection)
Gas Backpressure (Gauge)	
Anode	0 kPa
Environmental Condition	
Gas temperature	Room Temperature (20 ±2℃)
Humidity	Room Condition (40% ±2%)
Temperature	
Reheat temperature	No reheat
Flow Field Plate	
Anode material	Graphite
Cathode material	Graphite
Cathode Shape	81-circle
Cathode Open Ratio	40%
Current Collector (thickness = 0.05mm)	
Material	Cu/Au
Shape	81-circle
Open Ratio	40%
Clamping Force	
100 Kgf · cm	

Figure 4.62 showed that the PDMS PEMFC has better performance than that of graphite one under the same resistance, and the performance difference is about 28.91%. The results showed that an increase in clamping force has no obvious effect on water management (see Figs. 4.59), so the performance of graphite PEMFC is lower than that of PDMS one.

4.3.3 Cell Temperature

We increased graphite PEMFC temperature to 60℃ by heating rod, then it has the similar performance as that of PDMS one under the reference case, Table 4.1. The test conditions of the graphite PEMFC were listed in Table 4.4.

Table 4.4 Testing Conditions of the Graphite PEMFC

Reactant gases	
Anode	H_2 (99.9%)
Cathode	Air
Flow Rates	
Anode	H_2: 60 sccm (Forced convection)
Cathode	Air-breathing (Natural convection)
Gas Backpressure (Gauge)	
Anode	0 kPa
Environmental Condition	
Gas temperature	Room Temperature (20 ±2℃)
Humidity	Room Condition (40% ±2%)
Temperature	
Reheat temperature	60℃
Flow Field Plate	
Anode material	Graphite
Cathode material	Graphite
Cathode Shape	81-circle
Cathode Open Ratio	40%
Current Collector (thickness = 0.05mm)	
Material	Cu/Au
Shape	81-circle
Open Ratio	40%
Clamping Force	
100 Kgf · cm	

Figure 4.63 showed that the PDMS and graphite PEMFC have similar performance, and the difference is about 1.1%. It indicated that an increase in cell temperature can remove accumulated water (see in Figs. 4.60), so the performance of graphite PEMFC improves rapidly.

In conclusions, the increases of flow rate and clamping force have no obvious effect on performance improvement because the water flooding problems in graphite PEMFC still exist. However, an increase in cell

temperature has obvious effect on a better performance due to the effective removal of water. The results are as same as those found by Ous and Arcoumanis [30]. Except increasing cell temperature like Ous and Arcoumanis's study [30], we also used PDMS material to fabricate flow field plates in PEMFC to resolve the water accumulation problem.

4.4 Dimensional Analyses

In order to compare with other researches, we list variables that involved in the experiment:

$$P = f(A, Q, \tilde{p})$$

Where P is power density, A is active area, Q is flow rate and $\tilde{p}$ is clamping pressure. Then we apply the pi theorem to determine the pi terms which is:

$$\pi = \frac{P A}{Q \tilde{p}}$$

The higher number of π means that it requires less flow rate and clamping pressure to reach the same power density. Besides, the power output increases with an increasing of active area of PEMFC.

Figure 4.64 showed that the PDMS PEMFC has higher number of π than that of the graphite one and Hsu's study of micro PDMS one [3] under the same clamping pressure. For instance, under the same clamping pressure of 65.5N/cm^2, the number of π of PDMS PEMFC is 0.774 which is larger than that of graphite one and Hsu's [3] which is 0.437 and 0.484, respectively.

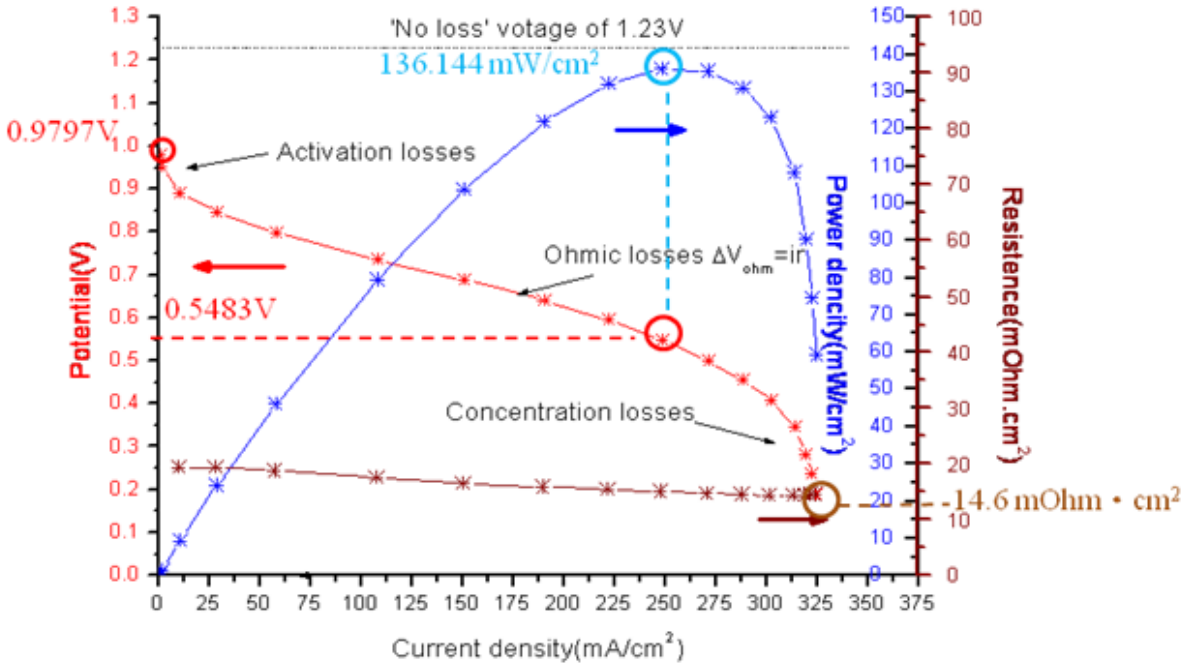

Fig. 4.1 Reference Case

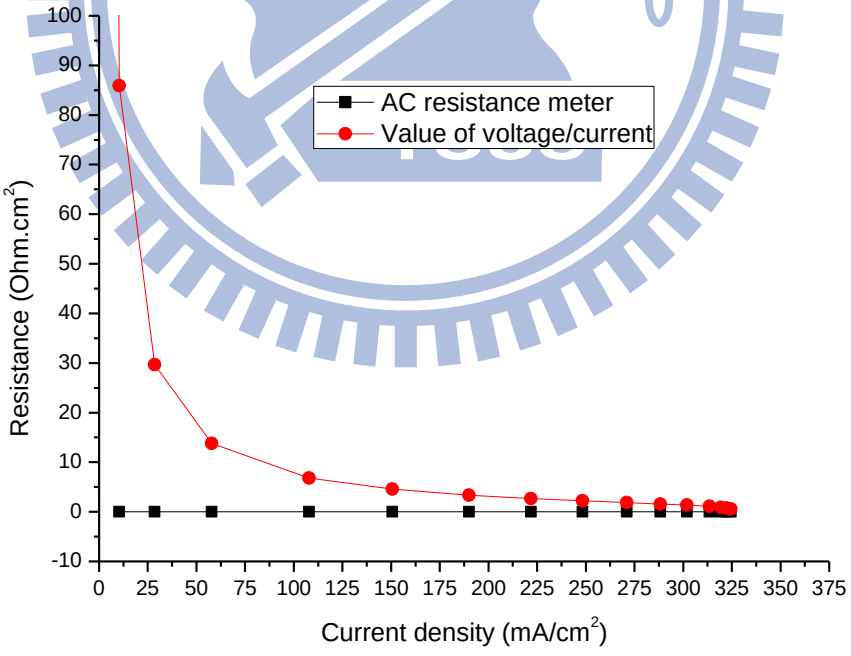

Fig. 4.2 Value of AC Meter and Voltage/Current for Comparison

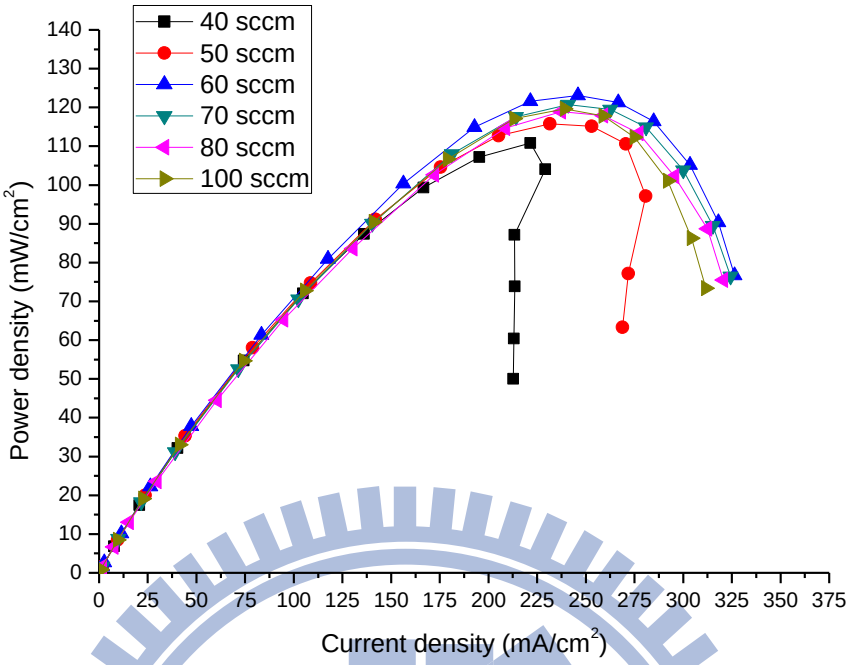

Fig. 4.3 I-P Curves in Different Flow Rates (PDMS PEMFC)

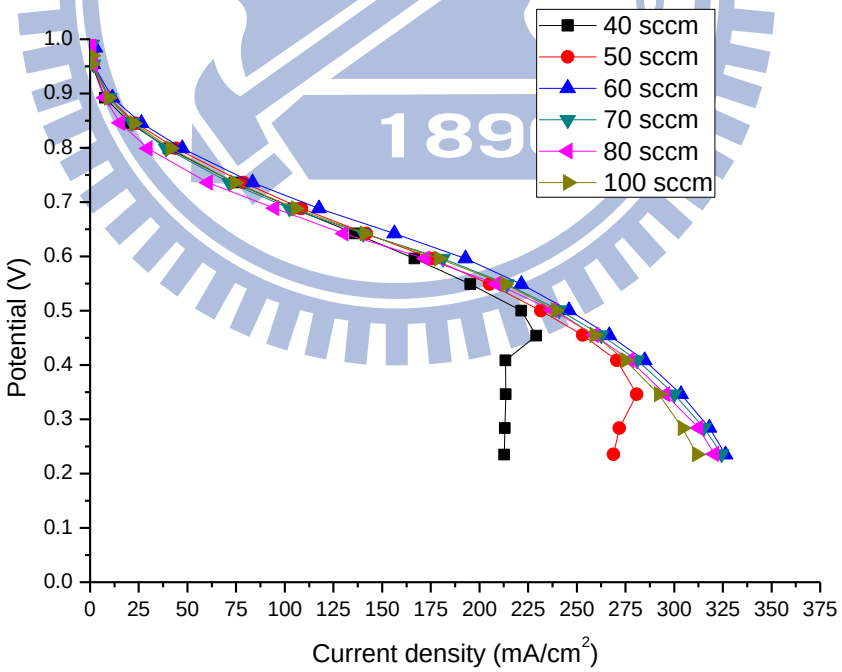

Fig. 4.4 I-V Curves in Different Flow Rates (PDMS PEMFC)

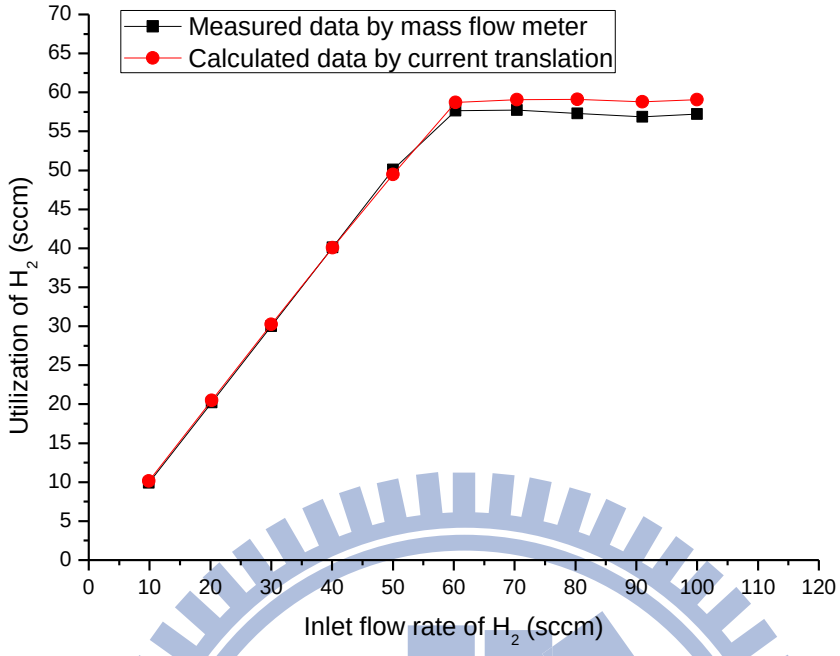

Fig. 4.5 Comparison between Measured and Calculated Utilization (PDMS PEMFC)

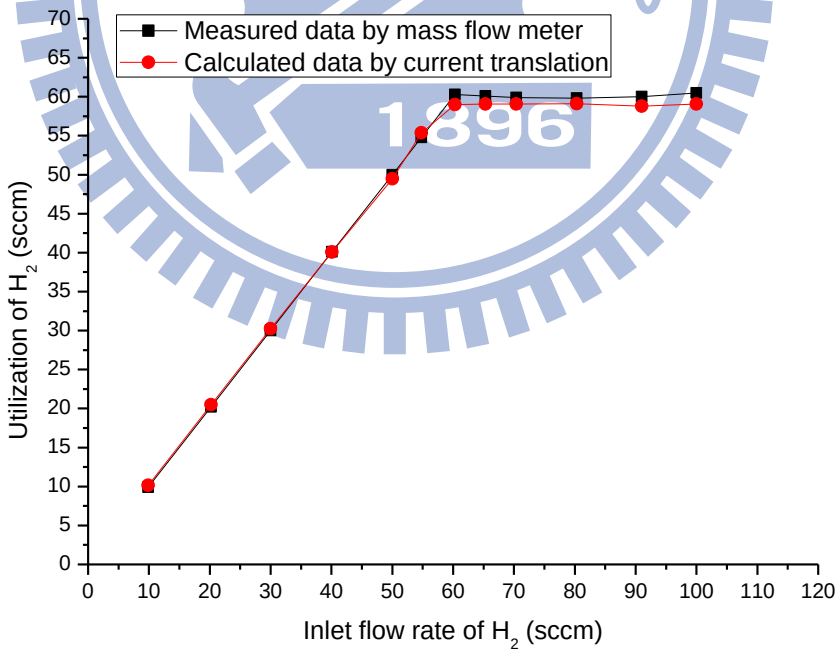

Fig. 4.6 Comparison between Measured and Calculated Utilization after Eliminating Water Vapor (PDMS PEMFC)

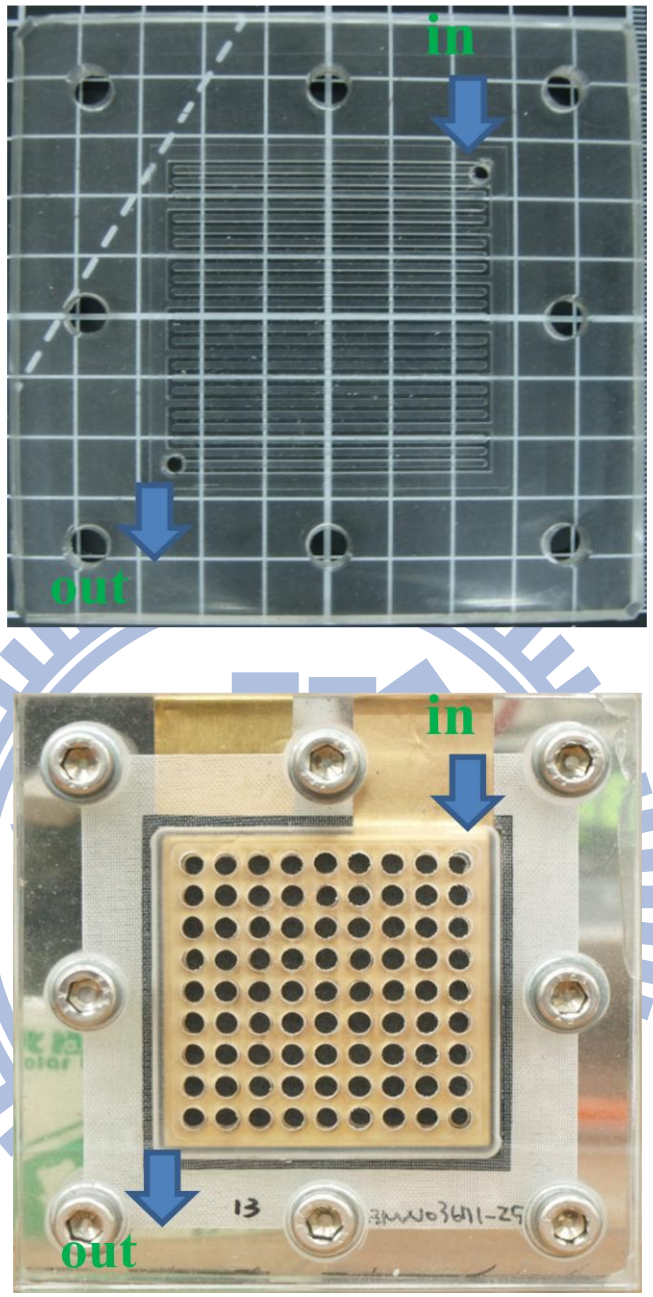

Fig. 4.7 Pictures of Inlet and Outlet of Fuel Cell (PDMS PEMFC)

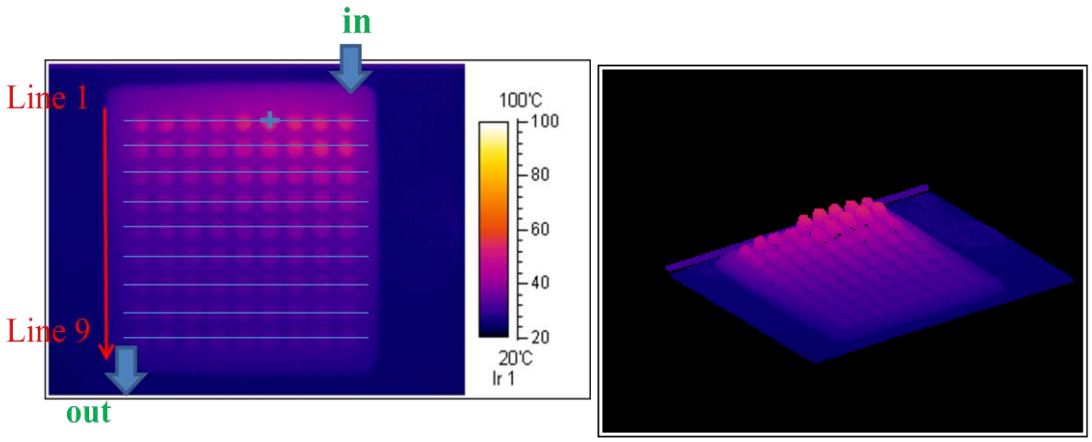

Fig. 4.8 Thermal Images in Hydrogen Flow Rate of 10sccm

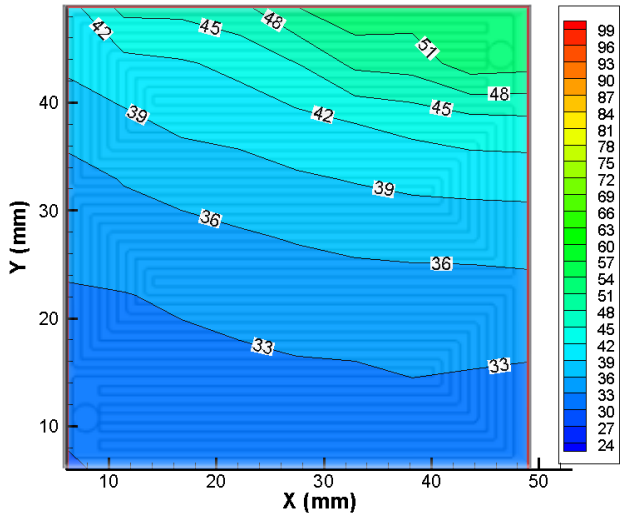

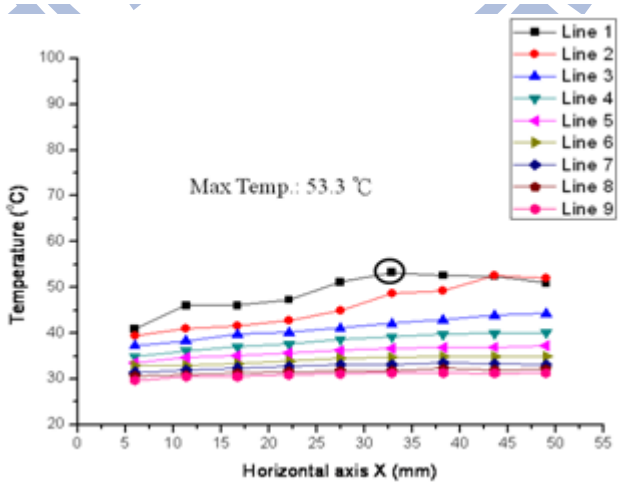

Fig. 4.9 Temperature Distribution Analyses in Hydrogen Flow Rate of 10sccm (PDMS PEMFC)

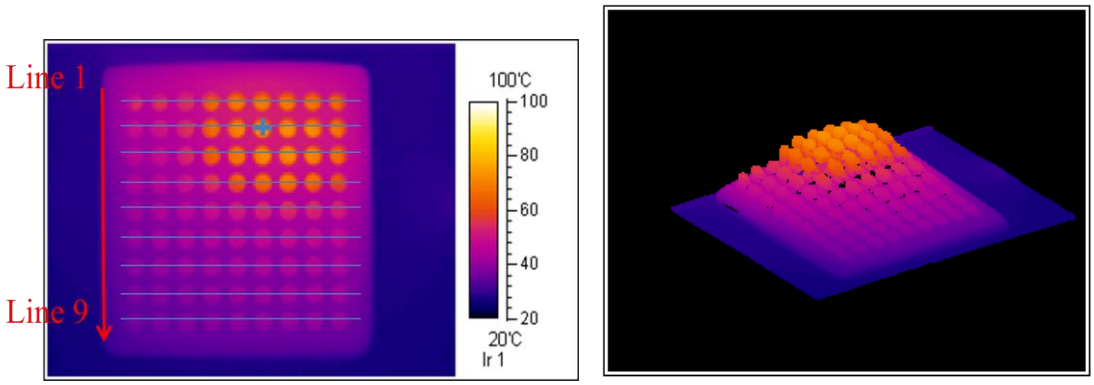

Fig. 4.10 Thermal Images in Hydrogen Flow Rate of 20sccm

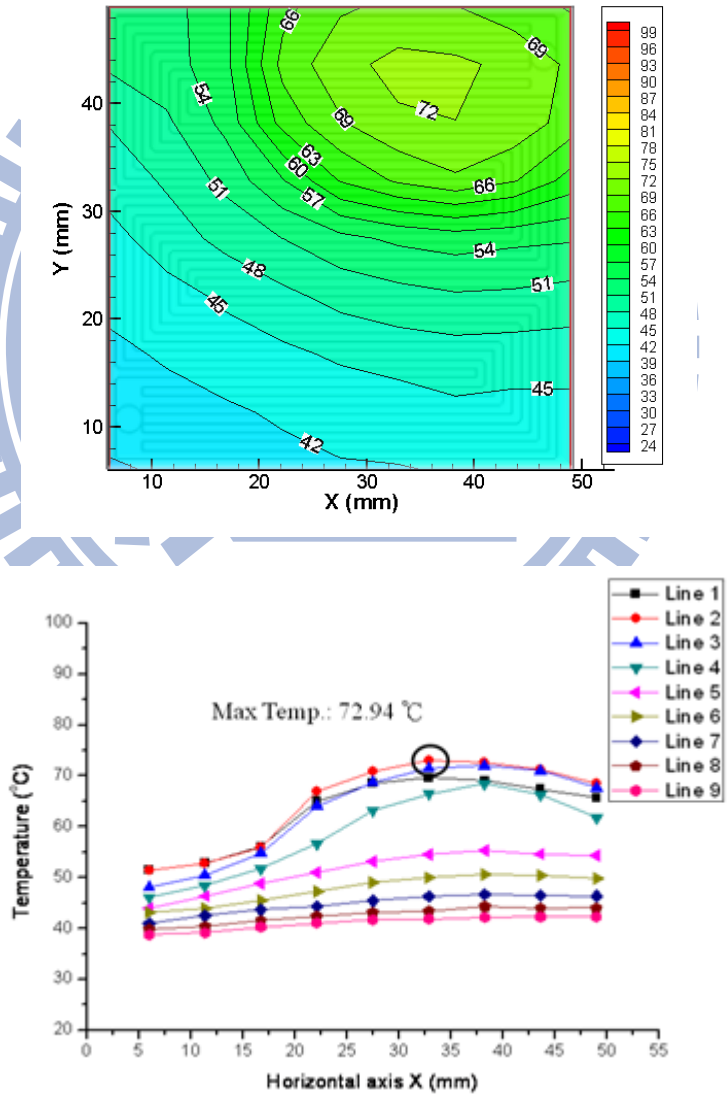

Fig. 4.11 Temperature Distribution Analyses in Hydrogen Flow Rate of 20sccm (PDMS PEMFC)

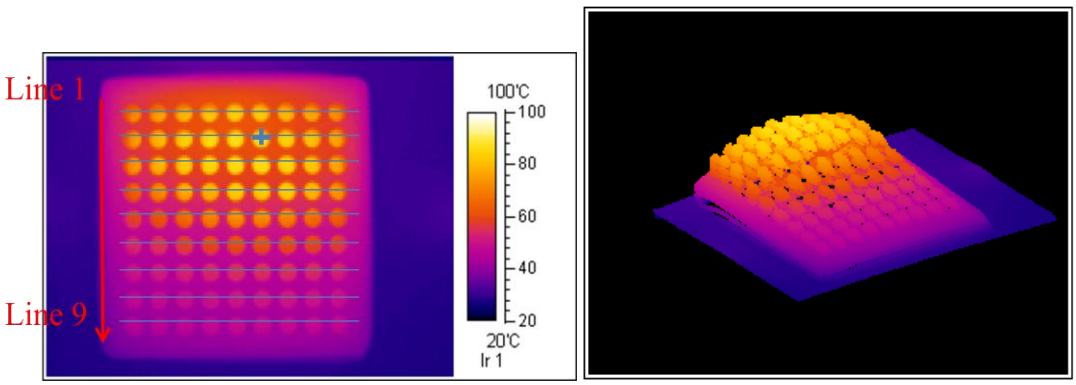

Fig. 4.12 Thermal Images in Hydrogen Flow Rate of 30sccm

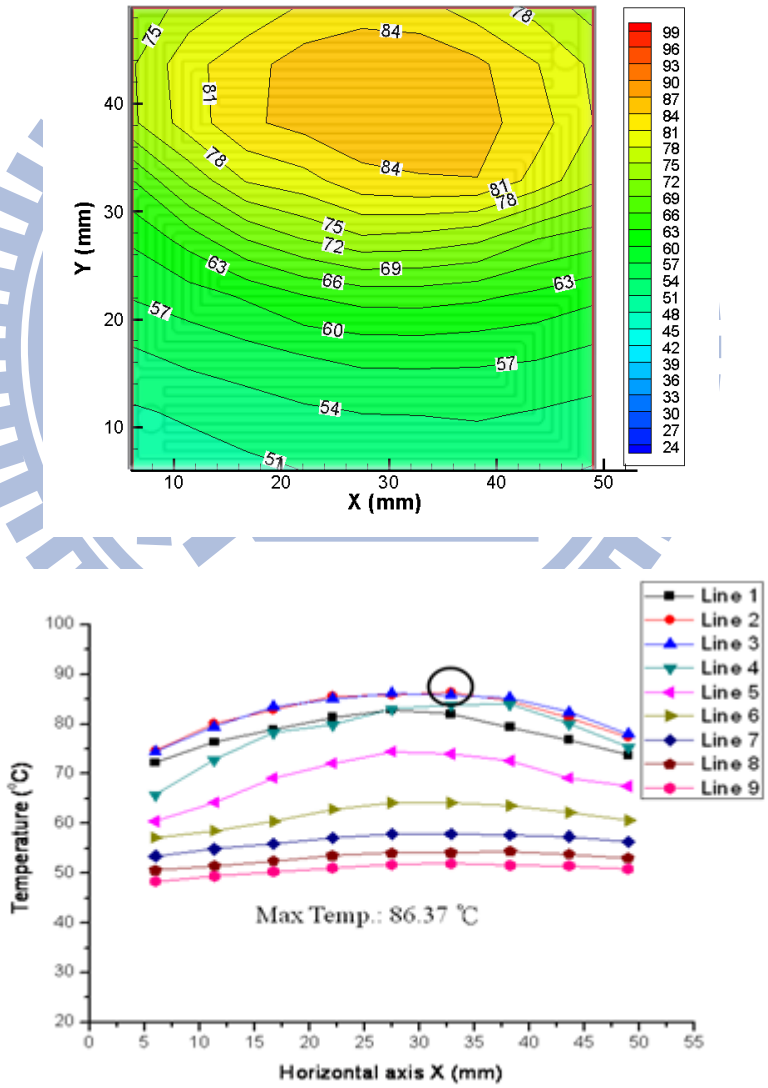

Fig. 4.13 Temperature Distribution Analyses in Hydrogen Flow Rate of 30sccm (PDMS PEMFC)

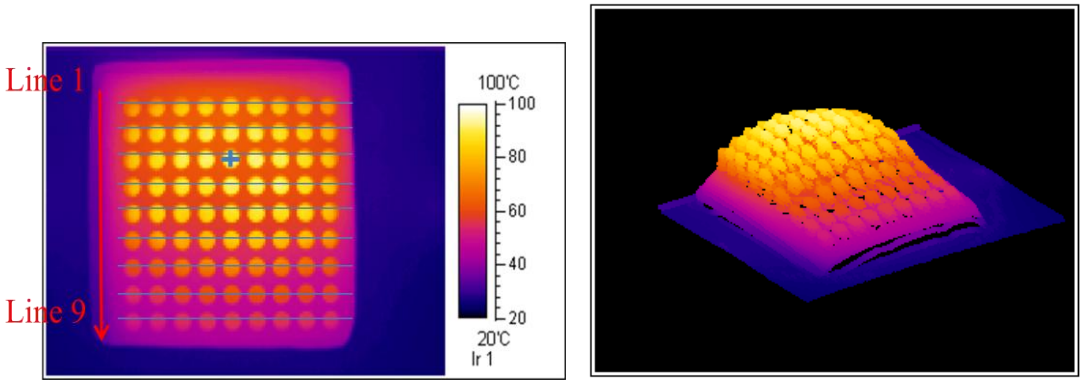

Fig. 4.14 Thermal Images in Hydrogen Flow Rate of 40sccm

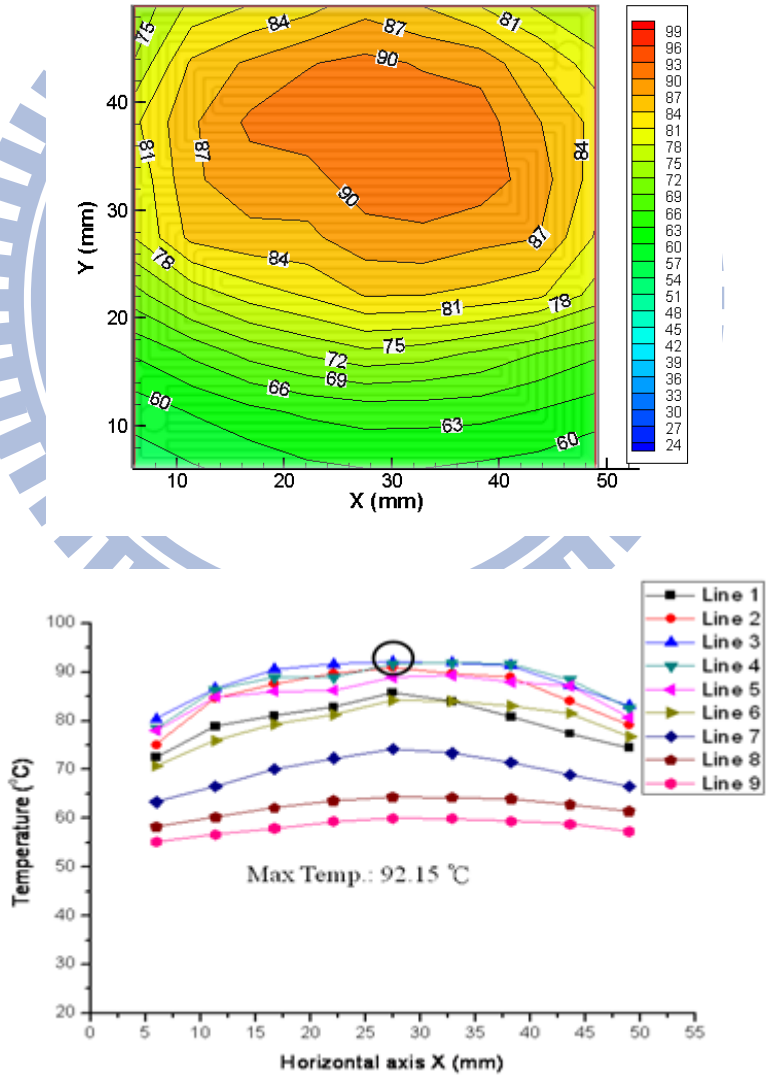

Fig. 4.15 Temperature Distribution Analyses in Hydrogen Flow Rate of 40sccm (PDMS PEMFC)

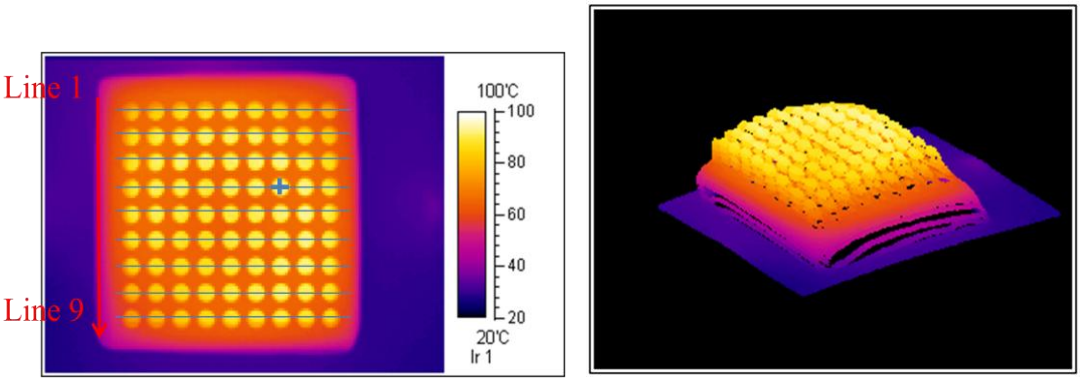

Fig. 4.16 Thermal Images in Hydrogen Flow Rate of 50sccm

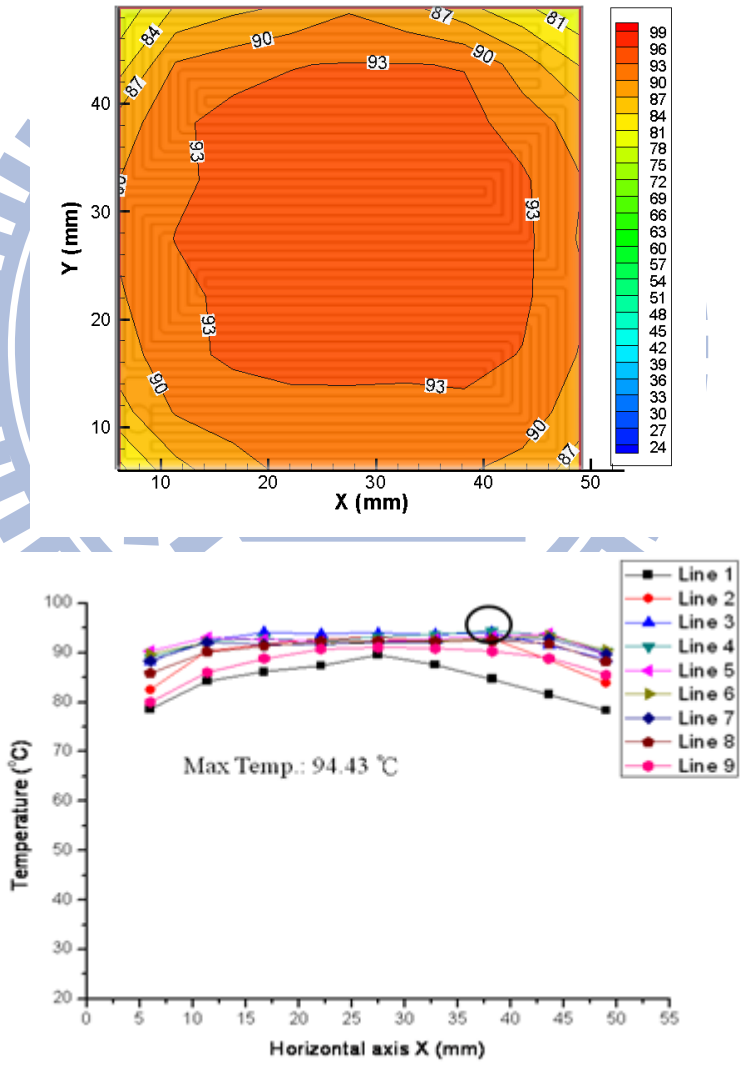

Fig. 4.17 Temperature Distribution Analyses in Hydrogen Flow Rate of 50sccm (PDMS PEMFC)

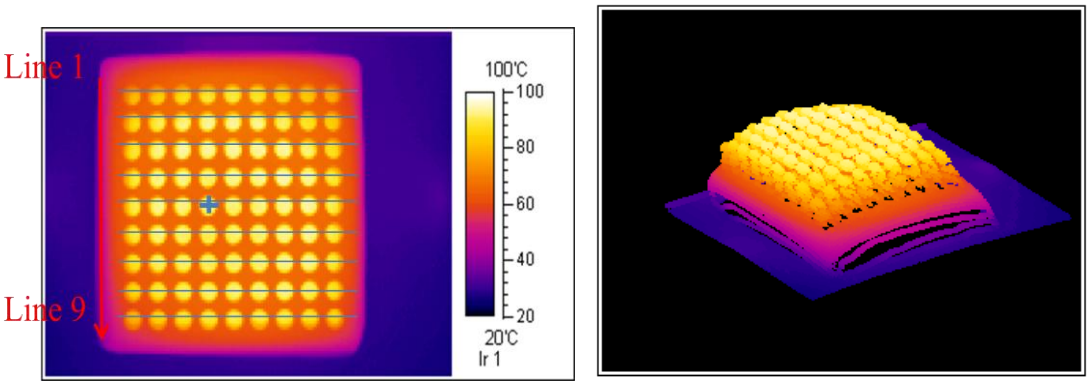

Fig. 4.18 Thermal Images in Hydrogen Flow Rate of 60sccm

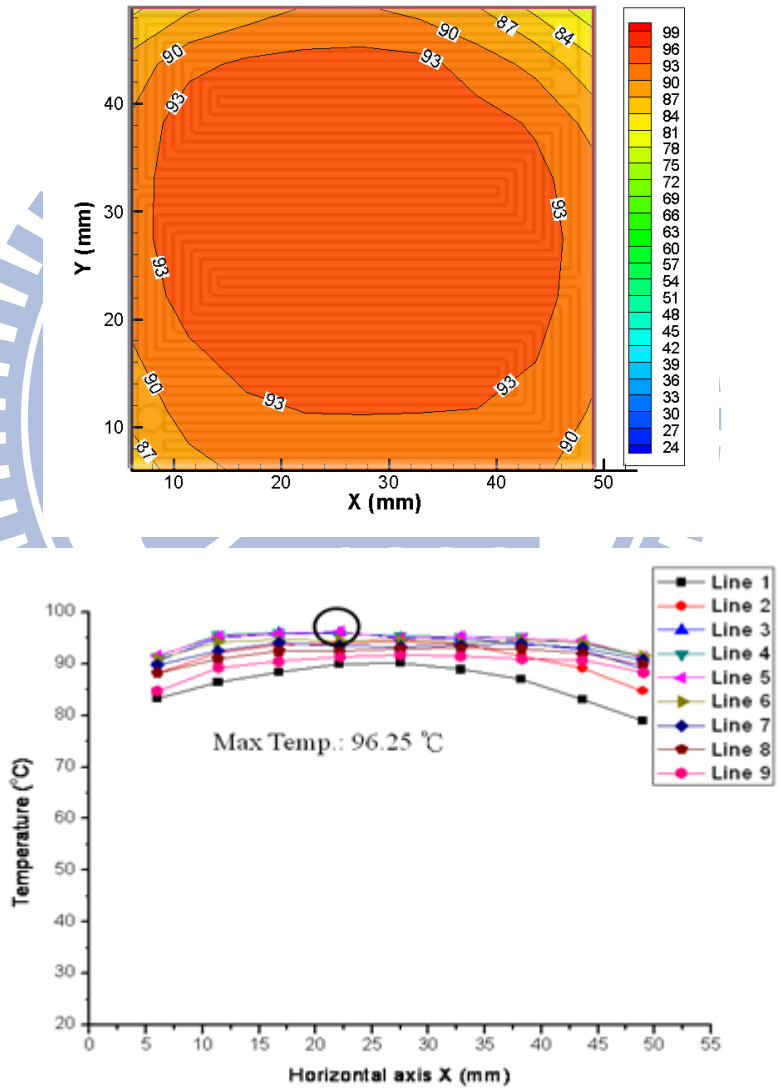

Fig. 4.19 Temperature Distribution Analyses in Hydrogen Flow Rate of 60sccm (PDMS PEMFC)

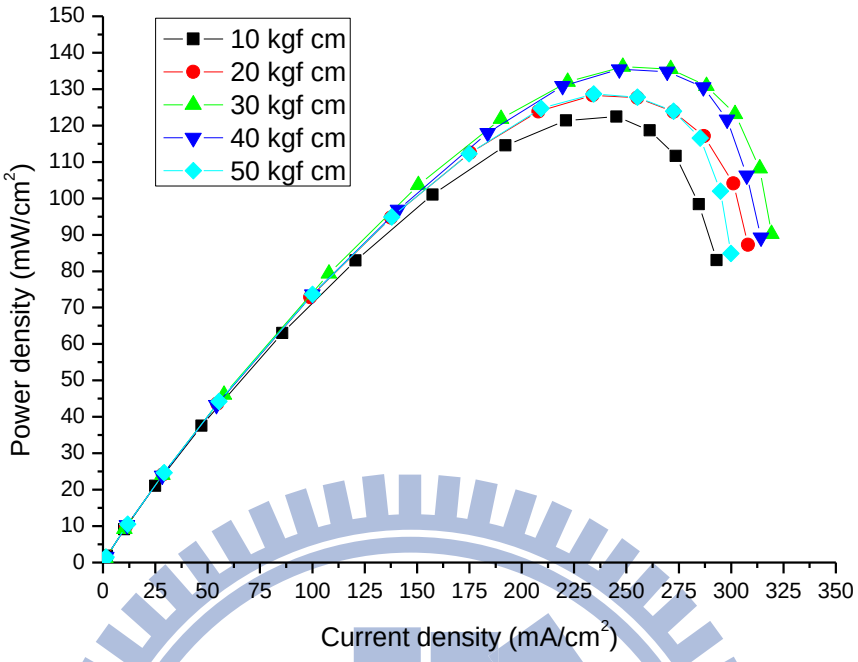

Fig. 4.20 I-P Curves in Different Clamping Forces (PDMS PEMFC)

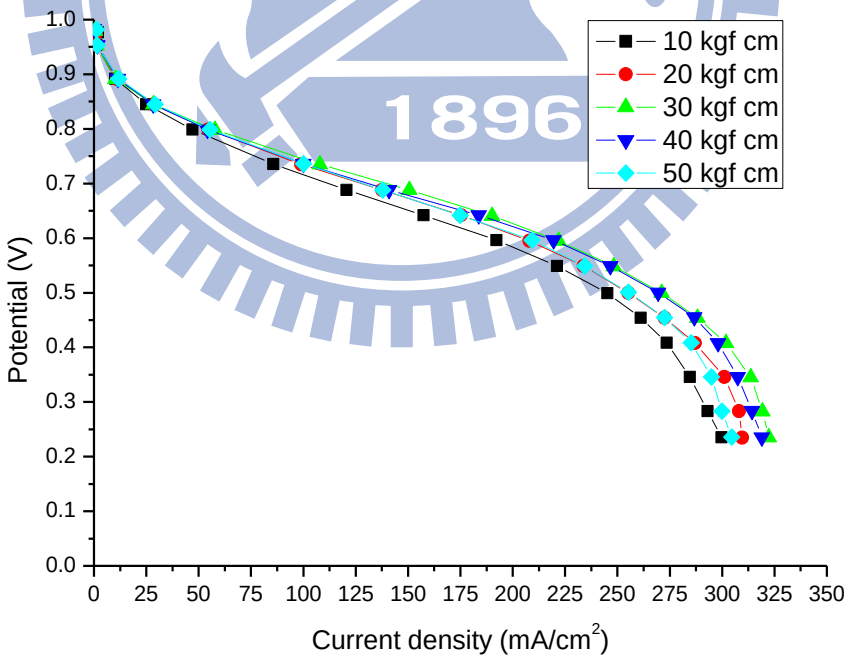

Fig. 4.21 I-V Curves in Different Clamping Forces (PDMS PEMFC)

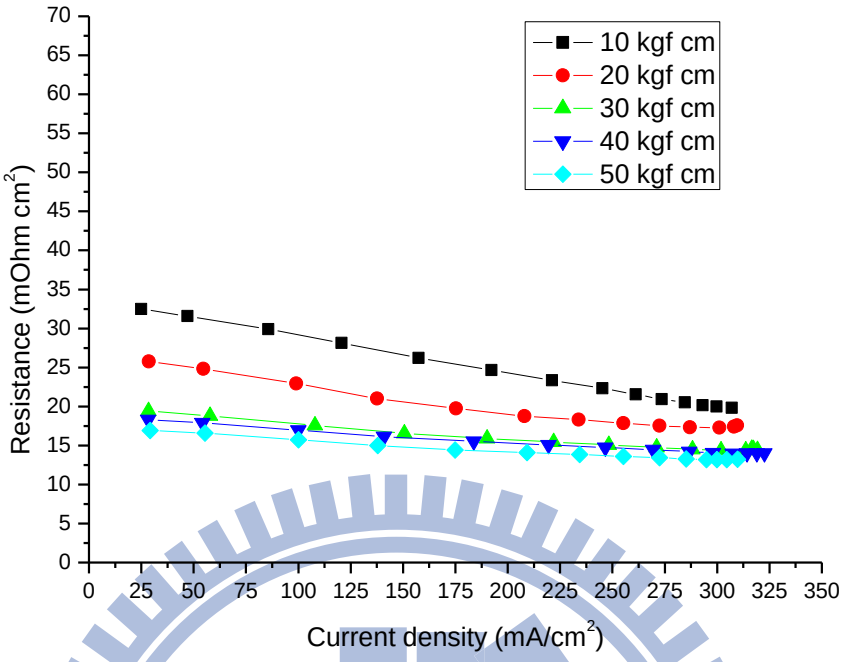

Fig. 4.22 I-R Curves in Different Clamping Forces (PDMS PEMFC)

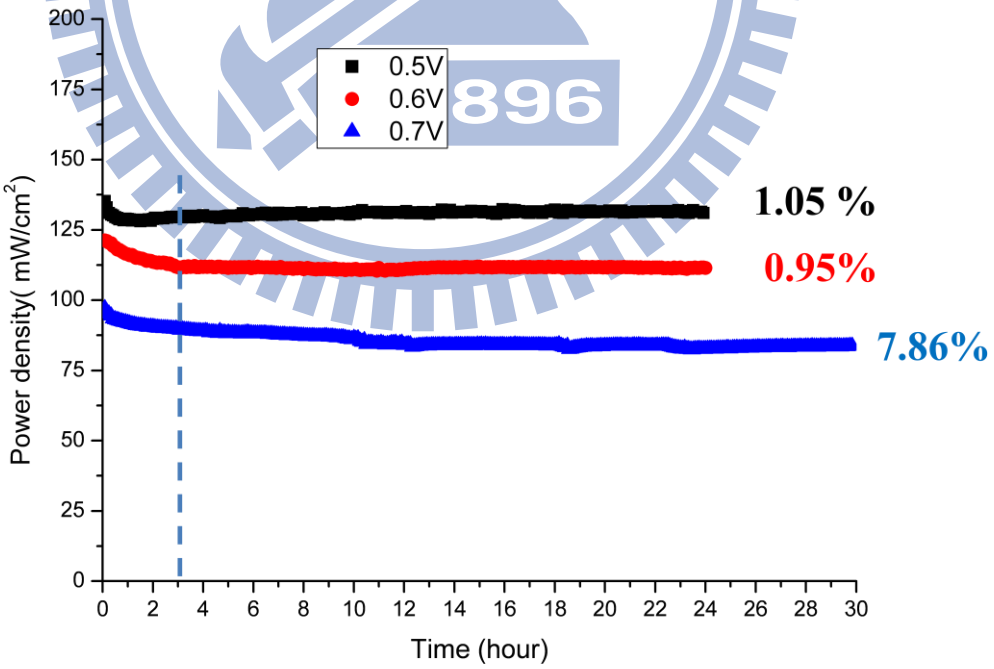

Fig. 4.23 Durability Test for 24 Hours (PDMS PEMFC)

(a) (b)

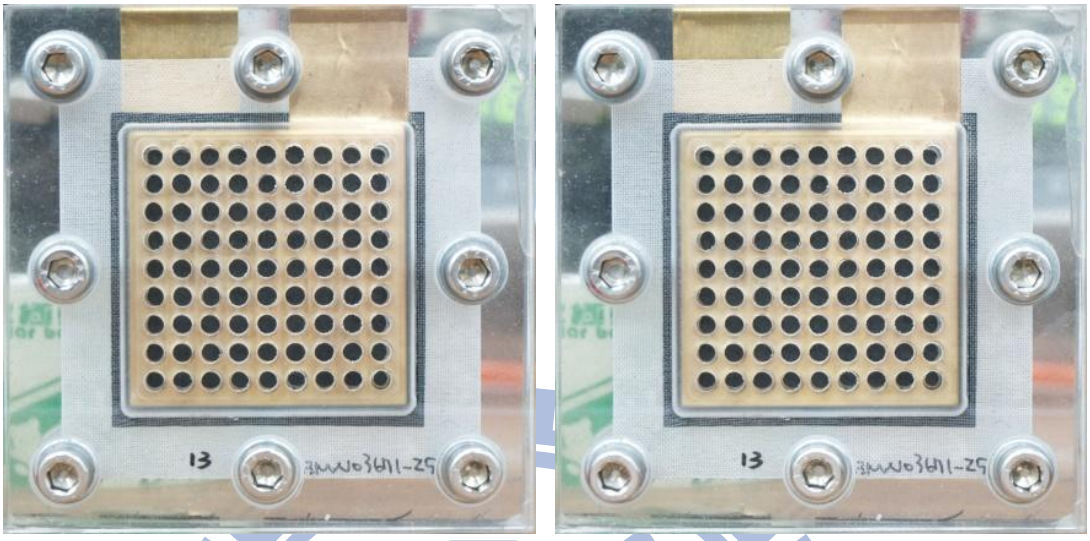

(c) (d)

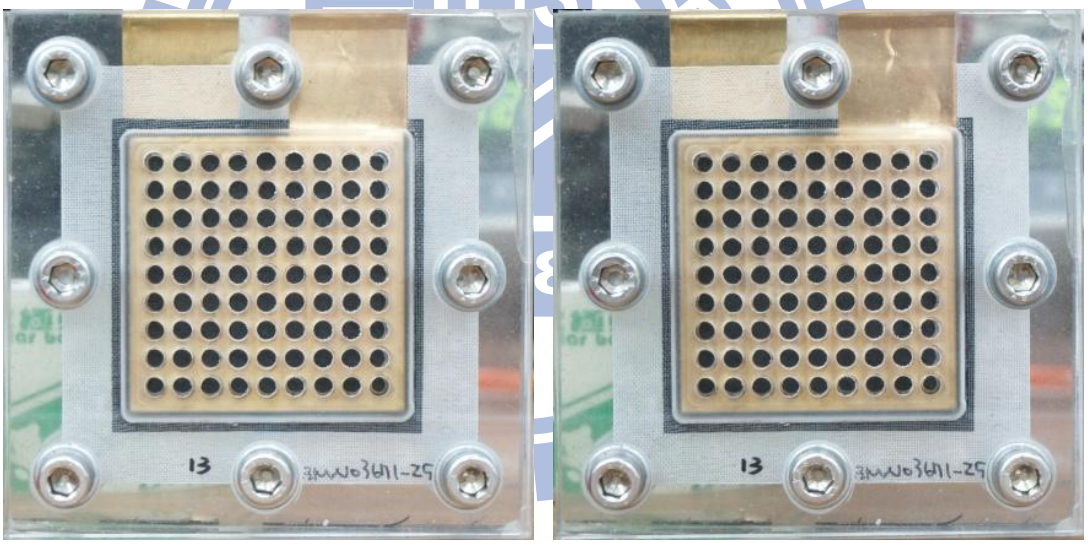

Fig. 4.24 Pictures of Water Accumulation at 0.5V (PDMS PEMFC) (a) 6 hours (b) 12 hours (c) 18 hours (d) 24 hours

(a) (b)

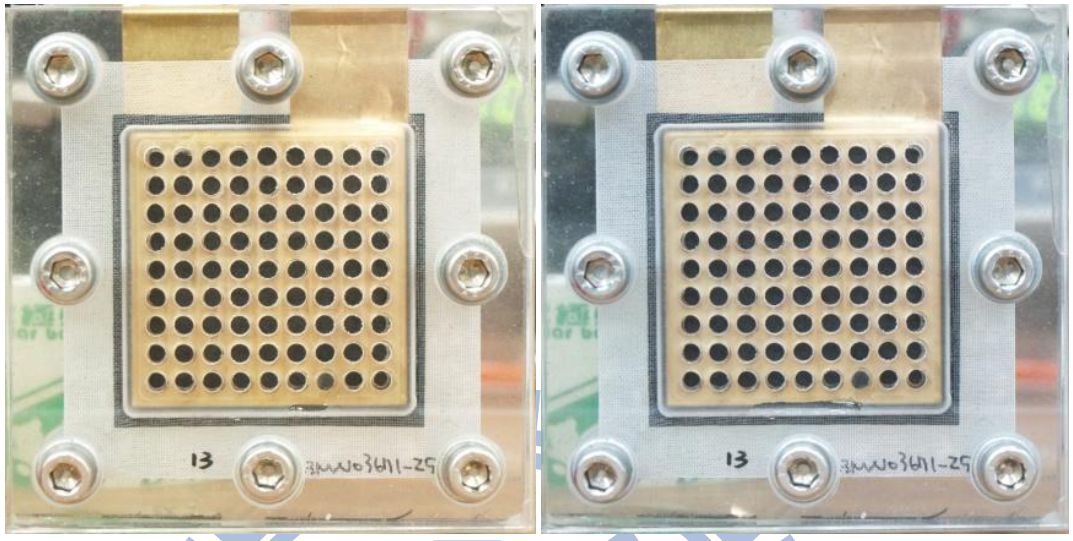

(c) (d)

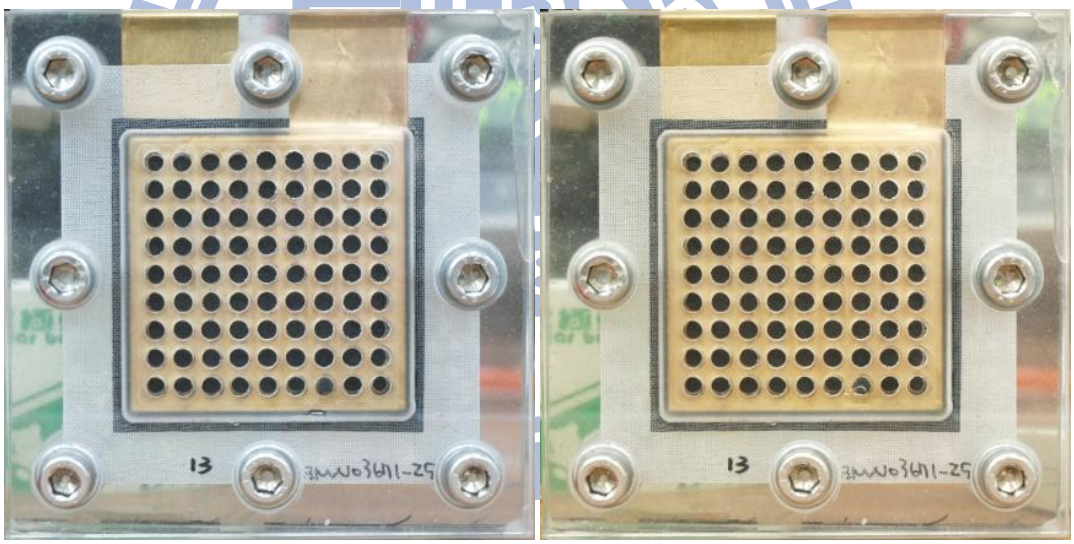

Fig. 4.25 Pictures of Water Accumulation at 0.6V (PDMS PEMFC) (a) 6 hours (b) 12 hours (c) 18 hours (d) 24 hours

(a) **(b)**

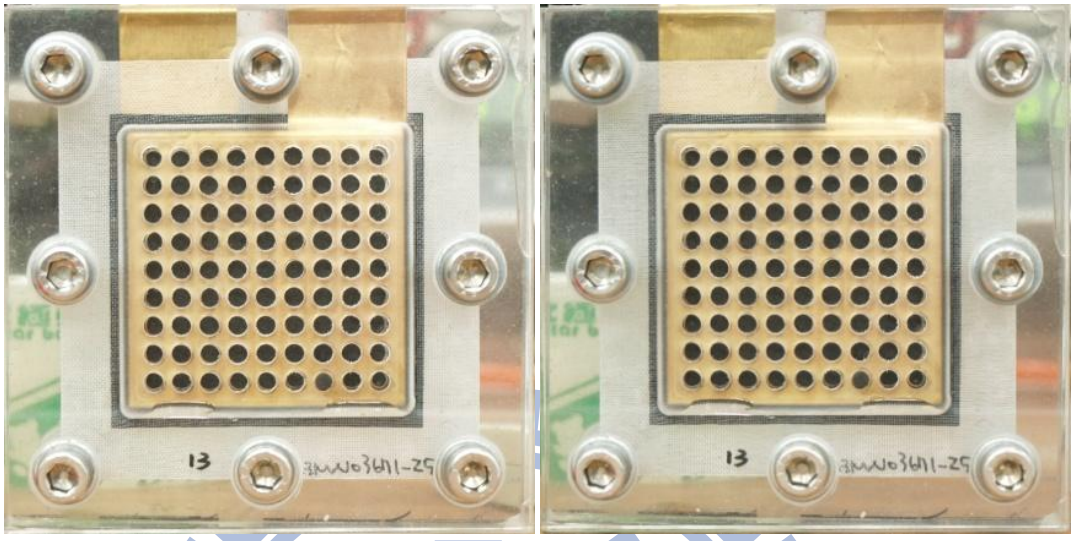

(c) **(d)**

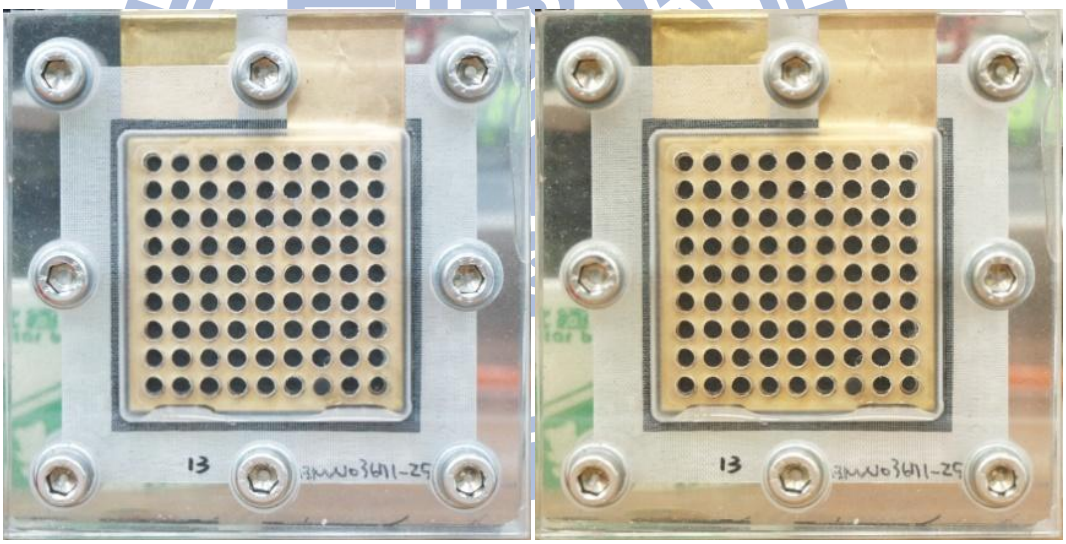

Fig. 4.26 Pictures of Water Accumulation at 0.7V (PDMS PEMFC) (a) 6 hours (b) 12 hours (c) 18 hours (d) 24 hours

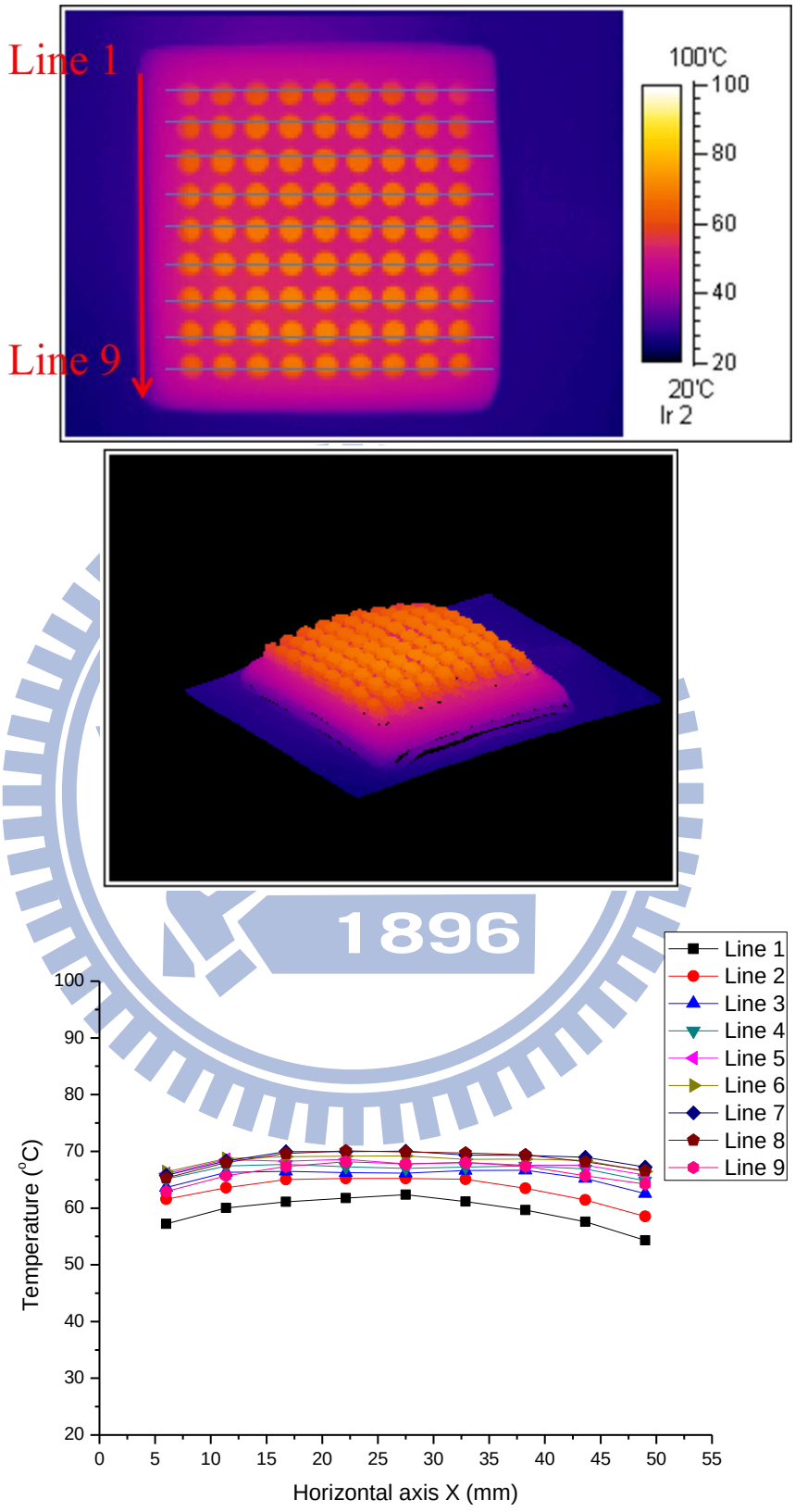

Fig. 4.27 Thermal Images at 0.5V (PDMS PEMFC)

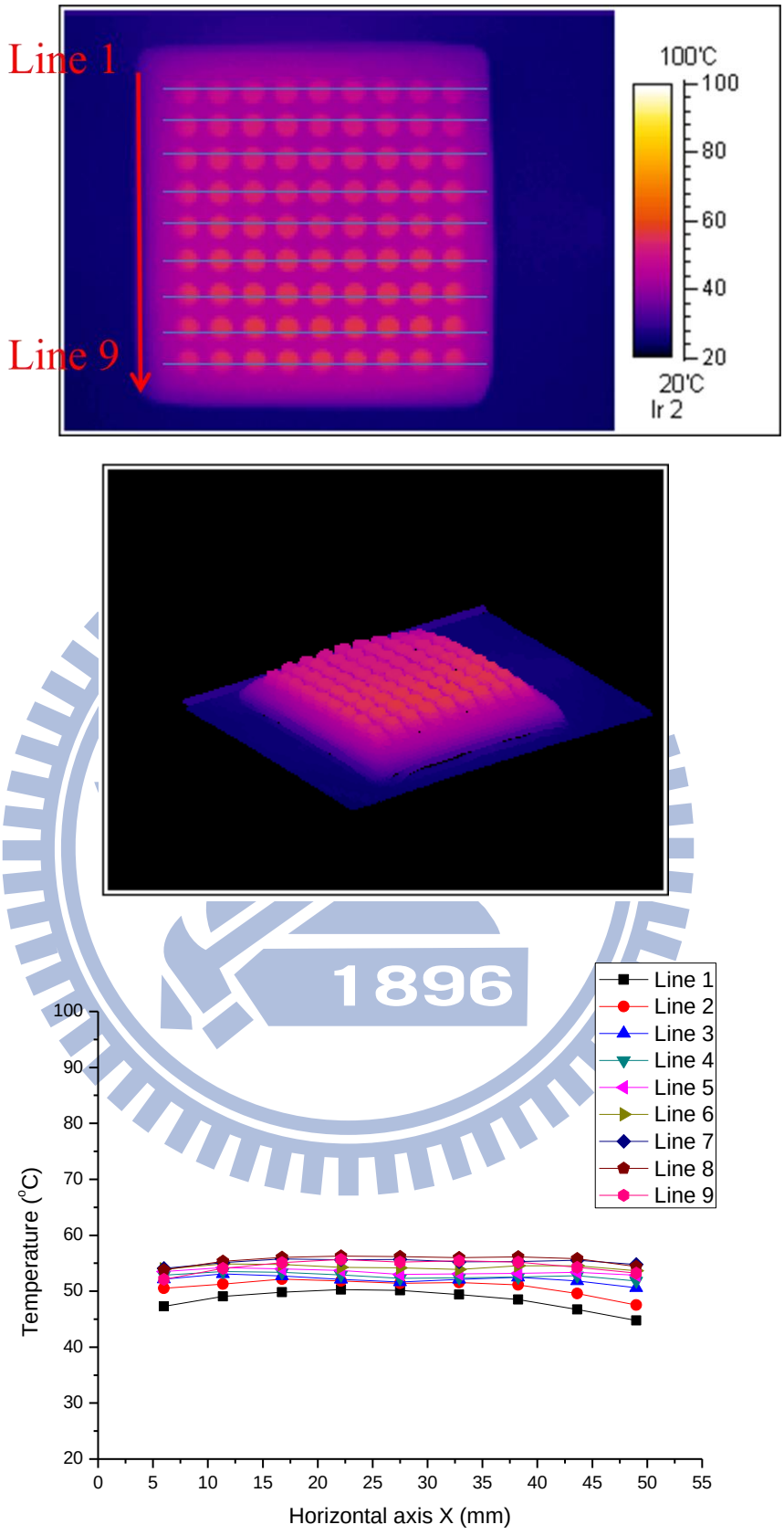

Fig. 4.28 Thermal Images at 0.6V (PDMS PEMFC)

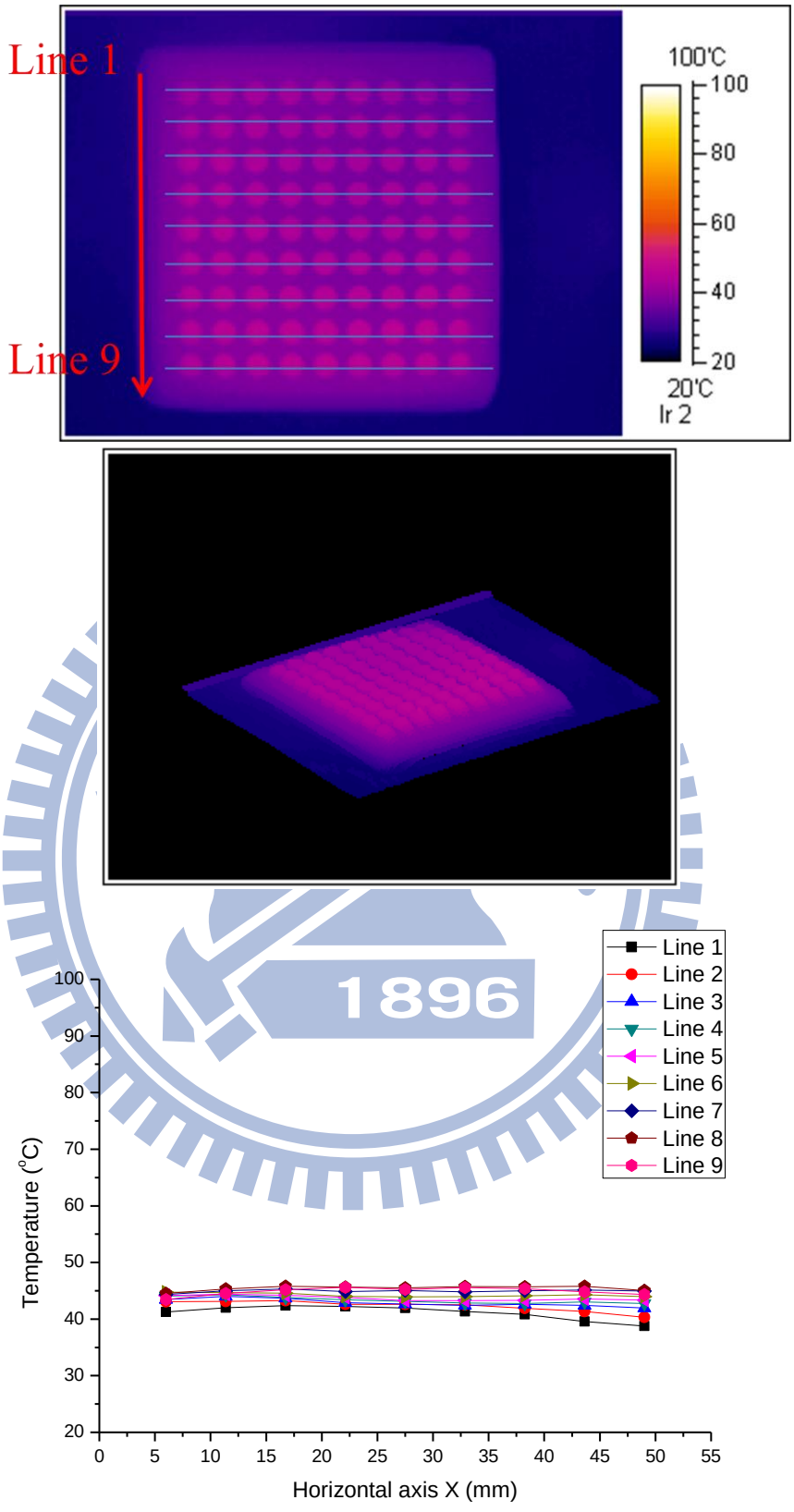

Fig. 4.29 Thermal Images at 0.7V (PDMS PEMFC)

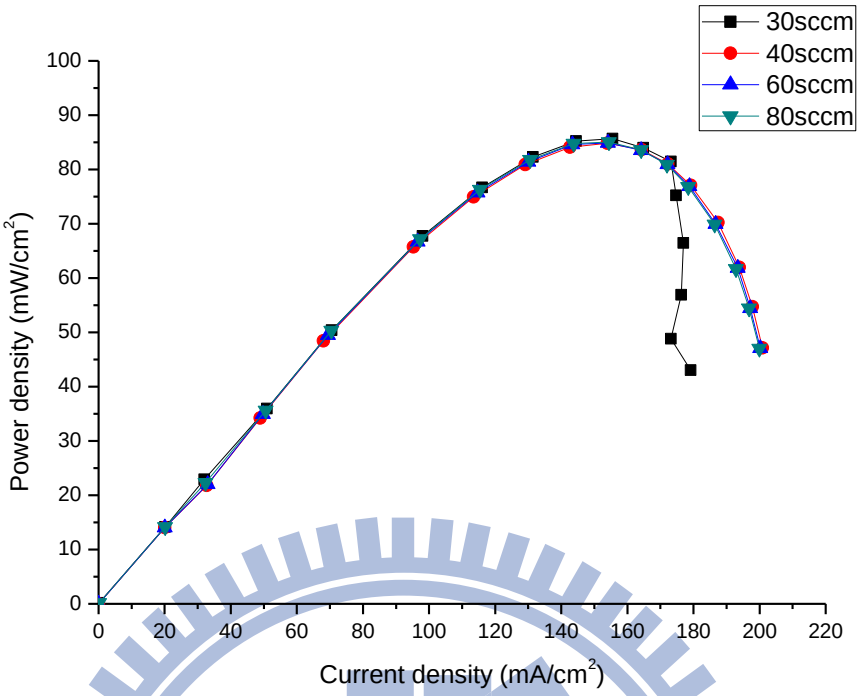

Fig. 4.30 I-P Curves in Different Flow Rates (Graphite PEMFC)

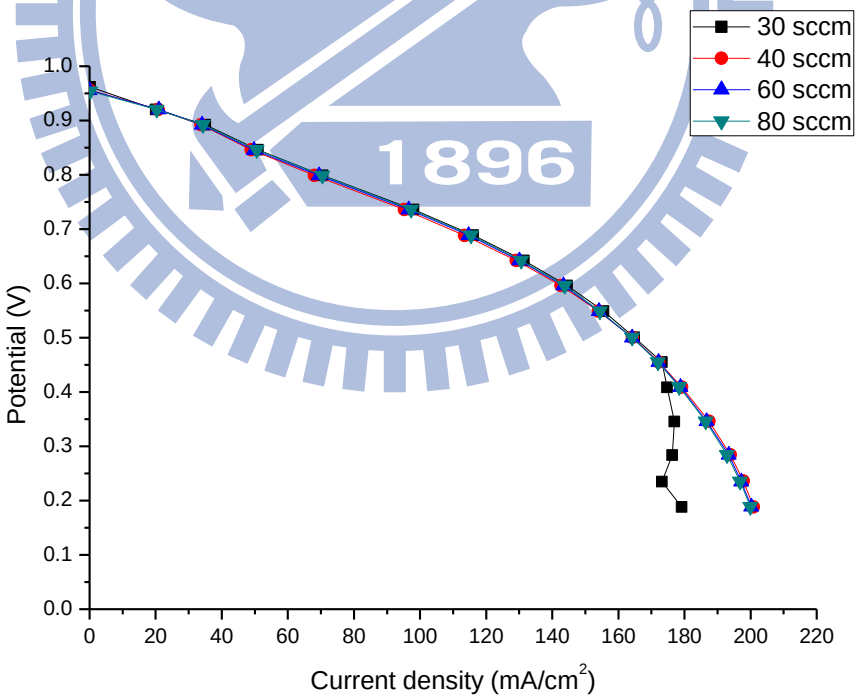

Fig. 4.31 I-V Curves in Different Flow Rates (Graphite PEMFC)

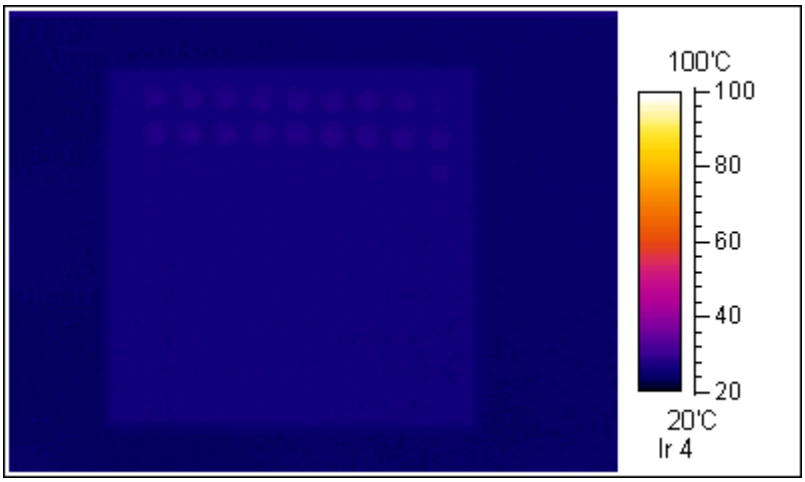

Fig. 4.32 Thermal Images in Hydrogen Flow Rate of 10sccm (Graphite PEMFC)

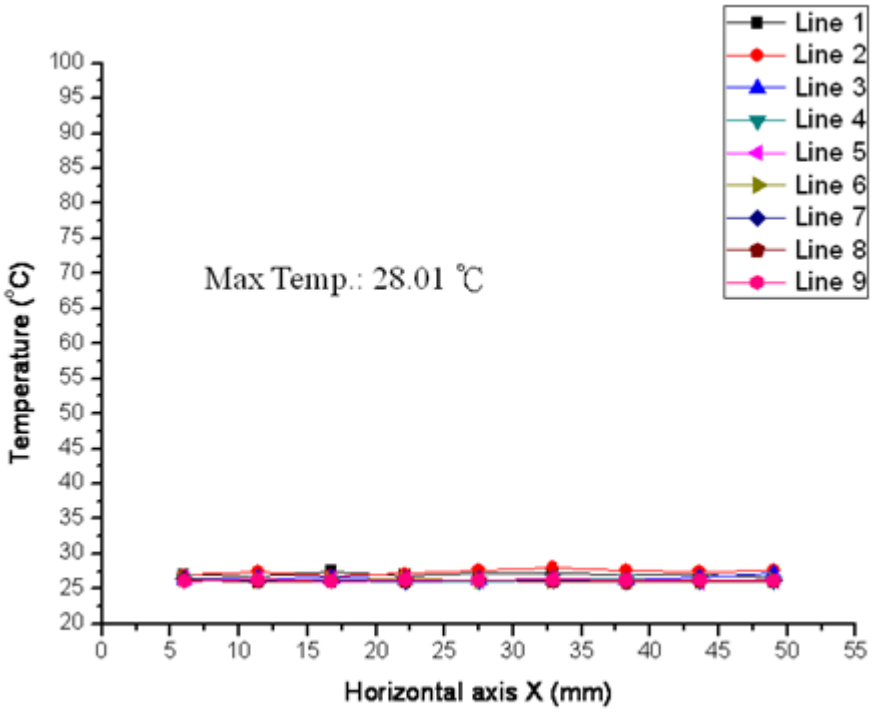

Fig. 4.33 Temperature Distribution Analyses in Hydrogen Flow Rate of 10sccm (Graphite PEMFC)

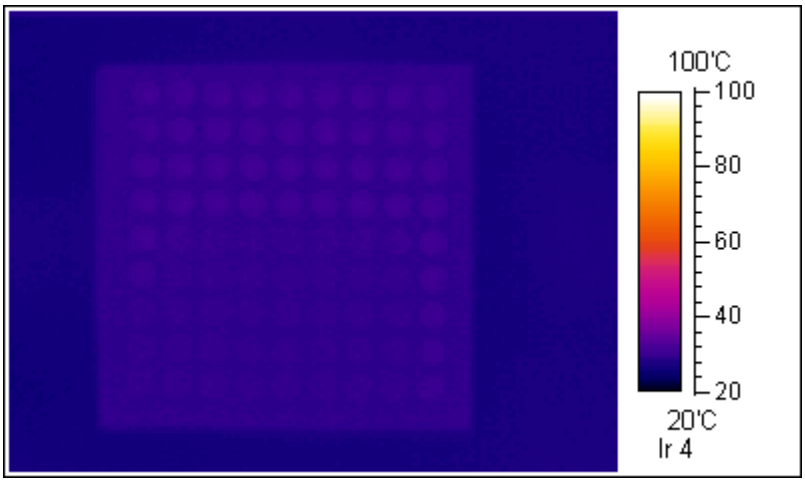

Fig. 4.34 Thermal Images in Hydrogen Flow Rate of 20sccm (Graphite PEMFC)

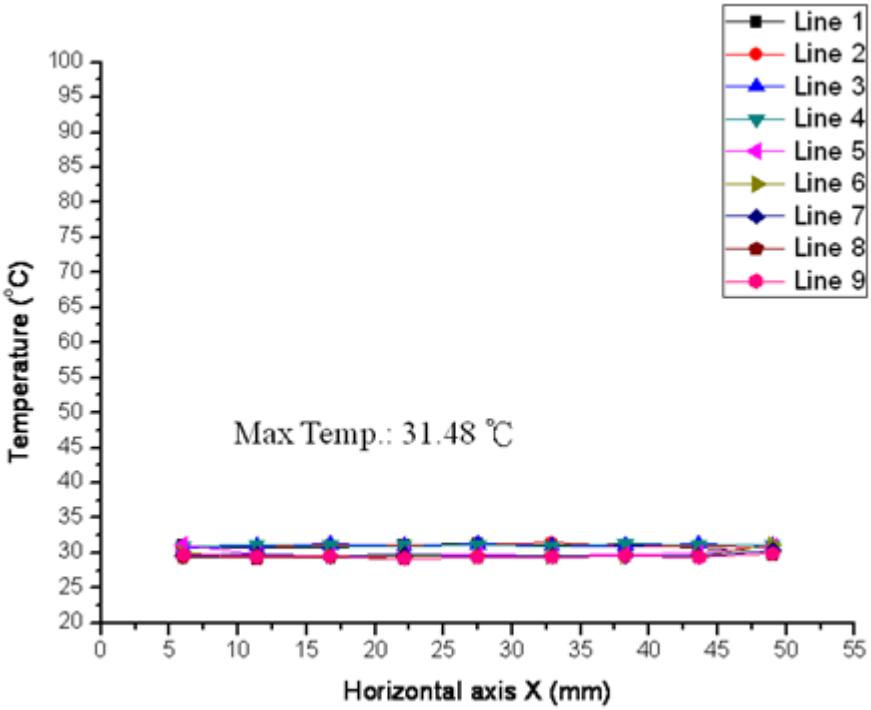

Fig. 4.35 Temperature Distribution Analyses in Hydrogen Flow Rate of 20sccm (Graphite PEMFC)

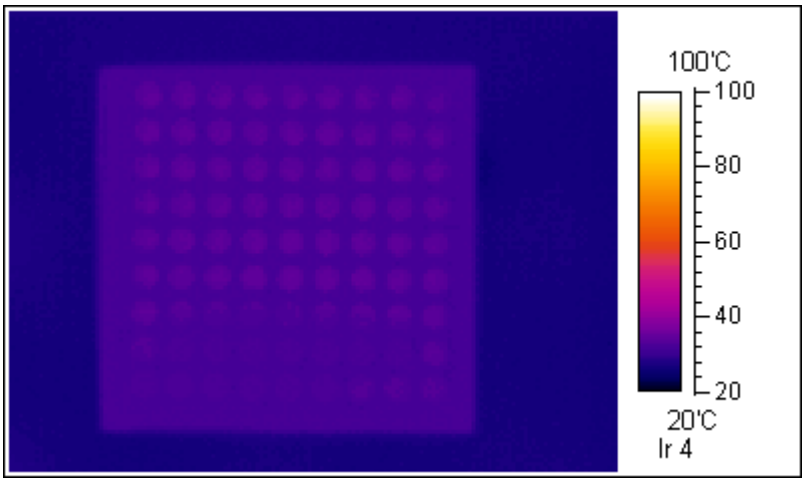

Fig. 4.36 Thermal Images in Hydrogen Flow Rate of 30sccm (Graphite PEMFC)

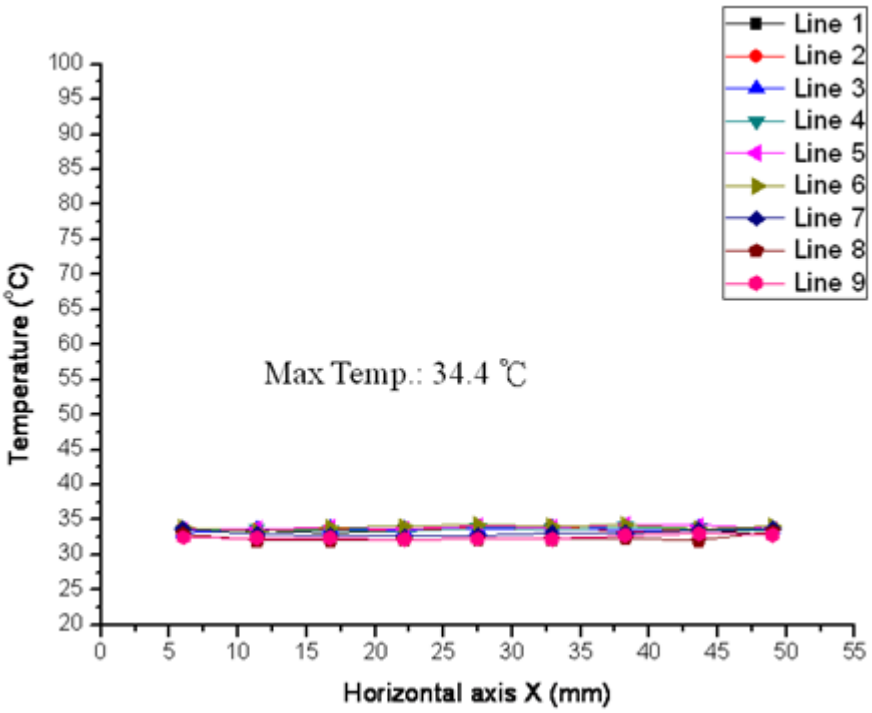

Fig. 4.37 Temperature Distribution Analyses in Hydrogen Flow Rate of 30sccm (Graphite PEMFC)

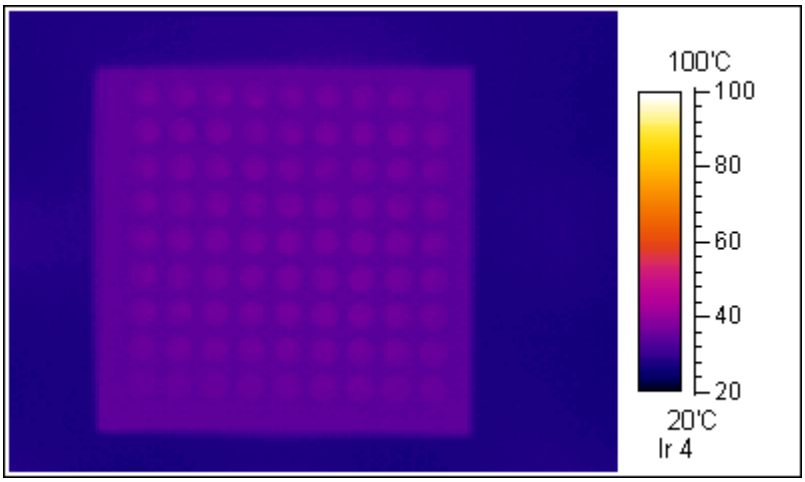

Fig. 4.38 Thermal Images in Hydrogen Flow Rate of 40sccm (Graphite PEMFC)

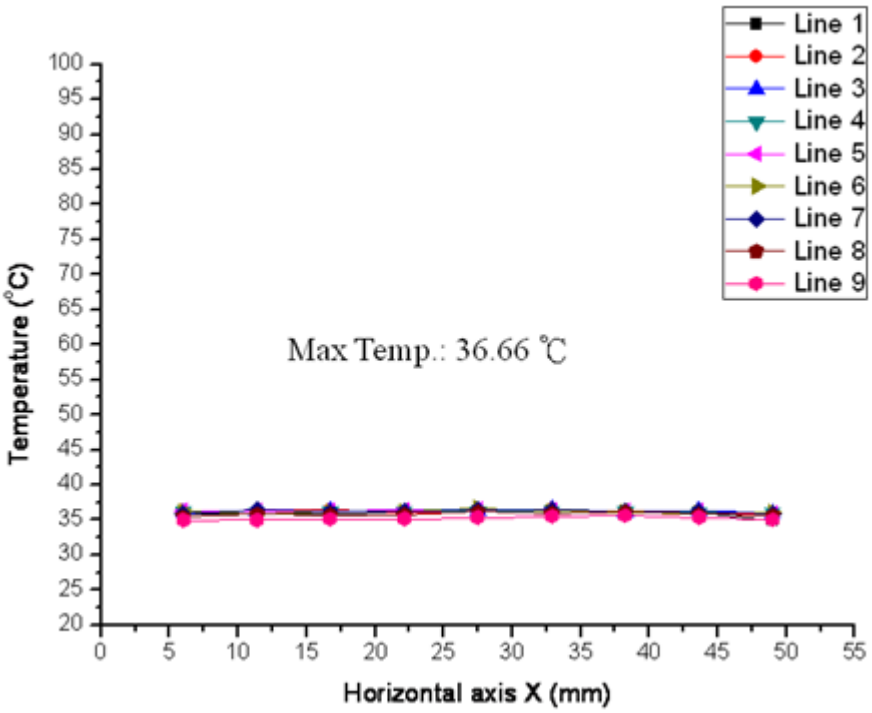

Fig. 4.39 Temperature Distribution Analyses in Hydrogen Flow Rate of 40sccm (Graphite PEMFC)

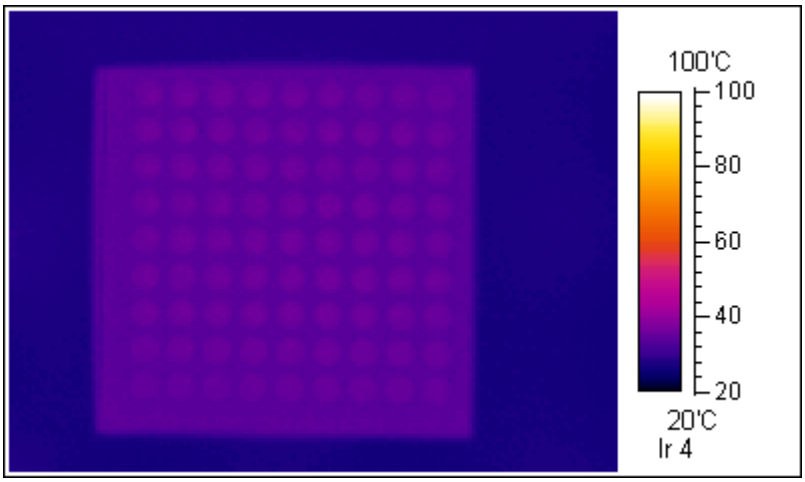

Fig. 4.40 Thermal Images in Hydrogen Flow Rate of 50sccm (Graphite PEMFC)

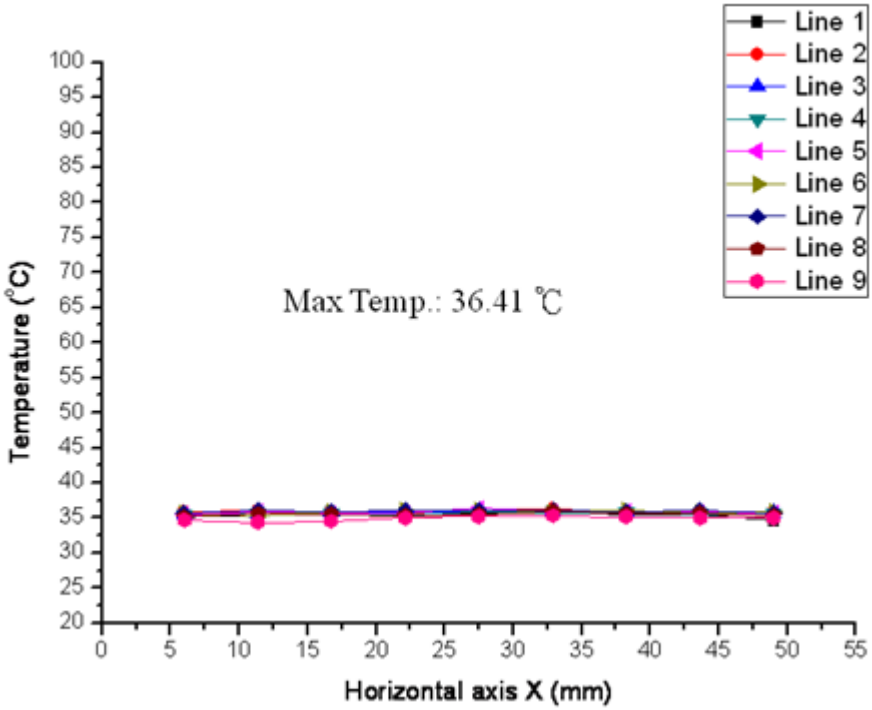

Fig. 4.41 Temperature Distribution Analyses in Hydrogen Flow Rate of 50sccm (Graphite PEMFC)

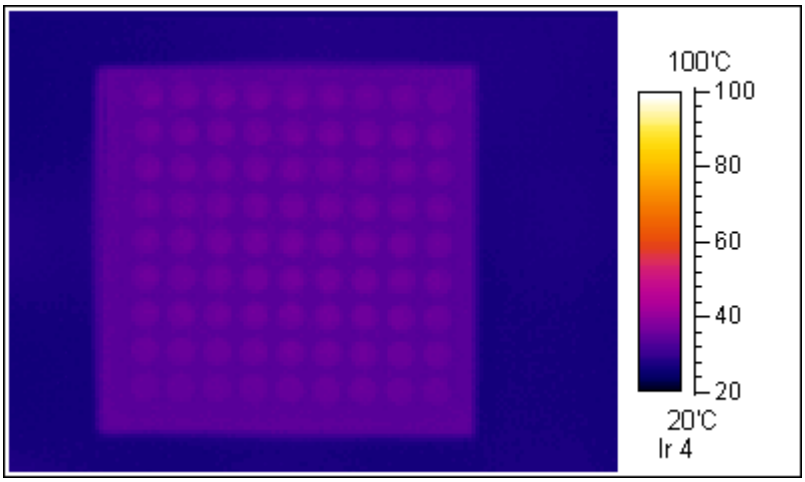

Fig. 4.42 Thermal Images in Hydrogen Flow Rate of 60sccm (Graphite PEMFC)

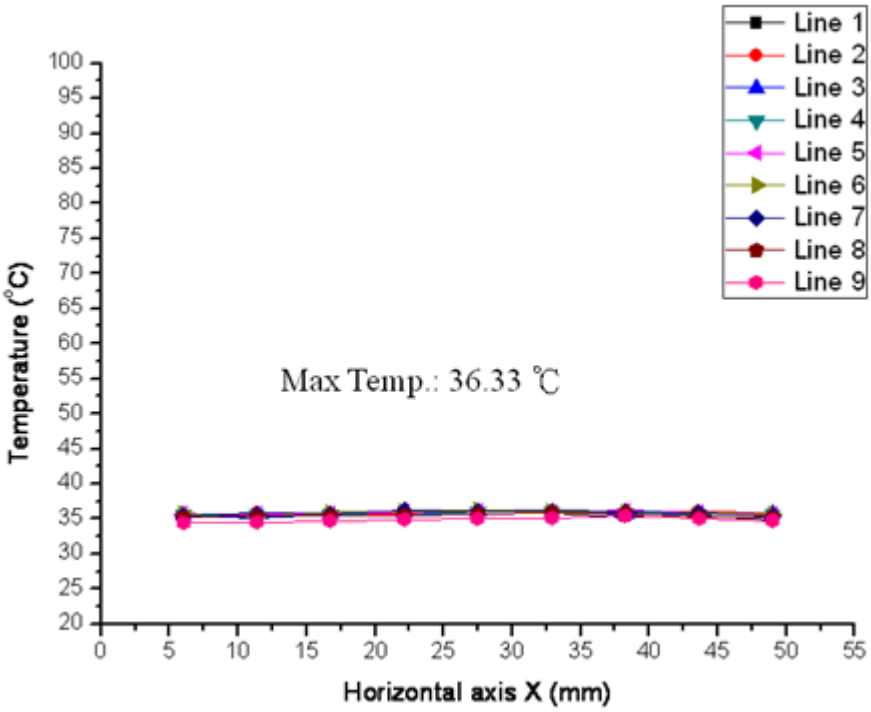

Fig. 4.43 Temperature Distribution Analyses in Hydrogen Flow Rate of 60sccm (Graphite PEMFC)

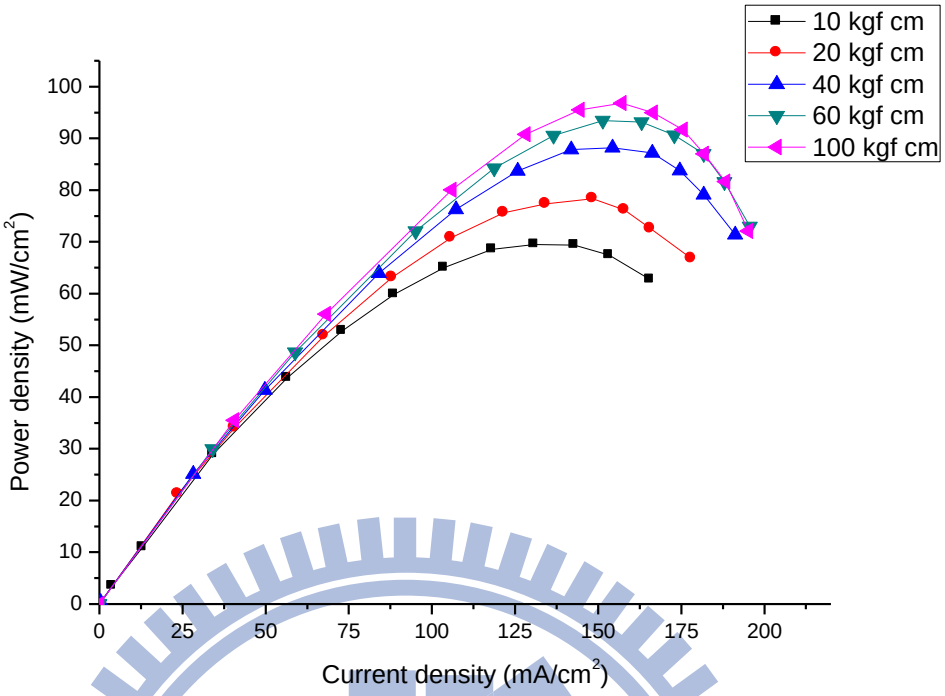

Fig. 4.44 I-P Curves in Different Clamping Forces (Graphite PEMFC)

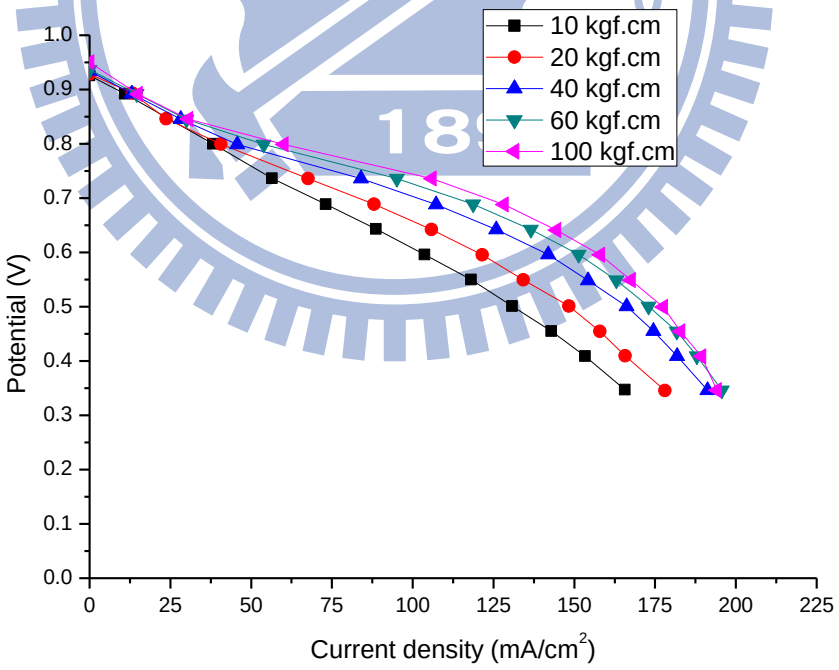

Fig. 4.45 I-V Curves in Different Clamping Forces (Graphite PEMFC)

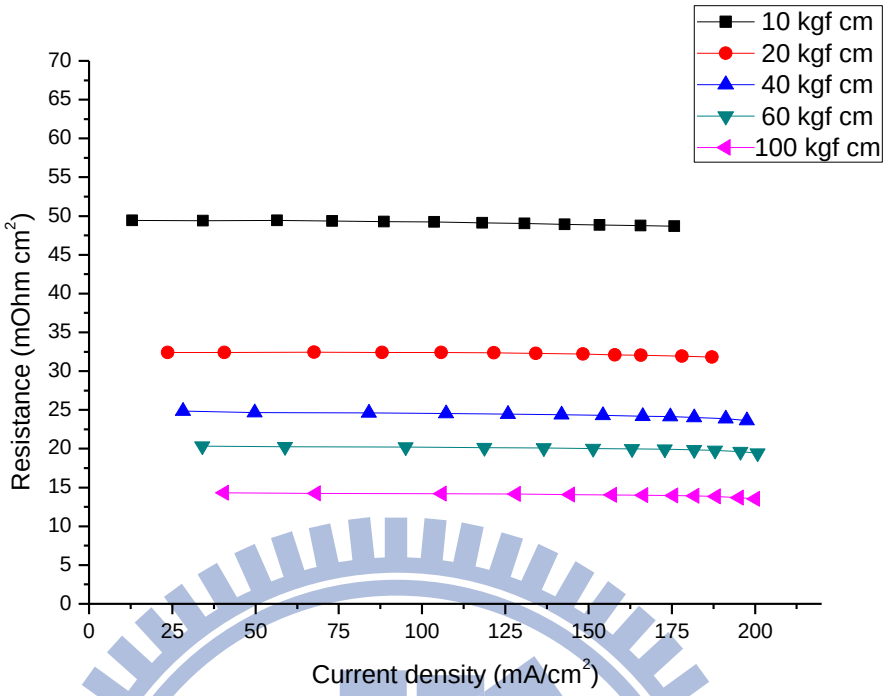

Fig. 4.46 I-R Curves in Different Clamping Forces (Graphite PEMFC)

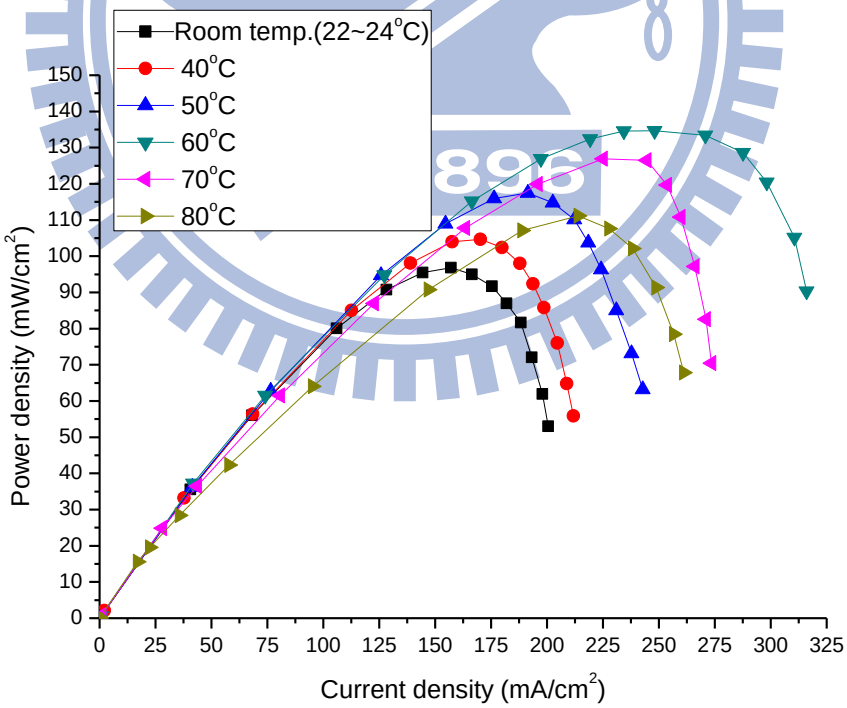

Fig. 4.47 I-P Curves in Different Cell Temperatures (Graphite PEMFC)

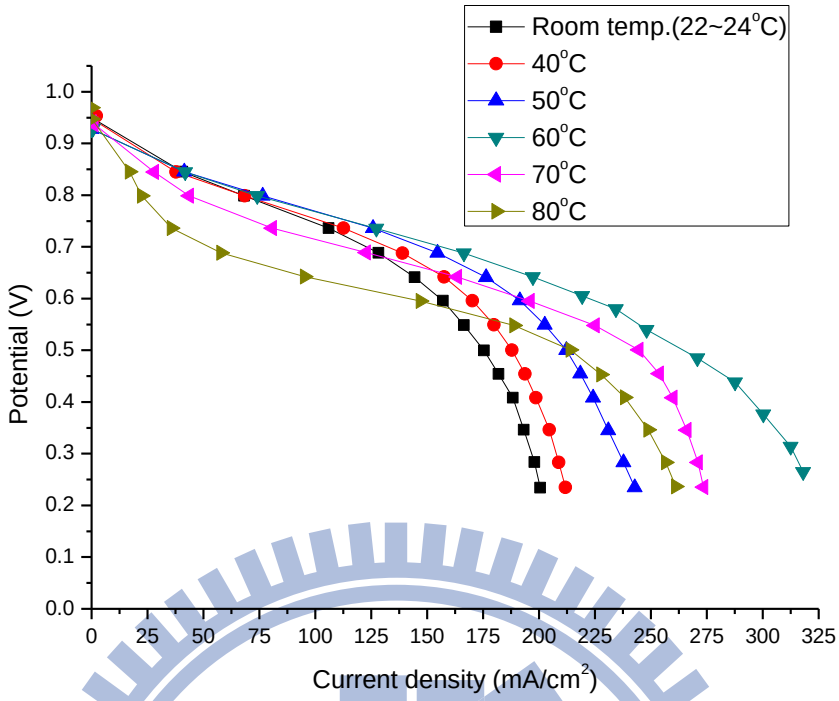

Fig. 4.48 I-V Curves in Different Cell Temperatures (Graphite PEMFC)

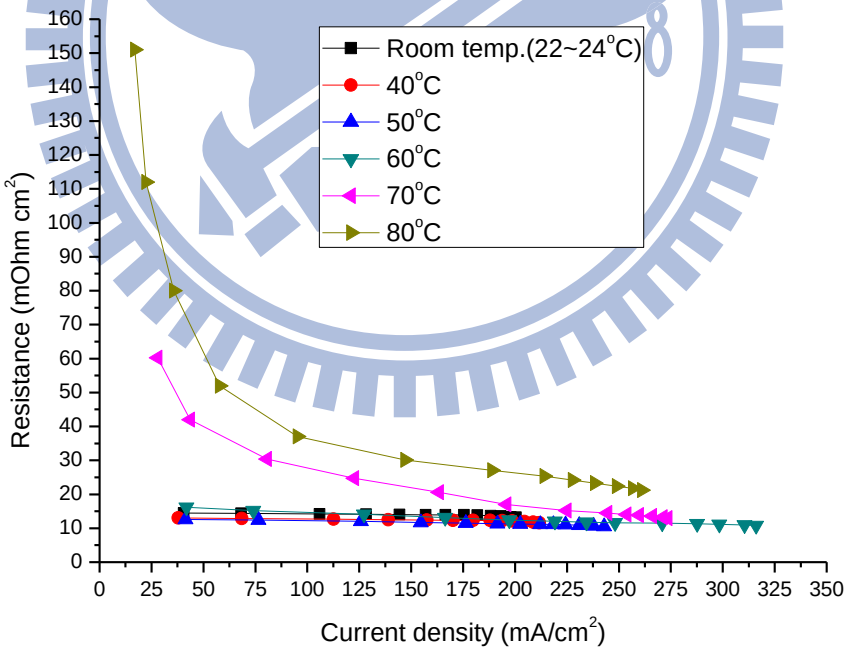

Fig. 4.49 I-R Curves in Different Cell Temperatures (Graphite PEMFC)

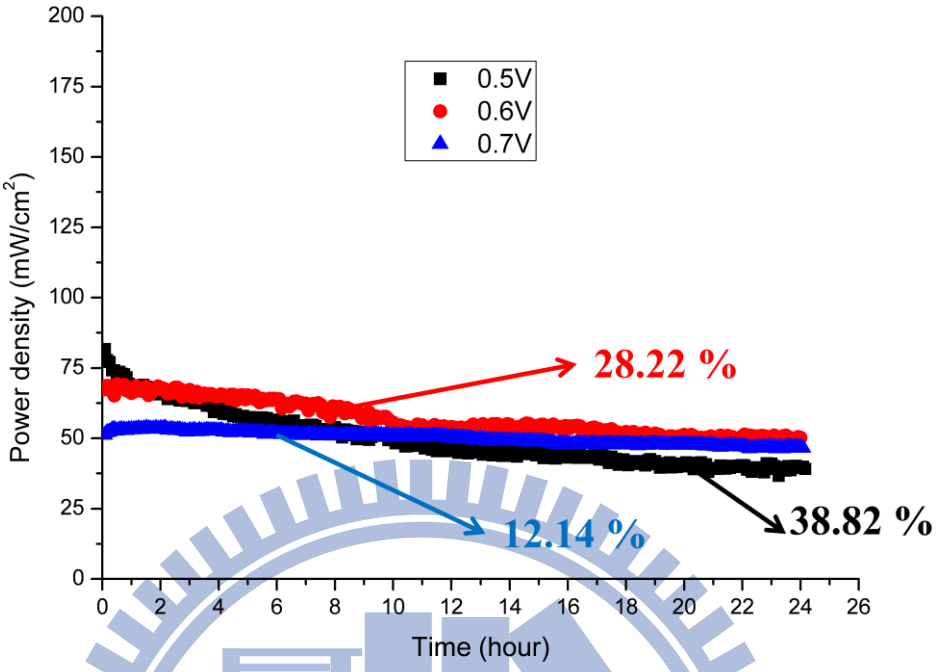

Fig. 4.50 Durability Test for 24 Hours (Graphite PEMFC)

(a) (b)

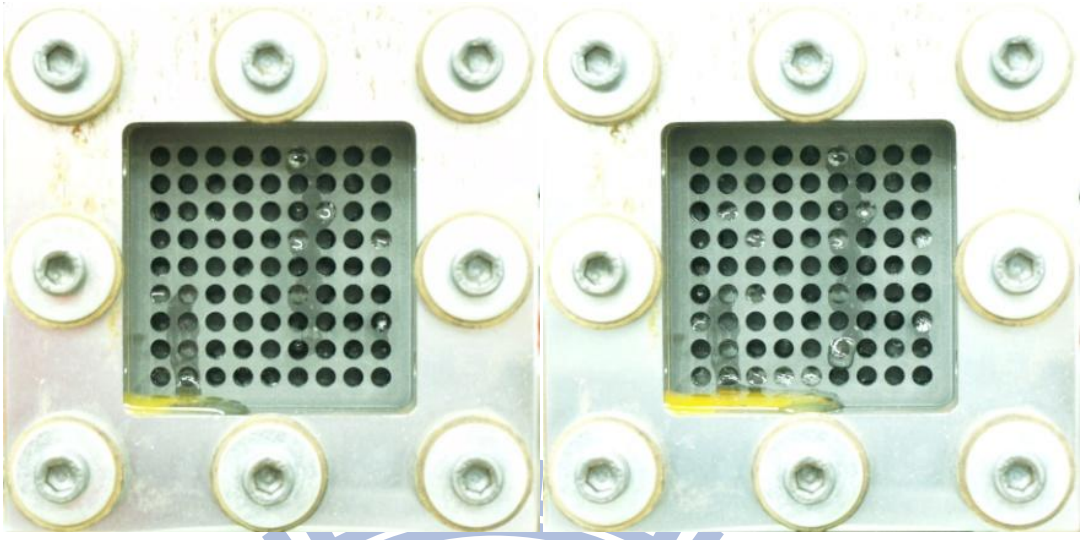

(c) (d)

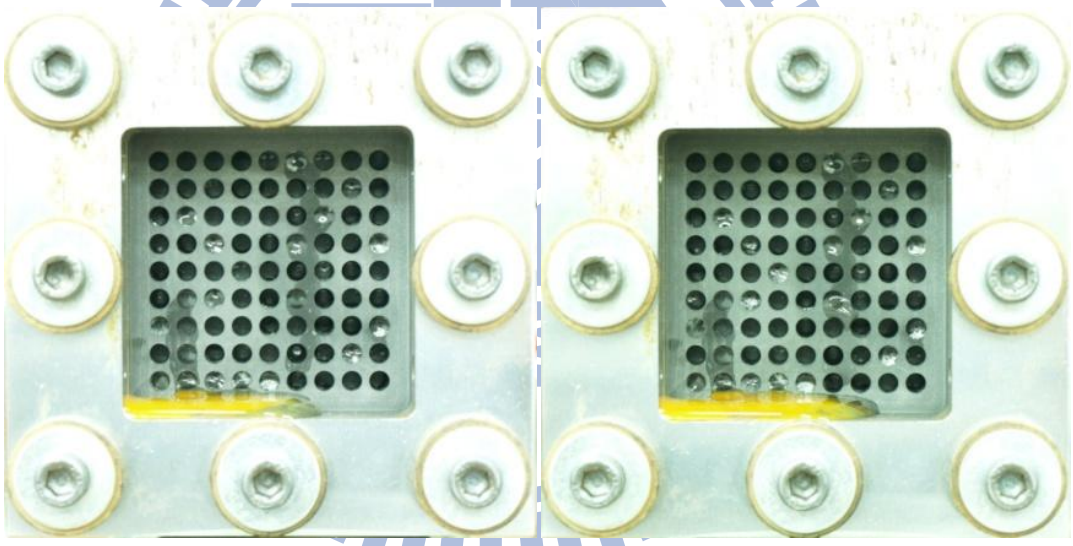

Fig. 4.51 Pictures of Water Accumulation at 0.5V (Graphite PEMFC) (a) 6 hours (b) 12 hours (c) 18 hours (d) 24 hours

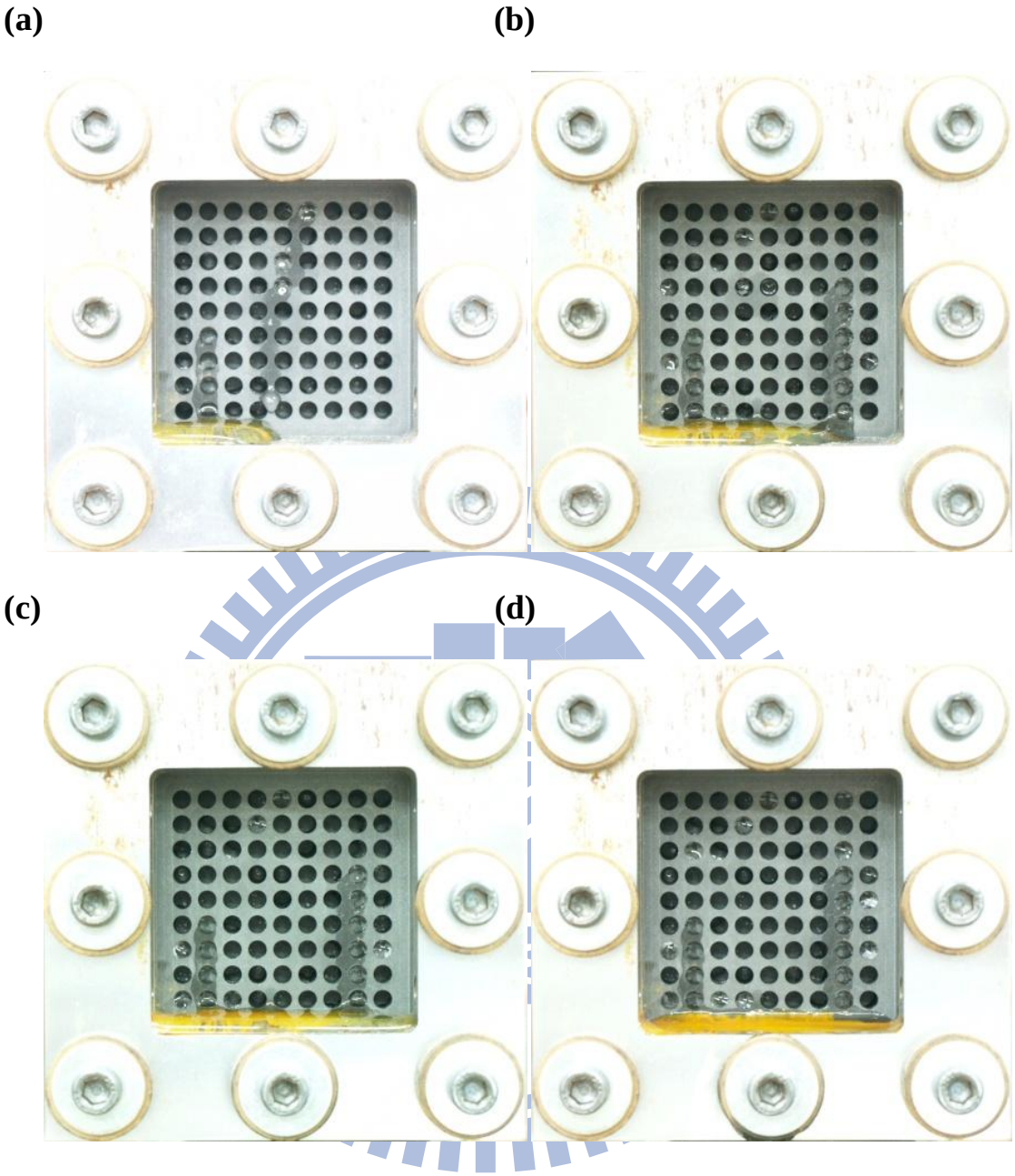

Fig. 4.52 Pictures of Water Accumulation at 0.6V (Graphite PEMFC) (a) 6 hours (b) 12 hours (c) 18 hours (d) 24 hours

(a) (b)

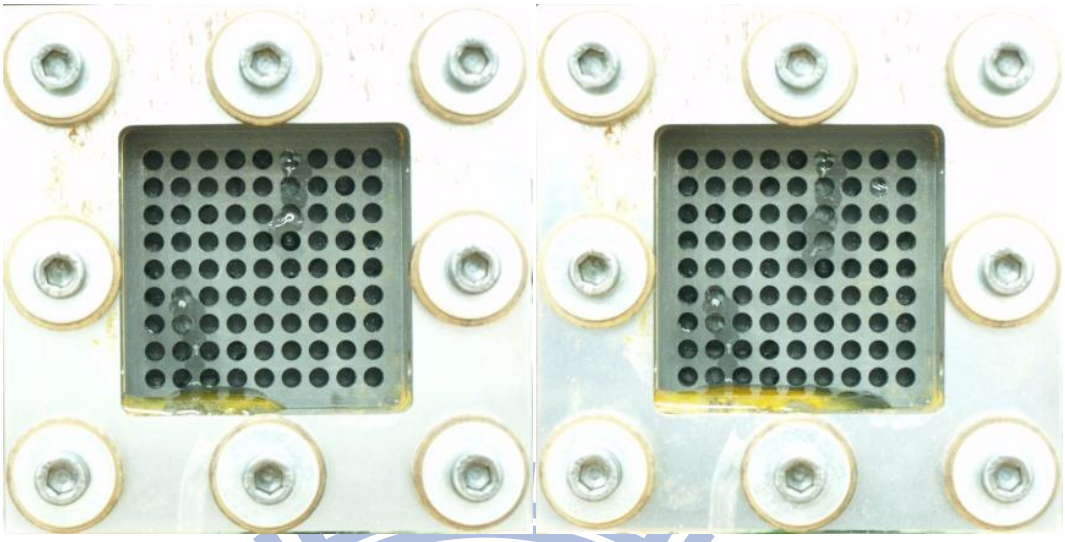

(c) (d)

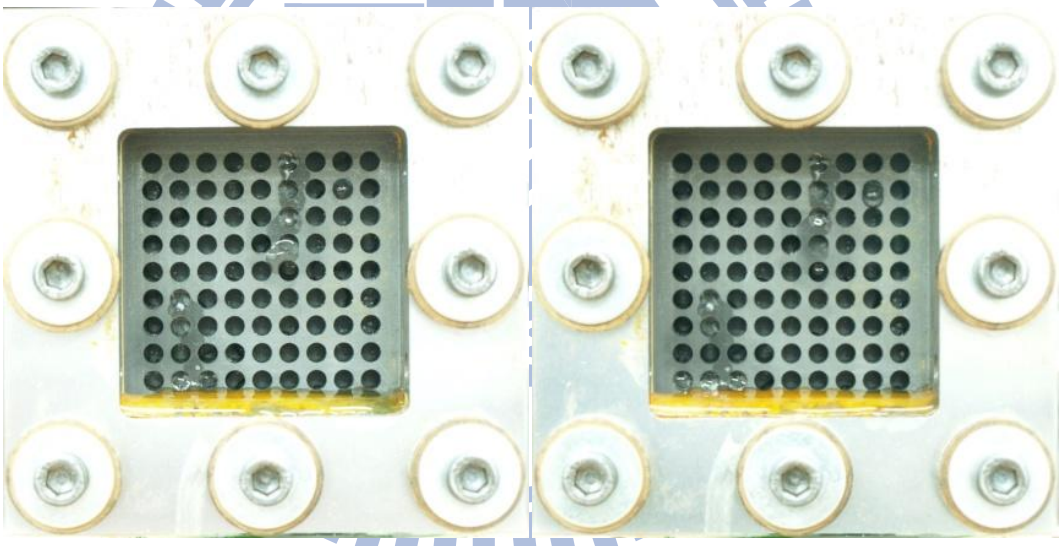

Fig. 4.53 Pictures of Water Accumulation at 0.7V (Graphite PEMFC) (a) 6 hours (b) 12 hours (c) 18 hours (d) 24 hours

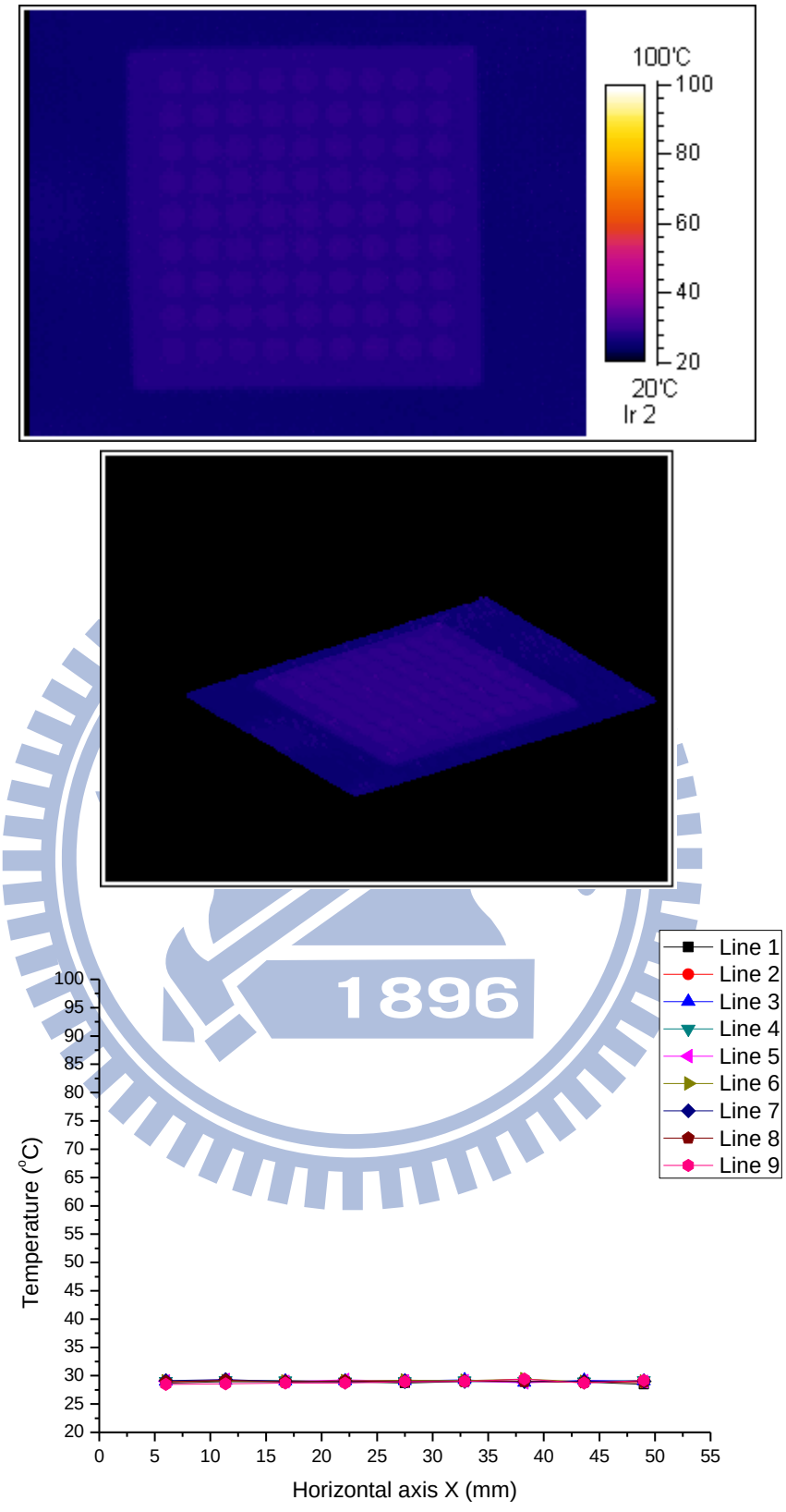

Fig. 4.54 Thermal Images at 0.5V (Graphite PEMFC)

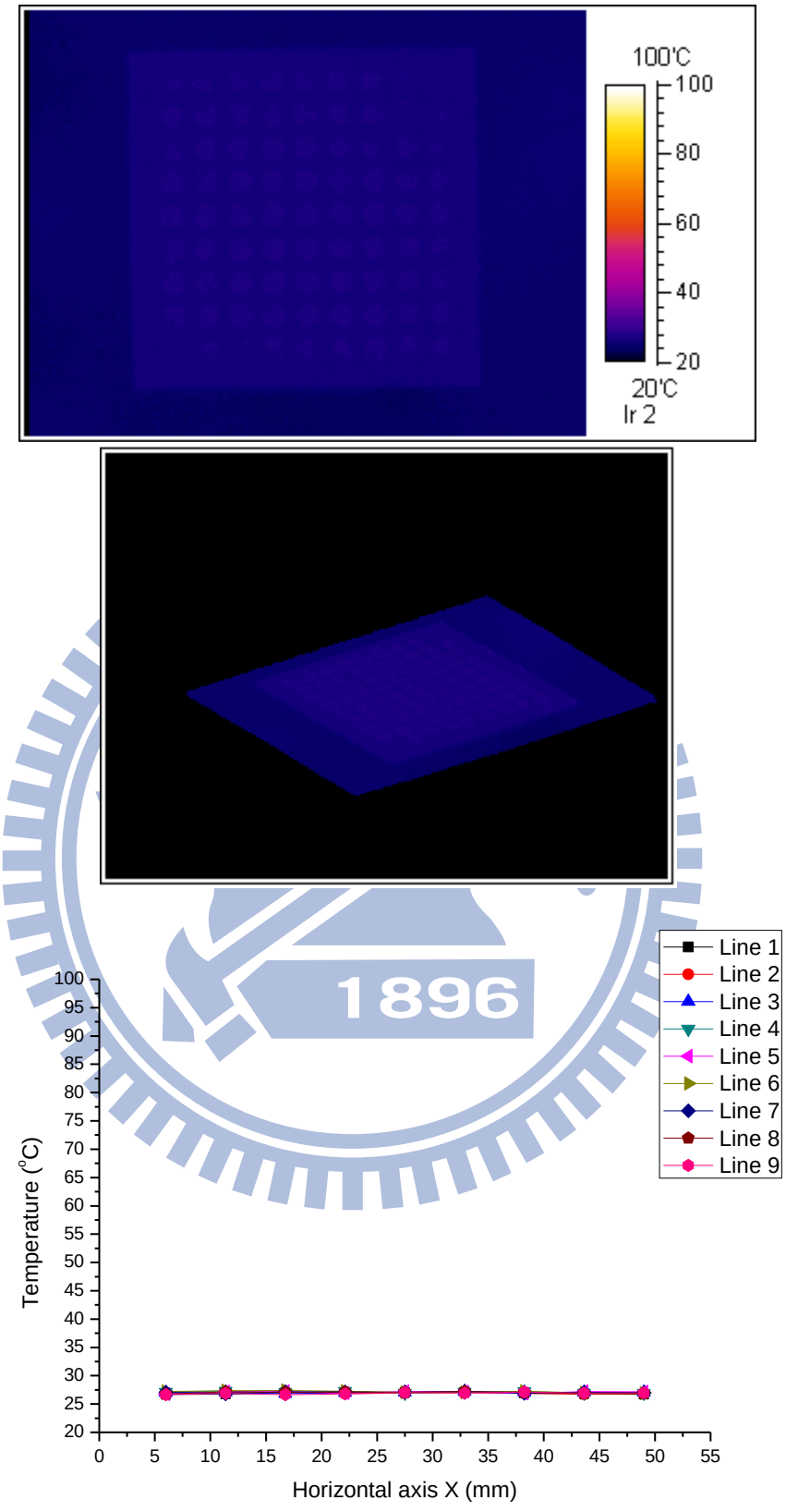

Fig. 4.55 Thermal Images at 0.6V (Graphite PEMFC)

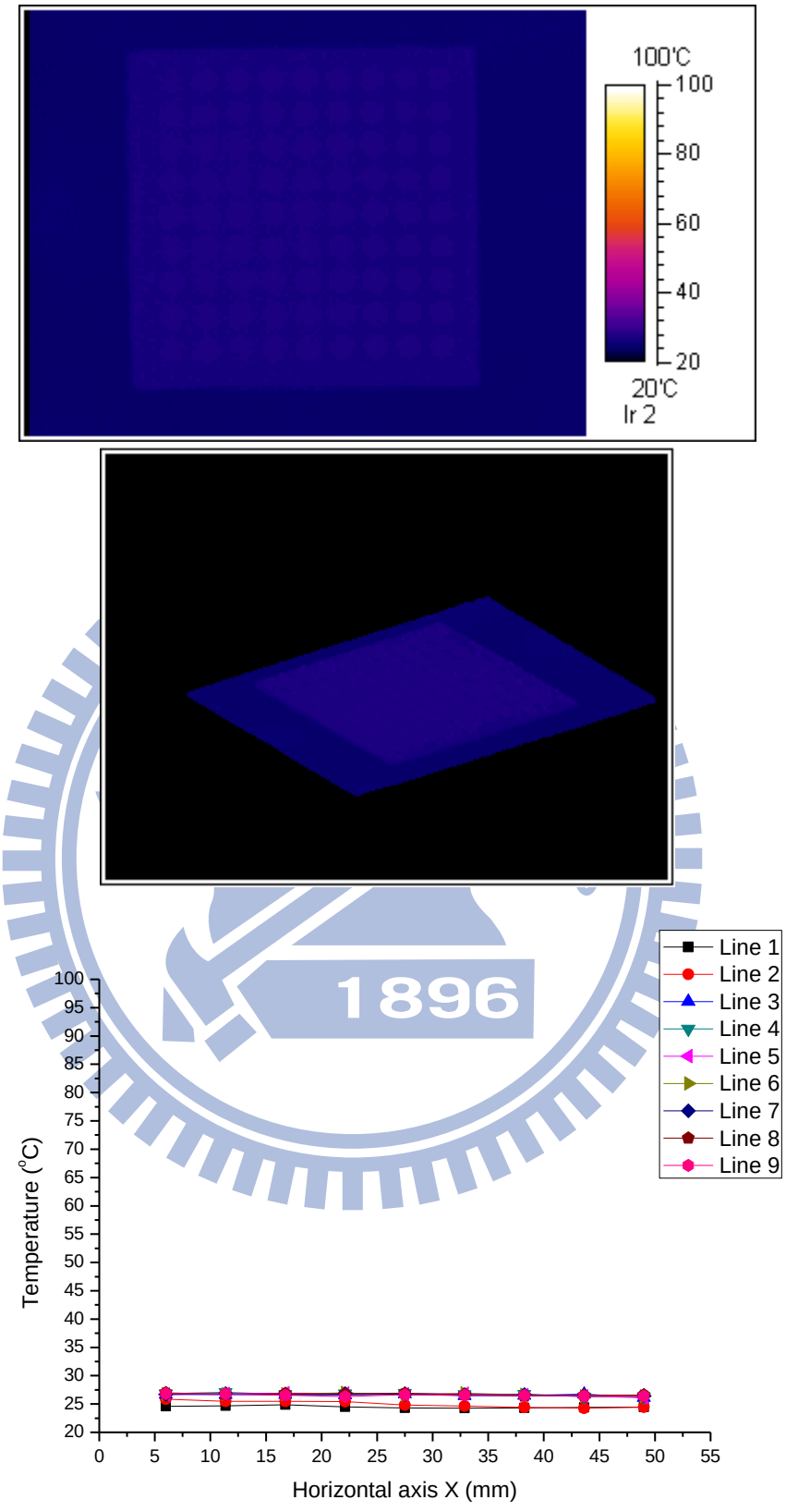

Fig. 4.56 Thermal Images at 0.7V (Graphite PEMFC)

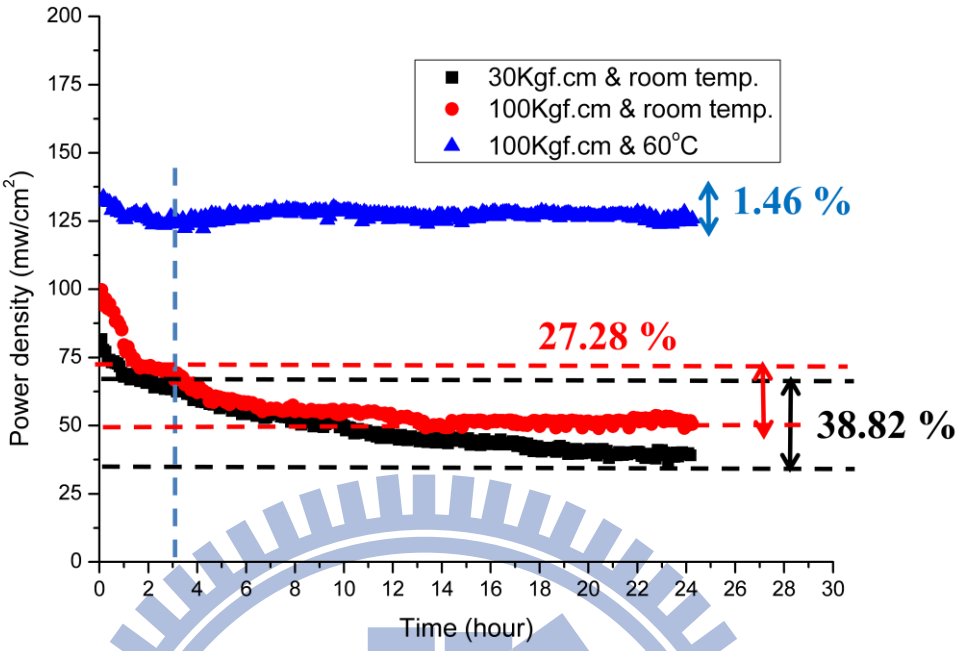

Fig. 4.57 Durability Test for 24 Hours after Improvement (Graphite PEMFC)

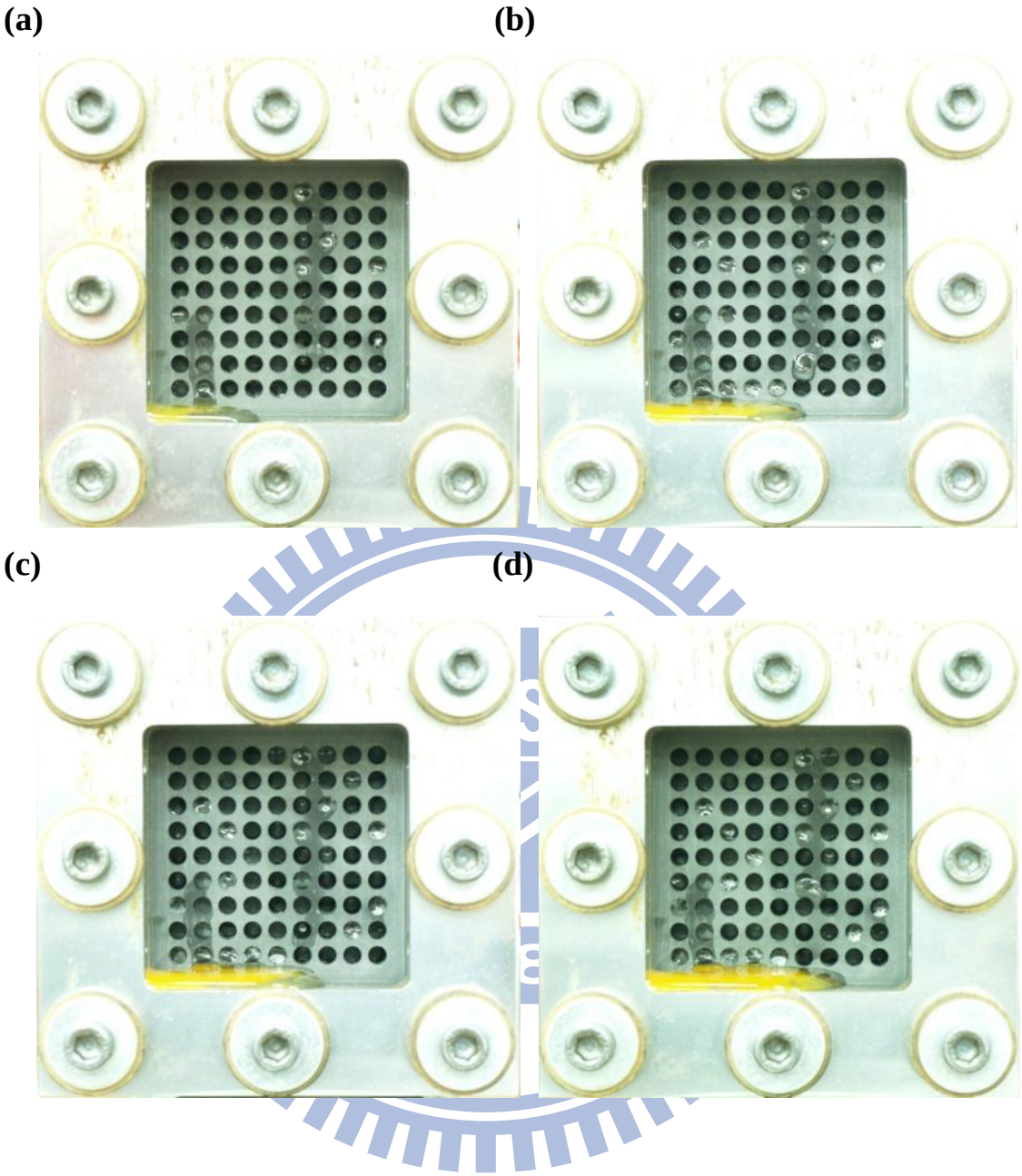

Fig. 4.58 Pictures of Water Accumulation at 30 Kgf·cm and Room Temperature (Graphite PEMFC) (a) 6 hours (b) 12 hours (c) 18 hours (d) 24 hours

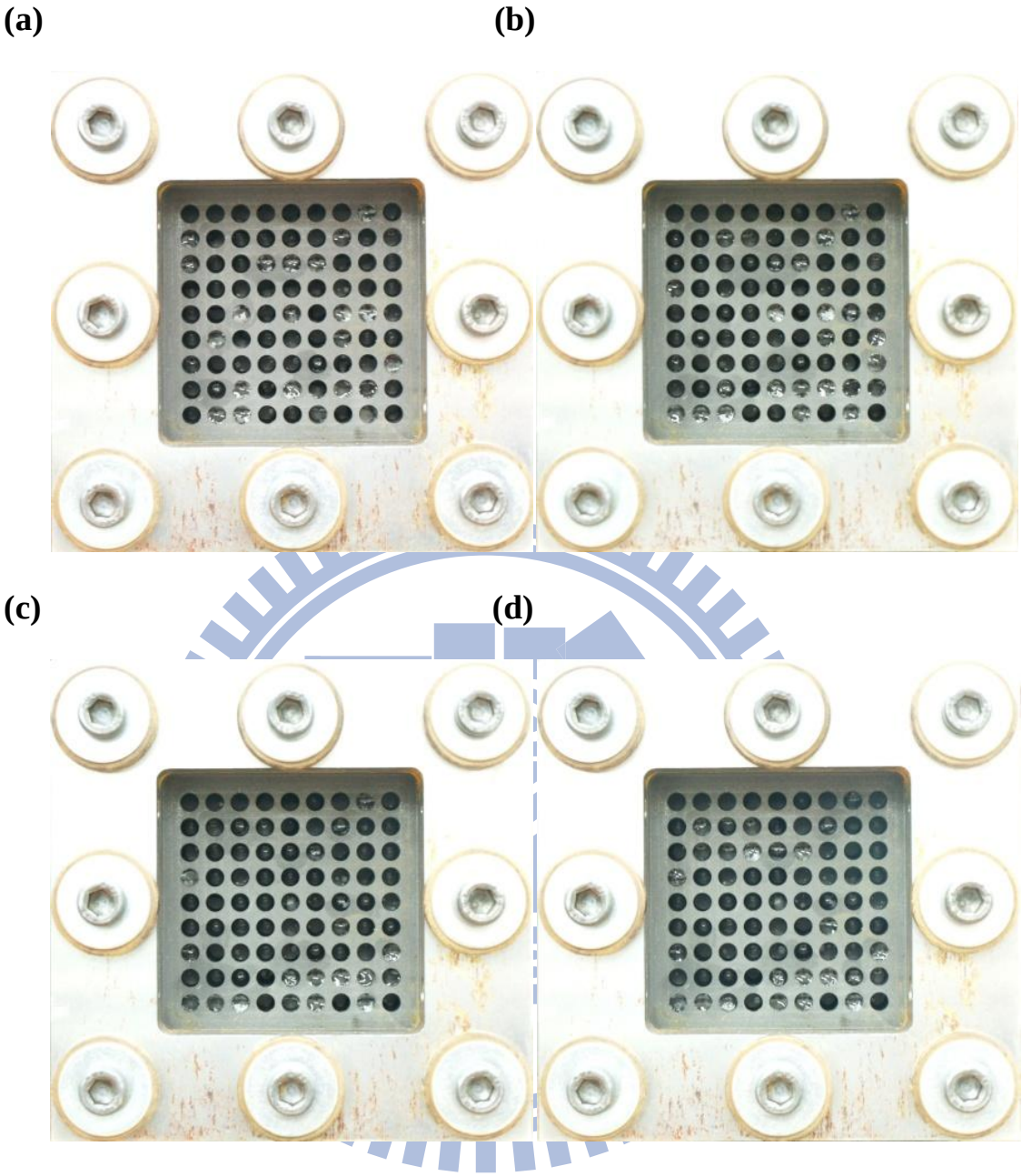

Fig. 4.59 Pictures of Water Accumulation at 100 Kgf·cm and Room Temperature (Graphite PEMFC) (a) 6 hours (b) 12 hours (c) 18 hours (d) 24 hours

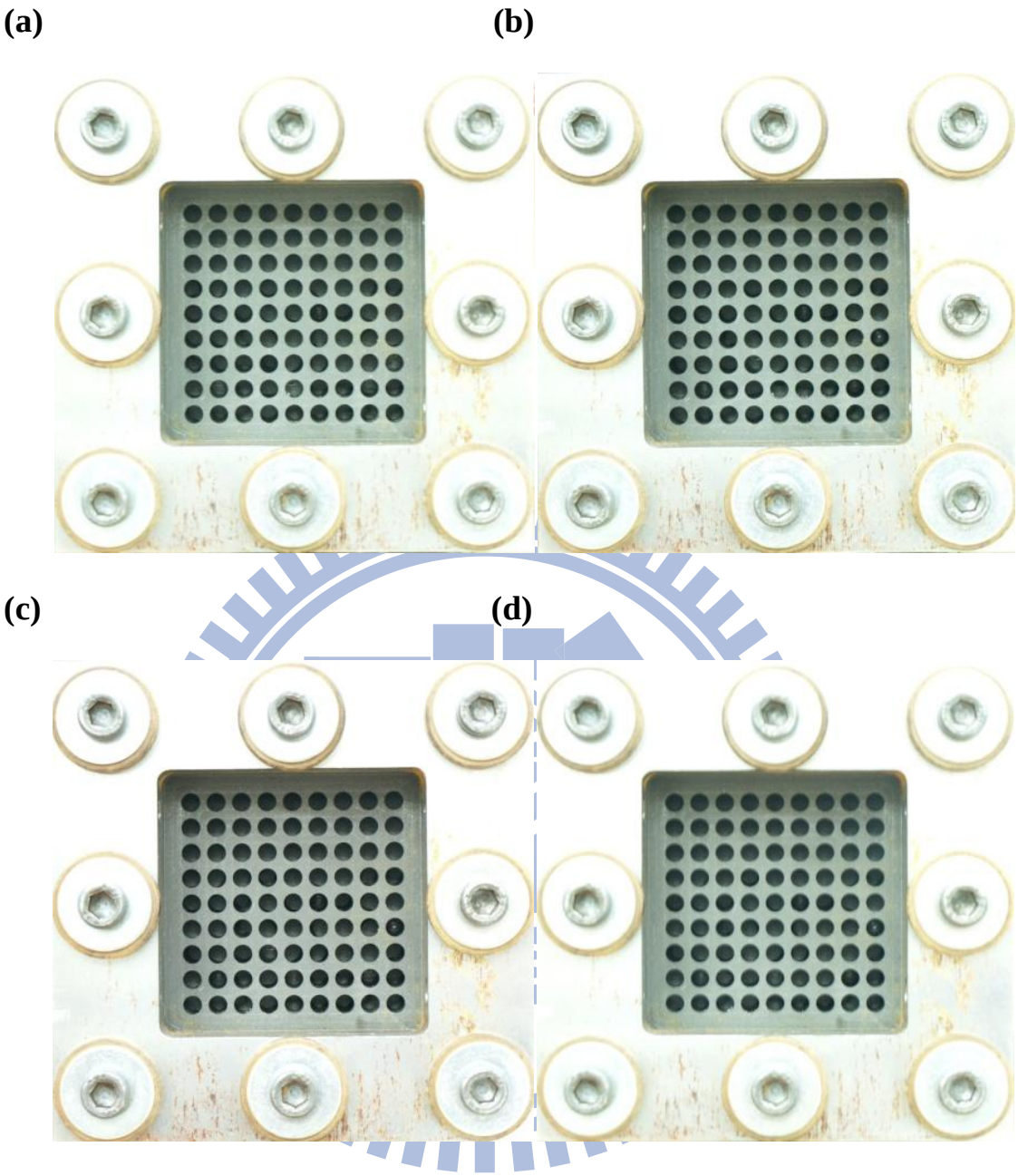

Fig. 4.60 Pictures of Water Accumulation at 100 Kgf·cm and 60℃ (Graphite PEMFC) (a) 6 hours (b) 12 hours (c) 18 hours (d) 24 hours

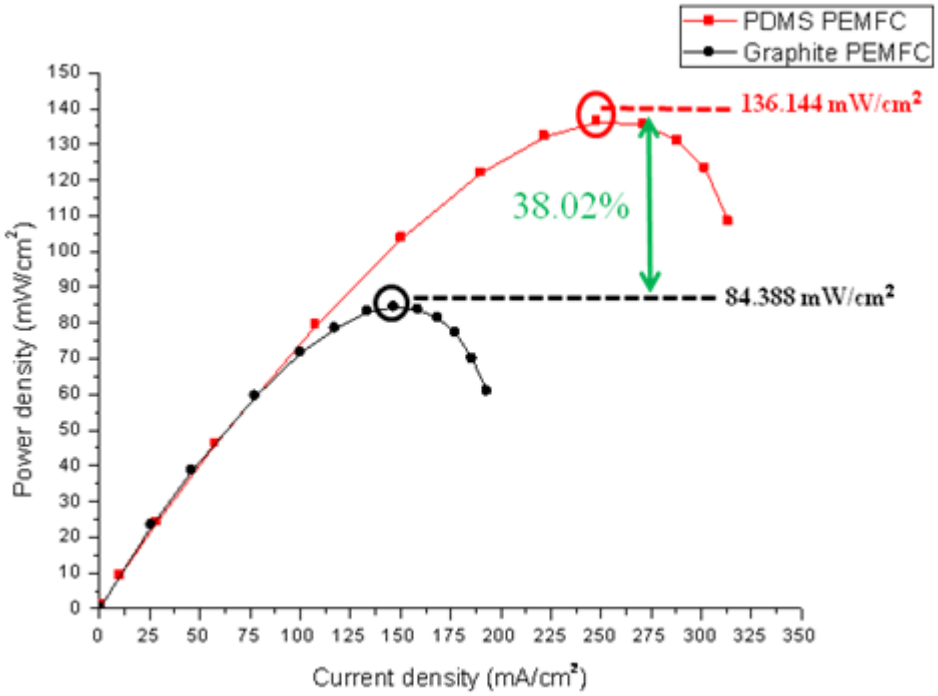

Fig. 4.61 Comparison between PDMS and Graphite PEMFC under the Same Conditions

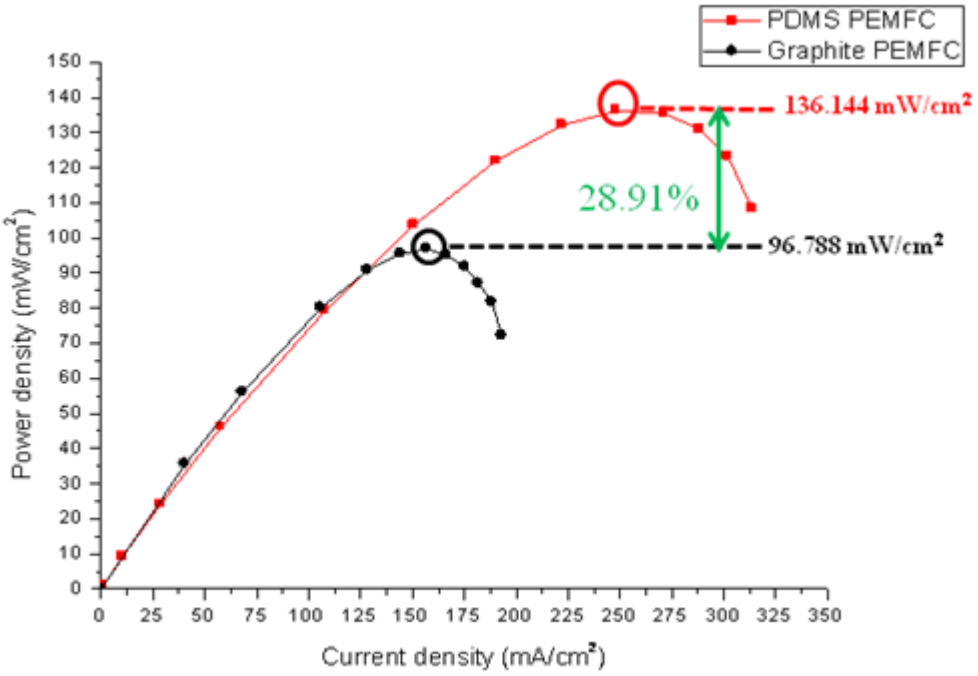

Fig. 4.62 Comparison between PDMS and Graphite PEMFC under the Same Resistance

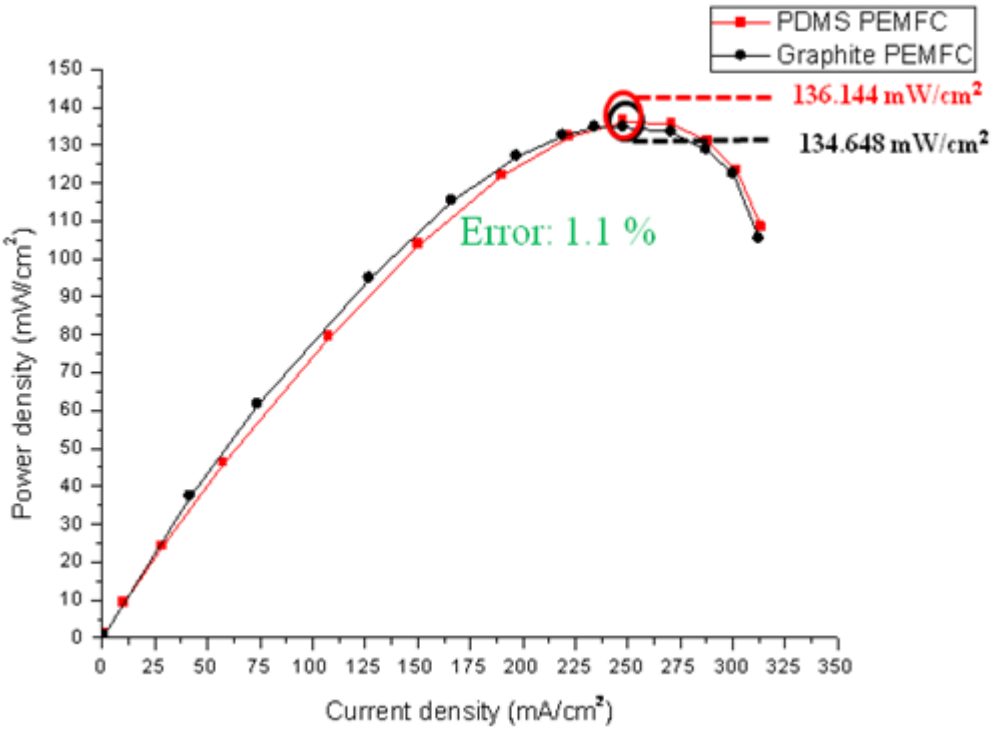

Fig. 4.63 Comparison between PDMS and Graphite PEMFC

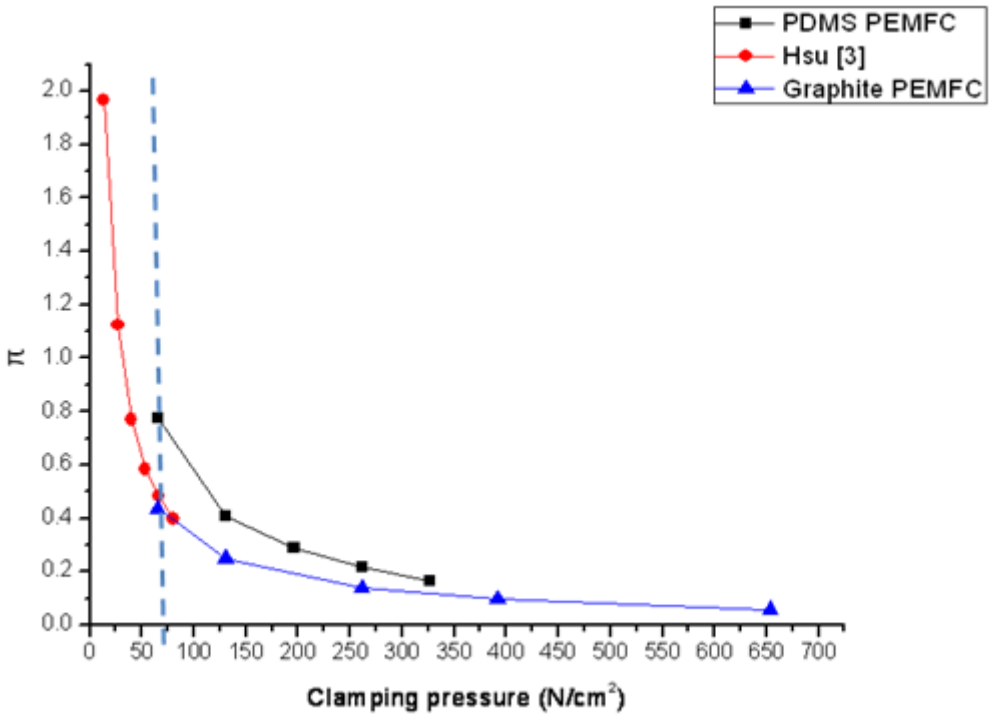

Fig. 4.64 Comparison with Hsu's study [3]

Chapter 5

Conclusions and Recommendations

5.1 Conclusions

This study is divided into three parts. Firstly, a series of performance experiments on a single PDMS air-breathing PEMFC were carried out and demonstrated. The experimental parameters included flow rate with the corresponding hydrogen utilization and clamping force. Secondly, the similar performance experiments on single graphite air-breathing PEMFC were also carried out and illustrated. The experimental parameters consisted of flow rate, clamping force and cell temperature. For both experimental studies, the corresponding thermal imagines of resultant temperature distributions on the cathode surface were given as well. In addition, in order to justify the durability of continuous usage and water produced situation, both fuel cells mentioned above were tested for 24 hours at a fixed operating voltage. Finally, we made a comparison between PDMS and graphite PEMFCs to see the performance difference and the advantage.

According to above experiment results, this study can obtain the following conclusions:

1. The performances of the single PDMS and graphite air-breathing PEMFC increase with an increase of flow rate, but have no further obvious improvements when the flow rates are greater than 60sccm and 40sccm, receptivity.
2. The hydrogen utilization of the single PDMS air-breathing PEMFC is 60sccm, and the corresponding thermal image show its temperature distribution being more uniform.

3. An appropriate clamping force should be considered carefully to enhance the performance without damaging the GDL and narrowing the fuel flow channels. In the present study, a torque of 30.0Kgf·cm is recommended for the single PDMS air-breathing PEMFC. A clamping force of 100.0Kgf·cm applied for the single graphite air-breathing PEMFC has the same resistance as PDMS one with a clamping force of 30.0Kgf·cm.
4. The performance has significantly improved as increasing graphite fuel cell temperature up to 60℃, however, it starts to decrease as the cell temperature above 60℃. There exists a trade-off between water production and evaporation, and the appropriate temperature for graphite fuel cell's performance is 60℃.
5. The single PDMS air-breathing PEMFC can maintain a stable power output for a long time use up to 24 hours. On the contrary, the single graphite air-breathing PEMFC cannot, but it can maintain a stable power output when the clamping force and cell temperature is raised manually to 100 Kgf·cm and 60℃, receptively.
6. The single PDMS air-breathing PEMFC has a better performance with a 38.02% of peak power more than that of the graphite one under the same conditions. The PDMS one has a better performance with a 28.91% of peak power more than that of the graphite one under the same resistance. It is because the PDMS one has higher cell temperature than the one of graphite one that can remove the water effectively to avoid the flooding problem. When both cell temperatures are at 60℃ (controlled manually in graphite one), they have similar performance.

7. PDMS is a better material than graphite for single air-breathing PEMFC because it has less water flooding effects.

5.2 Recommendations

This thesis has some lacks on the experiments. Followings are the recommendations for the near future development of single air-breathing PEMFC:

1. Assemble several cells into a stack to increase power output.
2. Try to use different flow channel designs to improve the performance of the fuel cells.
3. Simulate the temperature distributions of single PDMS air-breathing PEMFC and graphite one by using the computer code.

Reference

[1] R. O'hayre, S.W. Cha, W. Colella, and F.B. Prinz, "Fuel Cell Fundamentals", John Wiley & Sons, New York, 2009.

[2] C.W. Cheng, "The Experimental Study on Micro PEMFC by Using MEMS Technology", June 2009.

[3] Y.J. Hsu, "The Experimental Study on Micro PDMS PEMFC Manufactured by Using MEMS Technology", June 2010.

[4] J.P. Meyers and H.L. Maynard, "Design considerations for miniaturized PEM fuel cells", Journal of Power Sources, 109, pp. 76-88, 2002.

[5] M. Noponen, T. Mennola, M. Mikkola, T. Hottinen, and P. Lund, "Measure of current distribution in a free-breathing PEMFC", Journal of Power Sources, 106, pp. 304-312, 2002.

[6] K. Shah, W.C. Shin, and R.S. Besser, "A PDMS micro proton exchange membrane fuel cell by conventional and non-conventional microfabrication techniques", Sensors and Actuators, B 97, pp. 157-167, 2004.

[7] S. Shimpalee, S. Greenway, and J.W. Van Zee, "The impact of channel path length on PEMFC flow-field design", Journal of Power Sources, 160, pp. 398-406, 2006.

[8] A. Schmitz, M. Tranitz, S. Eccarius, A. Weil, and C. Hebling, "Influence of cathode opening size and wetting properties of diffusion layers on the performance of air-breathing PEMFCs", Journal of Power Sources, 154, pp. 437-447, 2006.

[9] U.H. Jung, S.U. Jeong, K.T. Park, H.M. Lee, K. Chun, D.W. Choi, and S.H. Kim, "Improvement of water management in air-breathing and air-blowing PEMFC at low temperature using hydrophilic silica nano-particles",

International Journal of Hydrogen Energy, 32, pp. 4459-4465, 2007.

[10] C.Y. Chen, W.H. Lai, B.J. Weng, H.J. Chuang, C.Y. Hsieh, and C.C. Kung, “Planar array stack design aided by rapid prototyping in development of air-breathing PEMFC”, Journal of Power Sources, 179, pp. 147-154, 2008.

[11] K. Ito, K. Ashikaga, H. Masuda, T. Oshima, Y. Kakimoto, and K. Sasaki, “Estimation of flooding in PEMFC gas diffusion layer by differential pressure measurement”, Journal of Power Sources, 175, pp. 732-738, 2008.

[12] C.Y. Wen and G.W. Huang, “Application of a thermally conductive pyrolytic graphite sheet to thermal management of a PEM fuel cell”, Journal of Power Sources, 178, pp. 132-140, 2008.

[13] S. Pandiyan, K. Jayakumar, N. Rajalakshmi, and K.S. Dhathathreyan, “Thermal and electrical energy management in a PEMFC stack--- An analytical approach”, International Journal of Heat and Mass Transfer, 51, pp. 469-473, 2008.

[14] C.P.B. Siu and M. Chiao, “A Microfabricated PDMS Microbial Fuel Cell”, Journal of Microelectromechanical System, vol. 17, no. 6, 2008.

[15] Y.A. Song, C. Batista, R. Sarpeshkar, and J. Han, ” Rapid fabrication of microfluidic polymer electrolyte membrane fuel cell in PDMS by surface patterning of perfluorinated ion-exchange resin”, Journal of Power Sources, 183, pp. 674–677, 2008.

[16] C.Y. Wen, Y.S. Lin, and C.H. Lu, “Performance of a proton exchange membrane fuel cell stack with thermally conductive pyrolytic graphite sheets for thermal management”, Journal of Power Sources, 189, pp. 1100-1105, 2009.

[17] N. Bussayajarn, H. Ming, K.K. Hoong, W.Y.M. Stephen, and C.S. Hwa, “Planar air breathing PEMFC with self-humidifying MEA and open cathode

geometry design for portable applications", International Journal of Hydrogen Energy, 34, pp. 7761-7767, 2009.

[18] W. Dai, H. Wang, X.Z. Yuan, J. J. Martin, D. Yang, J. Qiao, and J. Ma, "A review on water balance in the membrane electrode assembly of proton exchange membrane fuel cells", International Journal of Hydrogen Energy, 34, pp. 9461-9478, 2009.

[19] N. Karst, V. Faucheux, A. Martinent, P. Bouillon, J.Y. Laurent, and F. Druart, J.P. Simonato, "Innovative water management in micro air-breathing polymer electrolyte membrane fuel cells", Journal of Power Sources, 195, pp. 1156-1162, 2010.

[20] M.B. Pomfret, D.A. Steinhurst, D.A. Kidwell, and J.C. Owrutsky, "Thermal imaging of solid oxide fuel cell anode processes", Journal of Power Sources, 195, pp. 257-262, 2010.

[21] S.H. Kim, H.Y. Cha, C.M. Miesse, J.H. Jang, Y.S. Oh, and S.W. Cha, "Air-breathing miniature planar stack using the flexible printed circuit board as a current collector", International Journal of Hydrogen Energy, 34, pp. 459-466, 2009.

[22] J. Yu, P. Cheng, Z. Ma, and B. Yi, "Fabrication of miniature silicon wafer fuel cells with improved performance", Journal of Power Sources, 124, pp.40-46, 2003.

[23] L. Zhang, Y. Liu, H. Song, S. Wang, Y. Zhou, and S. J. Hu, "Estimation of contact resistance in proton exchange membrane fuel cells", Journal of Power Sources, 162, pp.1165-1171, 2006.

[24] W.R. Chang, J.J. Hwang, F.B. Weng, and S.H. Chan, "Effect of clamping pressure on the performance of a PEM fuel cell", Journal of Power Sources, 166, pp.149-154, 2007.

[25] P. Zhou, C.W. Wu, and G.J. Ma, “Influence of clamping force on the performance of PEMFCs”, Journal of Power Sources, 163, pp.874-881, 2007.

[26] C.Y. Wen, Y. S. Lin, and C.H. Lu, “Experimental study of clamping effects on the performances of a single proton exchange membrane fuel cell and a 10-cell stack”, Journal of Power Sources, 192, pp.475-485, 2009.

[27] C.I Lee and H.S. Chu, “Effects of temperature on the location of the gas-liquid interface in a PEM fuel cell”, Journal of Power Sources, 171, pp.718-727, 2007.

[28] M. Matian, A.J. Marquis, and N.P. Brandon, “Application of thermal imaging to validate a heat transfer model for polymer electrolyte fuel cells”, International Journal of Hydrogen Energy, 35, pp.12308-12316, 2010.

[29] J.Zhang, Y. Tang, C. Song, X. Cheng, J. Zhang, and H. Wang, “PEM fuel cells operated at 0% relative humidity in the temperature range of 23-120℃”, Electrochimica Acta, 52, pp.5095-5101, 2007.

[30] T. Ous and C. Arcoumanis, “The formation of water droplets in an air-breathing PEMFC”, International Journal of Hydrogen Energy, 34, pp. 3476-3487, 2009